Centre for
Energy Research

Óbuda University

Doctoral School on Materials Sciences and Technologies

Institute of Technical Physics and Materials Science

Centre for Energy Research

Development of Non-Destructive Optical Mapping Tools without Moving Parts for Macro- and Micro-Scale Spectroscopic Ellipsometry

PhD Thesis

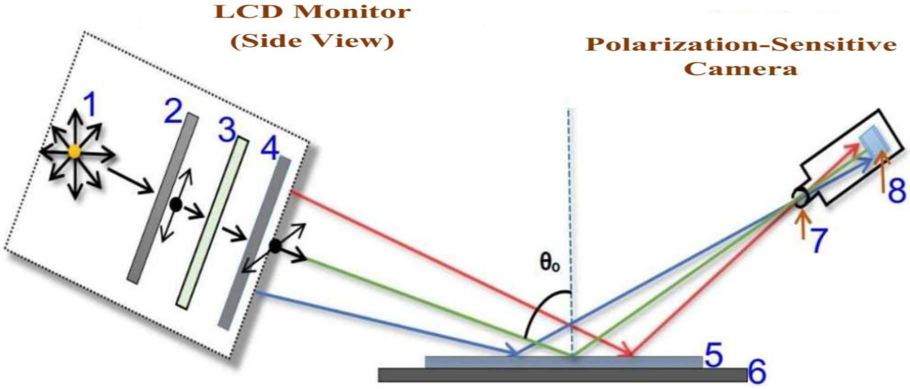

By: **Berhane Nugusse Zereay**

Supervisor: **Miklos Fried, DSc**

Óbuda University, Budapest (Hungary)

2026

Development of Non-Destructive Optical Mapping Tools without Moving Parts for Macro- and Micro-Scale Spectroscopic Ellipsometry

Berhane Nugusse Zereay

Supervisor: **Prof. Miklós Fried (DSc)**

Submitted in partial fulfillment of the requirements for the degree of
Doctor of Philosophy on Materials Sciences and Technologies

Óbuda University, Budapest, Hungary

2026

Table of Contents

List of acronyms

NDT : Non Destructive Testing,

SE : Spectroscopic Ellipsometry

RGB : Red Green Blue
AoI : Angle Of Incidence
Si : Silicon
SiO_2 : Silicon dioxide
a-Si : Amorphous Silicon
c-Si : Single crystal Silicon
tan (ψ) : the amplitude ratio
Δ : (delta) phase difference
ρ : rho
UV : Ultra-Violet
NIR : Near Infra-Red

1. Introduction

1.1. Background information

To start with, a Non Destructive Testing (NDT) is a technique that consists of a variety of non-invasive inspection techniques used to evaluate material properties, components or the entire process units. It can be used during all the stages of the manufacturing processes of the material sample. The main purpose of NDT is to inspect a component in a safe, reliable and cost effective manner without causing any damage to the material [38], as it requires a low power light source.

Generally, NDT is divided into conventional and non-conventional (advanced) methods, where the methods are almost complementary to each other. The key characteristics of the conventional methods include simplicity, accessibility and general standardization .They are the foundation of today`s most advanced NDT methods. In contrast, the non-conventional (advanced) NDT methods are more recent and modern methods integrated with complex sensors, digital imaging, advanced data processing with automation yielding high data quality output.

Optical mapping tools, a type of non-destructive mapping tools, are techniques used to characterize the structural, chemical and physical properties of materials by adopting the interaction of light with the matter. The interaction of light with the matter is a physical process that occurs when an electromagnetic radiation encounters atoms, molecules or materials during light absorption, reflection, transmission or scattering.

Note that non-destructive mapping tools is a broad field mainly containing an optical, X-ray, acoustic (ultrasonic), magnetic or electrical mapping techniques see the flow chart below.

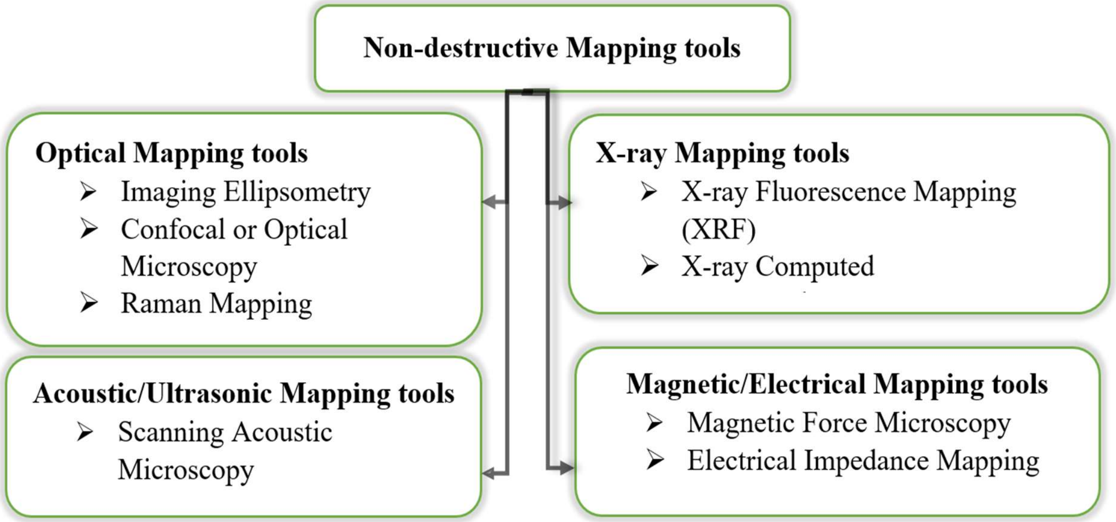

Figure 1.1. Non-destructive mapping tools flow chart

Almost in all disciplines of science, for example in the field of material sciences like thin films characterization in photovoltaics [1], microelectronics, and in biological and medical sciences, non-destructive optical techniques play a great role. One of the most widely used techniques is the spectroscopic ellipsometry (SE) [2]. Spectroscopic ellipsometry primarily measures the relative change in polarization state of the measurement beam induced by reflection from or transmission though a sample. It measures the amplitude ratio, tan (ψ), and the phase difference, Δ(delta), between the p-polarizations (light polarized parallel to the plane incidence) and the s-polarizations (light polarized perpendicular to the plane of incidence) [1]. It is a relatively fast, non-destructive, non-intrusive, noninvasive and contactless optical technique [3]. Upon interaction, the polarized light often becomes elliptical, a reason behind the name's derivation for spectroscopic 'ellipsometry' [2] [47].

During most of the measurements, in laboratory or during fabrication process, spectroscopic ellipsometry is used to analyze multilayered film structures, interfaces, and composites. It is capable for extreme sensitivity to layer thickness changes well below 1Å [4]. At the same time, it has high-speed measurement capability, makes it an efficient optical tool for imaging or mapping. Under appropriate circumstances, SE determines film thicknesses more accurately than any other known technique [3]. Advances in data-acquisition speed have made spectroscopic ellipsometry more relevant for rapid in-line metrology [5]. In addition to optical properties, ellipsometry may also be used to characterize materials' composition, crystallinity, doping, and electrical conductivity with the right modelling and calibration [6].

However, solving an inverse problem is what ellipsometry data analysis entails. As ellipsometry is an indirect measurement method, information about the sample under study is obtained by fitting measured ellipsometry spectra to optical and structural models [7], which usually is a complex data analysis and fitting process [44]. During data analysis, the measured values cannot be converted directly into physical parameters. Usually, a good optical model should be created and a fitting procedure is used to evaluate the variable parameters. Finding the best match between the model and the experiment is typically achieved through regression, where the computer program calculates the ellipsometric angles (based on the optical model) and compares them with the measured ones. An estimator, such as the mean square error (MSE), is used to quantify the difference between the calculated and measured ellipsometric angles. A lower MSE indicates a better-fit and better optical model [2].

There is an analytic forward function that relates material properties to experimental data for a certain optical model that includes sample geometry and incidence plane, ellipsometric angles (Ψ and Δ) as a function of wavelength (λ) and incidence angle.

In order to understand material properties from experimental data, the inverse function should be computed, either explicitly or implicitly.

However, inversion is challenging due to the forward function's complexity and nonlinearity. Ellipsometry data is easy to interpret when the materials are well understood and there are few unknowns. However, the analysis becomes rigorous with complexity of situations in increasingly complicated situations and the analysis is frequently extremely time-consuming [6].

Basically, there are well-established analysis methods in which one can extract the optical properties and material thicknesses from the experimental spectroscopic ellipsometry data by reversing the forward function.

The most popular method combines nonlinear regression with models, including the Drude and Tauc-Lorentz models, which use a limited number of parameters to characterize the properties of optical materials. Another approach, spline analysis, uses a piecewise polynomial to parametrize the imaginary component of the dielectric function and the Kramers-Kronig (KK) connection to calculate the real part [8]. In this case, the spline parameterization is affected by the nonlinear regression instead of the underlying spectral model.

A wavelength-by-wavelength method is another option [9]. The forward function at a particular wavelength is independent of evaluation at other wavelengths and only depends on sample characteristics. Because of this, the forward function is input and output tensors at a particular wavelength have comparatively low dimensionality (usually, less than 10), allowing for an analytical approximation of the inverse function. Nevertheless, this method only works if the forward function is one-to-one, and there is not a straightforward way to tell if that is the case. Furthermore, this method does not ensure the continuity, smoothness, and KK-consistency of the inferred spectrum because the function is evaluated wavelength-by-wavelength.

Recently, with the advancement of artificial intelligence (AI), a deep learning approach is under intensive investigation, which tries to tackle the time consuming ellipsometric data analysis and poor precision, especially with increasing number of parameters. A deep learning, fundamentally based on artificial neural networks, is specialized subset of machine learning [6].

Note that AI is a branch of research that focusses on creating machines and computers that are capable of reasoning, learning, and acting in ways that would typically need human intelligence or that include data that is too large for people to analyze, where as

Machine Learning (ML) is a broad field of Artificial Intelligence (AI) where systems are designed to train and then learn autonomously from a huge data and make decisions or predictions without being explicitly programmed.

Generally, ellipsometry technique uses collimated light beams with a well-defined angle of incidence to illuminate the sample. Fried et al. showed a non-parallel expanded beam could also be used [10] [11].

During in situ real-time measurement, fabrication and processing, ellipsometry is used to analyze the multilayered film structures, interfaces, and composites, being famous for its extreme sensitivity to very thin over layers well below 1Å thickness [4], which makes it an efficient optical mapping tool for thin film solar cells added with its high-speed measurement capability. Under appropriate circumstances, SE determines film thicknesses more accurately than any other known technique [12] and a thorough and in-depth data analysis can yield a very rich information regarding the material's optical properties, layer thicknesses, and other relevant parameters [13]. The optical properties of a material may include the refractive index (n), the extinction coefficient (k), dielectric function and absorption coefficient (α) [1]. These parameters can entirely explain the propagation of the electromagnetic waves in the media.

However, several critical considerations must be addressed when conducting spectroscopic ellipsometry measurements.

First, the size of the surface roughness of samples has to be rather smaller than the wavelength of the measurement beam, generally below 30%, otherwise the scattered light depolarizes the measurement beam and deviates the reflected beam away from the detector, in addition to the reduction the light intensity.

Surface roughness is a common characteristic of real-world films that needs to be considered in any precise optical model. The Effective Medium Approximation (EMA), which is the most widely used method, treats the roughness of inhomogeneous materials (like porous thin films, rough interfaces or mixed phases) as a separate layer with an effective dielectric function, usually a 50/50 blend of void and underlying material. EMA treats these materials as if they were homogeneous media with some "effective" optical properties (e.g., refractive index or dielectric constant).Nonetheless; a great deal of research has been done in relation between the thickness of the EMA layer and the morphological features of the roughness.

Some popular specific models that fall within the broader framework of the EMA are Maxwell Garnett Approximation (MG) and the Bruggeman Approximation methods.

- Maxwell Garnett Approximation (MG): Asymmetrical EMA model that assumes a host medium with embedded inclusions most suitably used during small inclusions (e.g., nanoparticles, pores, voids) are dispersed in a continuous host matrix.
- Bruggeman Approximation: Symmetrical EMA model that treats all components equally; no distinct host or inclusion, most appropriately used when phases are intermixed, or the volume fractions are comparable.

The work of Fodor et. al. (2016) [50] provides critical insight into this relationship through rigorous finite-element method (FEM) simulations. They demonstrated that for random rough surfaces, the ellipsometric response calculated via FEM matches that of an EMA model only when the illumination wavelength is much larger than the surface feature size. Furthermore, they established that, the correlation between d_EMA and the root-mean-square roughness (R_RMS) is not linear, as often assumed, but quadratic, and is also dependent on the lateral correlation length (ξ). This work bridges the gap between purely morphological measurements (like AFM) and optical characterization, confirming that ellipsometry is more sensitive to sharper surface features with high local slopes.

Second, to maximize the sensitivity and reaction of the photo detectors, measurements must be carried out at an oblique angle of incidence. Normal and parallel incidences of light beam on a sample are not productive [2]. At a normal angle of incidence, for example, as the s-polarizations (perpendicular to the plane of incidence) and the p-polarizations (parallel to the plane incidence) cannot be distinguished one from the other. This makes the choice of the incidence angle more vital. For semi-conductors, the angle of incidence is typically from 70° -80° [2].

Other common restrictions include, thin film quality (like thickness limitation, transparency, absorption, homogeneity and isotropy), and modelling accuracy.

Note that,

As a rule of thumb, reliable measurements are typically limited to an RMS (root mean square) roughness σ that is less than λ/10, where λ is the measurement wavelength [14].

Film thickness limitation

Upper Thickness Limit: For a standard setup using visible light (Spectroscopic Ellipsometry), films generally need to be under approx. 5μ (micrometers).

Very thick films cause too many interference oscillations in the data disturbing the thickness determination uniqueness. Thin films up to approx. 50μm require IR ellipsometry, longer wavelengths measurement beam [39].

Lower Thickness Limit (Ultra-Thin Layers): While highly sensitive to even sub-nanometer layers, ellipsometry may not be able to uniquely determine both the thickness and the refractive index (n, k) of a layer that is too thin (e.g., a few Angstroms).Often, a known refractive index must be assumed to get an accurate thickness [39].

The flow chart of the Spectroscopic ellipsometry data analysis is shown in figure 1.2.

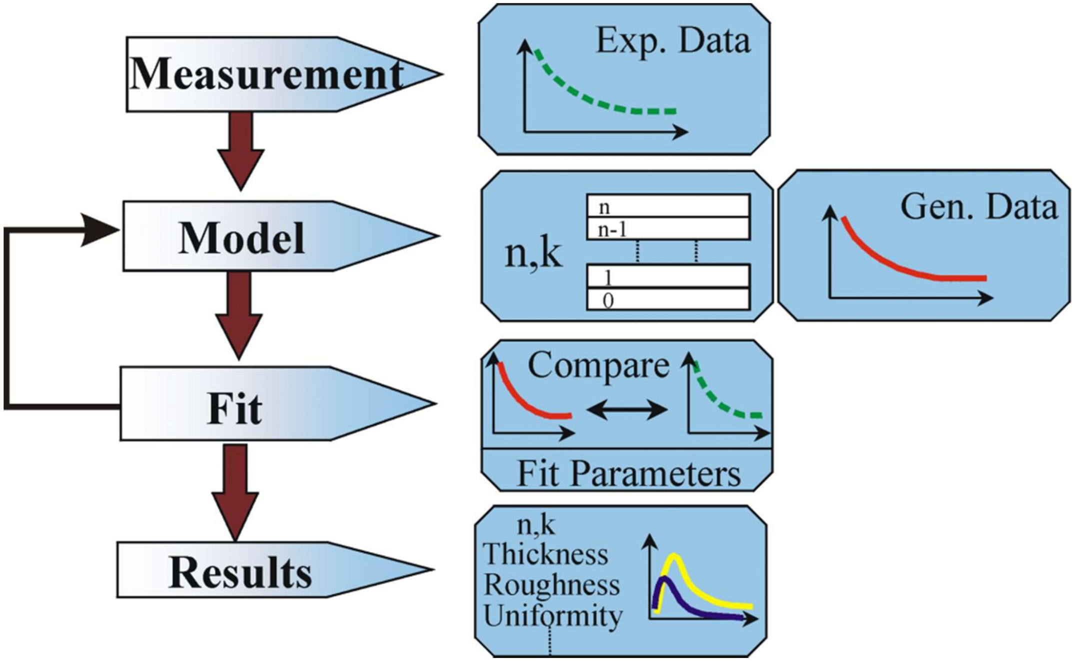

Figure 1.2. Spectroscopic Ellipsometry procedures flow chart

(https://www.jawoollam.com/resources/ellipsometry-tutorial/ellipsometry-data-analysis)

As ellipsometry is an indirect measuring technique, a multi-stage process is required that involves the ellipsometric parameters (Ψ and Δ) measurement, careful optical modelling and iterative fitting to reach to the results, the physical and optical parameters which characterize the material, as shown in Fig. 1.2 flow chart.

The initial stage involves the polarimetric measurements of the sample across a range of wavelengths, RGB range in our cases. After a linearly polarized light incidents at an oblique angle of incidence and gets elliptically polarized upon reflection, the change in polarization state ,defined by Ψ and Δ , is recorded by the polarization sensitive detector.

The measurement process can be classified in five steps [1],

i) Polarized beam generation: this involves generating measurement light beam in a known state of polarization utilizing optical sources like, monochromator, polarizer, compensator. In our case, the light sources used are an LCD-LED monitor and RGB laser module.

ii) Polarized beam-sample interaction: an interaction of the polarized beam of light with a sample, resulting in an emergent beam in a second polarization state, elliptically polarized beam in our case.

iii) Emergent polarized beam detection: the measurement of the emerging polarization state using optical elements such as a compensator, polarizer, spectrometer, and solid-state detector. In our experimental setup assembly, the polarization sensitive camera is used, which uses a solid-state CMOS sensor with specialized polarization filters integrated on chip for advanced polarization imaging.

iv) Determination of ellipsometry data: which involves measuring the change in the polarization state of light upon reflection from a sample, expressed as a complex reflectance ratio, which is the ratio of the reflected p- and s-polarized light components, represented by the amplitude ratio, tan (Ψ), and phase difference, Δ.

v) Data analysis: extraction of the optical and physical material parameters by modeling the sample structure and fitting the calculated reflectance ratios to the experimental data, through robust, model-based regression analysis [1].

The next step is the construction of an optical model that best represents the sample structure, as the measured ellipsometric parameters do not directly give the required properties of the sample. The optical modelling passes through two main considerations, the structural modelling and the dispersion modelling. The structural modelling involves the physical structure (monolayer, multi-layer stuck etc.) with their corresponding approximate thickness estimations to narrowly guide the iteration process. The dispersion modelling is a mathematical description of the complex dielectric functions with respect to the measurement beam spectral range. Some commonly used dispersion models include Cauchy, Sellmier, Tauc-Lorentz and Lorents oscillations, that ensure the dispersion optical constants are physically realistic and satisfy the Kramers-Kronig relations [12]. Note that, the fundamental Kramers-Kronig (KK) equations govern the relationship between the complex dielectric functions, ε_1 and ε_2**.**

The basic relation between these complex dielectric constants and the complex refractive indices of a material is discussed in chapter 2, theoretical background.

A physically well-constrained optical model is required to yield both a statistically good fitting result (low MSE) and physically relevant final parameters. Nevertheless, a good fitting result does not necessarily guarantee a good model, due to the problem of the non-uniqueness or correlation of parameters behavior of, which is a key challenge of the spectroscopic ellipsometric data analysis.

The fitting process, where a complex numerical analysis is carried out, is a crucial part of the SE data analysis process. The fitting process attempts to reduce the discrepancy between the experimentally measured Ψ and Δ ellipsometric spectra and the Ψ and Δ curves theoretically generated by the optical model. An iterative non-linear least-squares algorithm is employed to systematically adjust the unknown parameters within the model (e.g., film thicknesses, critical point energies in the dispersion models, and surface roughness) until the best possible congruence is achieved. The quality of the fit is quantitatively assessed using a metric such as the Mean Squared Error (MSE).

The final step to physically interpret and validate the previous processes and physically define and characterize the sample (physical and optical parameters), resulting from the successful minimization of the MSE.

The integrity of the results is contingent upon the uniqueness and physical viability of the chosen model. Over-parameterization must be avoided, as it can lead to non-unique solutions with low MSE but no physical meaning. Validation often involves comparing the extracted optical constants to established literature or cross-referencing thickness values with complementary techniques, like Transmission Electron Microscopy (TEM) or X-ray Reflectometry (XRR) (the J.A. Woollam M2000DI elllipsometer, in our case.)

A good optical model is necessary to achieve good fitting results (a low Mean Squared Error or MSE) and, more importantly, physically meaningful results [53], as a low MSE indicates a high degree of correlation between the model and the experiment.

Driven by the nanotechnology, ellipsometry is now being further investigated and utilized for the non-destructive and contactless characterization of nanomaterials and nanostructures.

1.2. Outline of the Problem

During conventional ellipsometric mapping, data collection is relatively slow and uses a small scanned spot. We know two industrial systems which are capable of measuring big (square-meter size) samples: the Semilab FPT system [40] and the Woollam AccuMap [41] system. Both systems use a “traditional” SE device (priced approx. 100k USD) in special big moving/scanning systems, measuring the big samples point by point.

The Woollam brochure states that “Data Acquisition Rate: <6 s per point (includes time for movement to new point, automated alignment, and data collection)” so it can measure one big area in several minutes.

Besides, the mechanical part nature of these ellipsometers contributes minor errors, instability and precision of the measurement and their evaluations.

These gaps hinder the measurement speed, difficulty in large area samples analysis, and efficiency of the experimental process as a whole.

Therefore, our laboratory developed optical mapping prototype ellipsometers, large area and small area mapping devices, that addresses these issues and endeavors to cover these gaps.

The newly developed prototype devices, assembled from cost-effective components, provide fast imaging capability-reducing data acquisition time, where large ellipsometric data can be collected in just couple of seconds compared to the several minutes of the conventional scanning ellipsometers. Besides, in comparison to the conventional ellipsometer typical current 15cm diameter sized samples capability, larger area size samples can be analyzed in our new assembly, without incorporating any moving mechanical parts in the setup.

Note that, if the current LCD-LED monitor used in our large area mapping tool assembly is replaced by a larger display panel, LCD TV, mapping area range can extend up to 150 cm.

The newly developed prototype devices are assessed through experimental laboratory works by measuring different types of samples after a proper calibration, validation and comparison of the results with a standard conventional spectroscopic ellipsometer (M2000 DI by J.A. Woollam Co).

1.3. Research objectives and their relevance

The main aim of this work is to assess prototypes for the optical imaging using only non-expensive parts: LCD-LED monitors, TVs or laser diodes for light source and polarization sensitive camera as detector.

This research project is very relevant with the current and future targets of the materials science and technology research areas. The research concentrates on the properties of thin films in the range of 10-100 nm.

Since it is a fast and exponentially growing field of interest nowadays, the research work explores a new way of dealing with our resources and tries to contribute to the long-term aim towards Green energy Vision of our planet, Earth.

The main sub-tasks of the research are:

- Assess prototypes of non-destructive optical imaging devices from inexpensive parts.
- Programming the data collection and data processing software and
- Making measurements on selected samples and determining the precision of the newly developed prototype devices.

1.4. General thesis Outline

The thesis deals with non-destructive optical mapping tools without moving parts from inexpensive parts, unlike the standard conventional spectroscopic ellipsometers with mechanical hardware, on spectroscopic ellipsometry, on two newly developed levels:

i). Macro area level, which considers thin film, samples of macro area level, usually few centimeters, about 30cm diameter thin film samples. Note that the conventional ellipsometers analyze samples of smaller size. The main light source in this case is LCD/LED monitors, emitting with polarized light. The monitor calibration is highly recommended in this case, after some basic calibration of the angle of incidence of the specific experiment, usually using the famous sample SiO_2 on Silicon substrate, before dealing with the monitor correction. It is worth noting that measuring a thin film sample of around 150cm is also possible in this newly developed mapping tool.

ii). Micro area level, which considers thin film samples of micro area level, an imaging microscopic ellipsometer utilizing a point-light source, RGB Laser module. In this setup, only angle of incidence calibration is required.

Many different thin film samples of different area sizes, nature and thicknesses are accomplished. After many experiments, the result is mainly compared with the corresponding results of the Woollam J.A. M2000 DI ellipsometer, our standard reference tool in our case, and with previous scholarly experimental results of other authors.

Each part is supported by careful and detailed independent laboratory experiments through calibrations and comparison and validations.

Compared to the current standard conventional ellipsometers, a faster optical mapping tool, larger or smaller surface area sample analysis, with non-moving inexpensive hardware parts, is achieved which was the main objective of the thesis work.

1.5. Thesis Statements

1. I have shown that it is possible to make a non-destructive optical imaging device from inexpensive parts (LCD-LED monitors, TVs for light source and polarization sensitive camera as a light detector) to measure in one shot on large, macro area, sample sizes. [1, 2]
2. I have shown that it is possible to make a non-destructive optical imaging devices from inexpensive parts (RGB laser diodes for light source and polarization sensitive camera as a light detector) to measure in one shot on small (mm size), micro area, sample sizes. [3]

3. After an appropriate subsequent calibration processes, I have shown that the devices (in points 1 and 2) can image a sample surface with a 1 nm thickness resolution on several 10 thousand pixels. [1-3]

Related Publications

[1] Zereay, Berhane N.; Kálvin, Sándor; Juhász, György; Major, Csaba; Petrik, Péter; Horváth, Zoltán G.; Fried, Miklós, "Optical Calibration of a Multi-Color Ellipsometric Mapping Tool Fabricated Using Cheap Parts" PHOTONICS 11 : 11 Paper: 1036 , 11 p. (2024) IF: 2.1

[2] Sándor Kálvin, Berhane Nugusse Zereay, György Juhász, Csaba Major, Péter Petrik, Zoltán György Horváth, Miklos Fried, "A new method to evaluate multi-color ellipsometric mapping on big area samples", Sci 2026, 8, 17. https://doi.org/10.3390/sci8010017 IF: 3.28 Q1 (Multidisciplinary)

[3] Csaba Major, Berhane Nugusse Zereay, György Juhász, Péter Petrik, Zoltán György Horváth, Péter Fürjes, Boglárka Kovács, György Zoltán Radnóczi, Sandor Kurunczi, Róbert Horváth, Levente Illes, Tamás Kolonits, Csaba Dücső and Miklós Fried, "A new type of microscopic ellipsometer utilizing point-like light source" submitted in Sci IF: 3.28 Q1 (Multidisciplinary).

In Proceedings

Nugusse, Berhane ; Juhász, György ; Major, Csaba ; Petrik, Péter ; Kálvin, Sándor ; Horváth, Zoltán György ; Fried, Miklós Multi-color ellipsometric mapping tool from cheap parts PROCEEDINGS OF SPIE - THE INTERNATIONAL SOCIETY FOR OPTICAL ENGINEERING 12428 pp. 134-141. , 8 p. (2023) IF: 0.28

Nugusse, Berhane ; Juhász, György ; Major, Csaba ; Petrik, Péter ; Kálvin, Sándor ; Horváth, György Zoltán ; Fried, Miklós "Optical calibration of the ellipsometric mapping tool from cheap parts" In: Fried, Miklós (szerk.) Symposium on Materials Science 2024 Mátraháza, Magyarország : Óbudai Egyetem (2025) 39 p. pp. 26-32. , 7 p.

Nugusse, Berhane ; Juhász, György ; Major, Csaba ; Petrik, Péter ; Kálvin, Sándor ; Horváth, Zoltán György ; Fried, Miklós "Multi-color ellipsometric mapping tool from cheap parts" In: Fried, Miklós (szerk.) Symposium on Materials Science 2022 Budapest.

2. Theoretical background

Consider an electromagnetic wave of initial wavelength (λ) and electric field of magnitude (E_0) in free space, incidents on two different materials, one transparent and the other light absorbing medium, as shown in Figure 2.1 (c) and (d) [2].

In the case light transmission through the transparent medium, the initial wavelength and magnitude of the electric field reduce to λ/n and E_{to}, respectively, where E_{to} indicates magnitude of the electric field in the transparent medium and n the refractive index of the medium.

Note that, the propagation of electromagnetic waves in a transparent medium is completely determined by the refractive index of the medium though which it advances [2], where the extinction coefficient (k) of the medium is zero.

However, when the same electromagnetic wave advances into a light absorbing medium, the phenomenon cannot be completely explained without the introduction of the extinction coefficient.

In Figure 2.1 d), the initial wavelength reduces to λ/n and the amplitude E_0 decays exponentially as a function of $\exp(\frac{-2\pi kx}{\lambda})$ along the direction of the wave propagation, x-axis in this case. As Fujiwara [2] noted**,** spectroscopic ellipsometry offers a very high precision allowing a reliable thickness measurement of up to $5d_p$.

Penetration depth (d_p) is the distance up to which an electromagnetic wave of light advancing into the material reduces to $\frac{1}{e}$, about 36.8% of its original value at the surface of the material.

At this point, $\alpha d = 1$

Where,

'α' and 'd' are the absorption coefficient of media and the distance from the surface (now the penetration depth, d_p) respectively.

Therefore, the refractive index (n) and the extinction coefficient (k) of a material are significant parameters in ellipsometric material characterization. Figures 2.1. a) and b) respectively illustrate a typical relation of n and k for a crystalline silicon as a function of the electromagnetic wavelength and the corresponding dependence of p-and s-reflectance components on the angle of incidence.

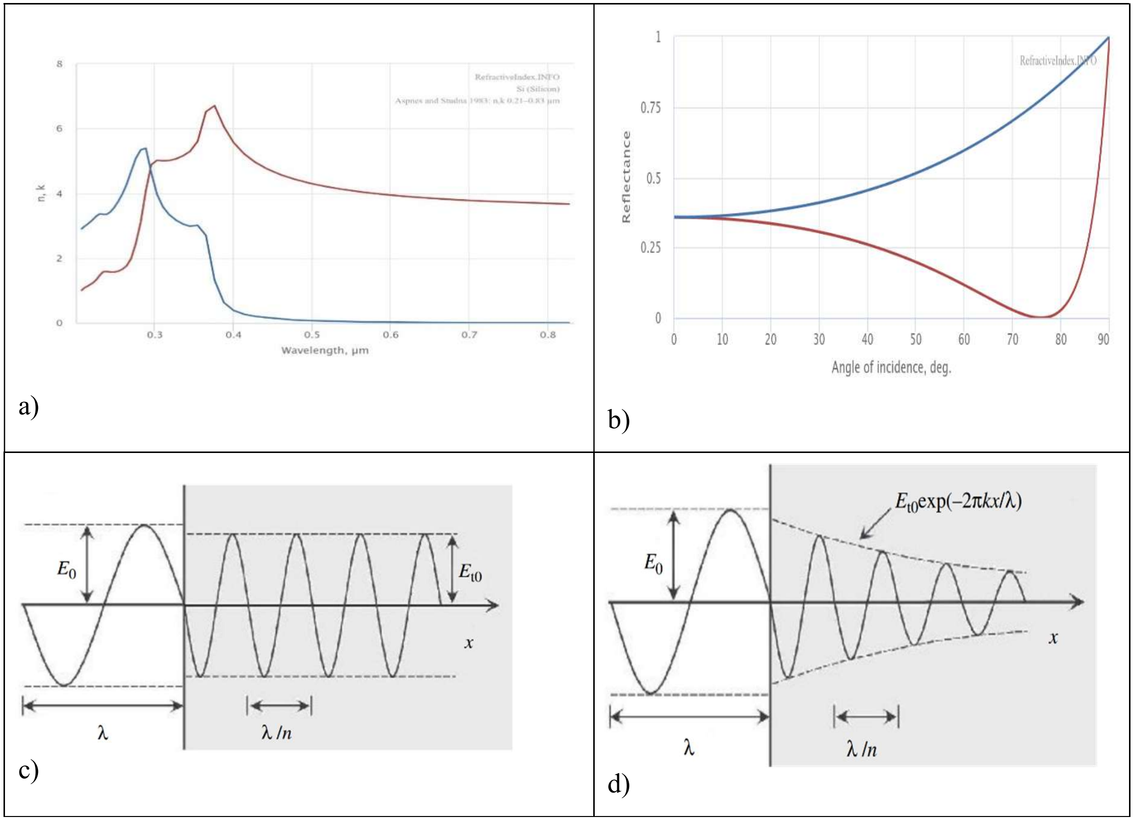

Figure 2.1. Relation between refractive index and extinction coefficient of a medium

a). Refractive index and extinction coefficient versus wavelength for a crystalline Silicon [48] [49].

b). Reflectance (R_P: blue curve, R_S: red curve) for a crystalline silicon versus an angle of incidence [48].

c). Propagation of electromagnetic waves in a transparent medium, where k=0

d). Propagation of electromagnetic waves in a light-absorbing medium, where k > 0 [2].

Notice that, Reflectance(R) is the intensity ratio of the reflected light to the incident light, which are going to be discussed in details latter.

When a linearly polarized light obliquely incidents on a sample surface and a relative change in polarization state takes place, it is characterized by two components depending on the oscillation of its electric field orientation: the p-polarized and the s-polarized light. As shown in Figure 2.2, the p-polarized light is the one, whose electric field component`s incident and reflected waves oscillate on the plane of incidence, a plane normal to the surface of the sample. In contrast, the s-polarized light electric field component oscillates normal to the plane of incidence.

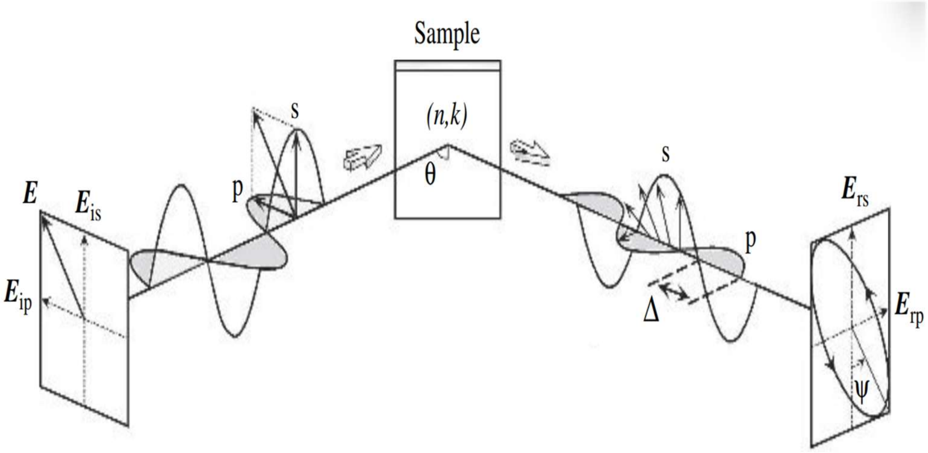

Figure 2.2. Elliptical polarization of a measurement beam [2].

Ellipsometry measures the amplitude ratio, tan (ψ), and the phase difference, delta (Δ), between the p-polarizations and the s-polarizations [1], which depend on the wavelength of the light beam (λ) and the angle of incidence of the beam (θ) with respect to the normal surface of the sample, respectively. See Figure 2.2.

In case of simplified structures, the refractive index (n) characterizes the amplitude ratio, where as extinction coefficient (k) determines the phase difference that represents light absorption [1].

In case of light reflection, the measured amplitude ratio tan (ψ) and phase difference (Δ) from ellipsometry are defined from the ratio of the amplitude reflection coefficients for p- and s-polarizations.

In ellipsometry the angle of incidence (θ_0) is usually set at the Brewster angle [2]. The Brewster angle (θ_B) is the angle of incidence at which the reflection of p-polarized light is theoretically zero at the interface between two non-absorbing dielectric media.

Brewster's Law: For reflection between two transparent, non-absorbing dielectric media with refractive indices n_1 and n_2, the Brewster angle θ_B is related as,

$$\tan \theta_B = \frac{n_1}{n_2} \tag{1}$$

The angle of incidence is typically chosen to be close to the Brewster angle of the substrate to attain mainly maximum sensitivity and optimal measurement [2].

Note that:

Maximum Sensitivity: The difference between the reflected amplitudes of the p-polarized (r_p) and s-polarized (r_s) light is maximized near θ_B.

Optimal Measurement: This maximum difference leads to the largest change in the ellipsometric parameters (ψ and Δ), which in turn provides the greatest sensitivity for determining the thickness and optical constants of a thin film deposited on that substrate.

The schematic diagram for the optical interference in an ambient/thin film/substrate optical model is given below.

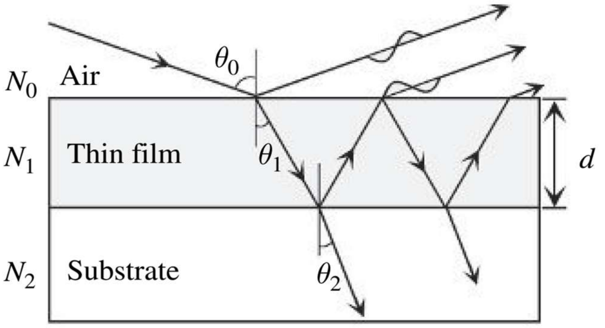

Figure 2.3. The schematic diagram for the optical interference in an ambient/thin film/substrate optical model [1].

In figure 2.3., θ_o is the angle of incidence in the air medium (N_o), where as θ_1 and θ_2 are the transmission angles in the thin film (N_1) and substrate media (N_2), respectively. These angles are related by the Snell`s law,

$$n_j \sin\theta_j = n_k \sin\theta_k \tag{2}$$

In case of complex refractive indices, Snell`s law becomes,

$$N_j \sin\theta_j = N_k \sin\theta_k \tag{3}$$

Where, $N=n-ik$, (4)

N represents the complex refractive index of a given medium and the imaginary number, $i=\sqrt{-1}$.

Note that for perfectly transparent materials (non-absorbing films) where the extinction coefficient k=0, equation (3) reduces to equation (2) [52].

In equation 3, N_j and N_k are complex refractive indices of the jth and kth layer in the formulated optical model, with their corresponding angles θ_j and θ_k, now complex numbers, respectively.

For example, for the air/thin film analysis in figure 2.3, the subscripts j=0 and k=1.

In case of the thin film/substrate, j=1 and k=2.

For a demonstration, the relation between the refractive index (n) and the extinction coefficient (k) versus wavelength (μm), for a crystalline silicon sample is depicted in Figure 2.1. a), from the D. E. Aspnes and A. A. Studna dielectric functions and optical parameters of materials database [49].

For a given wavelength of light (λ), the extinction coefficient (k) of a material is also related to its absorption coefficient (α) , a physical measure that describes how quickly light intensity is attenuated in a material, where;

$$\alpha = \frac{4\pi k}{\lambda} \tag{5}$$

The absorption coefficient is often used to describe the exponential decay of an incident light intensity I_0 into a material. The transmitted light intensity I, after travelling a distance of, x, in the given medium is given as,

$$I(x) = I_o \exp^{(-\alpha x)} \tag{6}$$

The above equation is called the General Attenuation Law or the Bouguer–Lambert Law. Equation 6 is graphically represented in figure 2.1 d), recalling that the electric intensity (I) is directly proportional to the square of the associated electric field amplitude (E) in the given medium.

For conducting materials, the relation between the complex refractive index (N) complex dielectric constant (ε) is given by Maxwell's equations and is given as,

$$N^2 = \varepsilon \tag{7}$$

Given that, $$\varepsilon = \varepsilon_1 - i\varepsilon_2 \tag{8}$$

After combining equations 7 and 8 and some mathematical manipulations, these parameters can explicitly be expressed as follows,

$$\varepsilon_1 = n^2 - k^2 \tag{9}$$

$$\varepsilon_2 = 2nk \tag{10}$$

$$n = \left\{ \left[\varepsilon_1 + \left(\varepsilon^2{}_1 + \varepsilon^2{}_2 \right)^{1/2} \right] / 2 \right\}^{1/2} \tag{11}$$

$$k = \left\{ \left[-\varepsilon_1 + \left(\varepsilon^2{}_1 + \varepsilon^2{}_2 \right)^{1/2} \right] / 2 \right\}^{1/2} \tag{12}$$

It should be noted that the complex dielectric function ε of a material defines the overall response of the material to an electric field, and the relationship between the complex dielectric functions, ε_1 and ε_2, is governed by the fundamental Kramers-Kronig (KK) equations [2].

Any analytical dispersion model used to fit the SE data (such as Tauc-Lorentz, Drude) must be intrinsically Kramers-Kronig consistent because ε_1 can be calculated from ε_2 (and vice-versa). This consistency provides a crucial constraint, guaranteeing that the final extracted parameters are physically feasible [54].

The dispersion (or polarizability) of the material is represented by the real part ε_1. It explains how the material stores energy from the electric field, which controls the phase velocity of light in the medium and is strongly correlated with the refractive index (n).

On the other hand, the absorption (or dissipation) of energy from the electric field is represented by the imaginary part ε_2. For ideal transparent materials, ε_2 is zero and it is proportional to the extinction coefficient (k).

In case of optical interference in different media, like the one in figure 2.3, an ambient/thin film/substrate optical model, the phenomenon can be well explained by the Fresnel`s equations.

The Fresnel`s equations are given as,

$$\boldsymbol{r_{jk,p}} = \frac{N_k cos\theta_j - N_j cos\theta_k}{N_k cos\theta_j + N_j cos\theta_k} \quad \boldsymbol{r_{jk,s}} = \frac{N_j cos\theta_j - N_k cos\theta_k}{N_j cos\theta_j + N_k cos\theta_k} \tag{13}$$

$$\boldsymbol{t_{jk,p}} = \frac{2N_j cos\theta_j}{N_k cos\theta_j + N_j cos\theta_k} \quad \boldsymbol{t_{jk,s}} = \frac{2N_j cos\theta_j}{N_j cos\theta_j + N_k cos\theta_k} \tag{14}$$

Where,

r_p and r_s are the reflection coefficients for p-polarized light and s-polarized light respectively.

N is the complex refractive index of a given medium.

‘r’ and ‘t’ are the complex reflection coefficient and complex transmission coefficient respectively, for each p- and s-polarized lights

‘j’ and ‘k’ subscripts represent corresponding parameter values in case of air, thin film or substrate reflection or transmission of the light.

'θ_j' and 'θ_k' are the angle of incidence and angle of transmission respectively .

Besides, for each p and s-polarized lights, the relation between the reflectances (R_p and R_s) and the reflection coefficients (r_p and r_s) are given as follows,

$$R_P = \left(r_p\right)^{1/2} \text{ and } R_S = \left(r_s\right)^{1/2} \tag{15}$$

The ratio of the amplitude reflection coefficients for p- and s-polarizations, r_p and r_s respectively, define the measured ellipsometric angles, the amplitude ratio and the phase difference. They are related as,

$$\rho = \tan(\Psi)\exp(i\Delta) = \frac{\boldsymbol{r_p}}{\boldsymbol{r_s}} \tag{16}$$

Equation 16 is often called the fundamental equation of spectroscopic ellipsometry.

In case of light transmission, the relation is given as,

$$\rho = \tan(\Psi)\exp(i\Delta) = \frac{t_p}{t_s} \tag{17}$$

Where,

ρ (rho) is the complex refraction ratio

tan (ψ) and Δ (delta) ,often called ellipsometric angles, represent the amplitude ratio and the phase difference of the measurement beam respectively.

As previously stated, SE technique is an indirect measurement optical technique that measures the change in the polarization state of the measurement beam. Accordingly, the measured ellipsometric values, Ψ_{exp} and Δ_{exp} do not directly give the required parameters of interest like the thin film thickness, roughness or the materials optical constant (n, k). In parallel to this, the theoretical ellipsometer values Ψ_{cal} and Δ_{cal}, computed mainly from the Fresnel's equations in relation to the constructed structural and optical model, do not give the parameters of interest either. It is after some regression computer algorithm analysis of these combined two data sets, iteratively adjusts the model parameters (the "fit parameters") to minimize the difference between the experimental data and the theoretical data [55].

The mean square error assesses the goodness of fit between the model-generated data and the experimentally measured data over the entire range of wavelengths and angles of incidence. The optimization process involves iteratively adjusting the model`s unknown parameters vary until the minimum MSE is achieved.

The most common widely used form of the MSE is given below [56].

$$MSE = \sqrt{\frac{1}{2N-M}\sum_{i=1}^{N}[(\frac{\psi_i^{\exp}-\psi_i^{calc}}{\sigma^{\exp}_{\psi,i}})^2+(\frac{\Delta_i^{\exp}-\Delta_i^{calc}}{\sigma^{\exp}_{\Delta,\mathrm{i}}})^2]} \qquad (18)$$

Where,

N Number of experimental data points (the total number of measured pairs (Ψ, Δ) across all wavelengths and angles).

M Number of variable model parameters (The values the regression adjusts, such as layer thicknesses, band gap energies, etc.).

i Index for each measurement point (each wavelength/angle combination).

$\Psi_i^{\exp}$ and $\Delta_i^{\exp}$ Experimental (measured) ellipsometric values at the i^{th} point.

Ψ_i^{calc} and Δ_i^{calc} calculated (model generated) ellipsometric values at at the i^{th} point.

$\sigma_{\Psi,i}$ *and* $\sigma_{\Delta,i}$ Standard deviation (experimental error) of the measured Ψ and Δ at the i^{th} point.

$\frac{1}{2M-N}$ Normalization Factor that accounts for the number of data points (2N) and the degrees of freedom (M). This makes the MSE an unbiased estimate of the variance.

The inclusion of the standard deviations (σ values) in the denominator is critical. This means that a deviation between the model and experiment is weighted less if the experimental measurement at that point was less precise (in case of a larger σ). This gives a statistically rigorous measure of the fit quality.

A "good" MSE value is usually close to 1.0, especially when using the normalized form above, that indicates the differences between the model-generated and experimental data are approximately equal to the expected experimental error.

During MSE iteration, is good to give the best guess of an initial values, like thin film thickness, and manually scan the result of the MSE values. Sometimes, the MSE estimator algorithm sees that any small step away from a local minimum results in a higher MSE and stops without finding the global minimum.

Briefly, a local minimum is any other low point on the surface (a "valley") that is lower than the surrounding area, but not the lowest point overall. It represents a mathematically plausible, but physically incorrect solution. In contrast, the global minimum is the absolute lowest point on this entire surface. It represents the true physical solution, the combination of thickness and properties that most accurately describes your sample.

Generally, physically unrealistic or very high MSE values may rise from inaccurate measured ellipsometric spectra, dielectric functions, optical model or a depolarization effect in the sample [2].

3. Literature Review

3.1. Ellipsometry - Spectroscopic ellipsometry theory and instrumentation

The development of photovoltaics, display technologies, semiconductor production, and protective coatings is made possible by thin films, which constitute the foundation of contemporary technology. The lateral homogeneity of the film's thickness, composition, and morphology over sometimes meter-sized surfaces is a crucial component in the performance and yield of these applications. Petrik and Fried [11] point out that scaling-up conventional thin film measuring methods to describe these vast surfaces is a major problem that necessitates a redesign in order to achieve high-speed, non-destructive, and in-line capable configurations.

In-depth thin-film characterization techniques based on sputtering depth profiling, complex modelling based on nondestructively measured whole-depth data, or destructive and time-consuming cross-section preparation are all sufficiently developed to only need minor adjustments and enhancements for new tasks like imaging or mapping on small or large area mapping. Only a few number of those techniques are able to gather the quantity of data required for big area measurements in a reasonable length of time due to inherent characteristics. A study conducted by Abou-Ras et. al. [15], shows the comparison between different collective techniques used during thin-film characterizations, as briefly discussed below.

i). depth-profiling by sputtering (e.g., secondary ion mass spectrometry [SIMS], secondary neutral mass spectrometry [SNMS], X-ray photoelectron spectrometry [XPS], Auger electron spectrometry [AES], glow-discharge optical emission spectrometry [GD-OES], glow-discharge mass spectrometry [GD-MS], Raman depth profiling)

ii). non-destructive techniques (e.g., spectroscopic ellipsometry [SE], Rutherford backscattering spectrometry [RBS], elastic recoil detection analysis [ERDA], X-ray diffraction [XRD], angle-dependent X-ray emission spectroscopy [AXES]), and

iii). Cross-section micro (Nano) mapping (e.g., transmission electron microscopy [TEM], its combination with energy dispersive X-ray analysis [EDX], scanning Auger electron microscopy, Raman mapping, time of flight SIMS [TOF-SIMS]).

Sputtering-based depth-profiling and cross-sectional methods require a long measurement time and tedious sample preparation; therefore, they are not capable of large area mapping. Non-destructive methods such as SE, RBS, ERDA, and AXES require a few minutes or even a few times ten minutes for taking a spectrum at one spot. However, the measurement time of some optical configurations can be reduced to even a few seconds per spot, or a few minutes for a completely mapped or imaged area if using simultaneous measurements at all illuminated lateral positions.

3.2. Mapping - Imaging Ellipsometry

The established industrial method, as detailed by Petrik and Fried [11], involves moving the ellipsometer's source and detector units in a specular reflection configuration over the surface, or moving the substrate itself in a roll-to-roll (RtR) process. This point-by-point approach is robust and widely used, for instance, in optimizing photovoltaic panels by mapping the thickness and bandgap of multilayer structures like CdS/CdTe, see Figure 3.2. The drawback is that measurement time scales directly with the number of points; characterizing a large panel with thousands of points can take hours, making it less ideal for high-throughput production environments.

3.2.1. Large area Scanning or Mapping

As previously briefly stated, the Semilab FPT (Flat Panel Testing) system [40] and the Woollam AccuMap are both industrial systems designed to support large-area thin film metrology but in a different industrial ranges.

The Semilab FPT series, like FPT-500, FPT- 600, FPT-800, are explicitly designed for large area thin films mapping across wafers, glass substrates and photovoltaic panels.

These Semilab FPT system combines mainly spectroscopic ellipsometry, reflectometry, optical profilometry and sheet resistance mapping, enabling the system to full-area uniformity analysis of optical and physical properties of thin films. Large area PV coatings, up to a meter-scale, and semiconductor thin films can be studied using these system tools.

The J.A. Wollam AccuMap systems in contrast focuses in higher speed mechanical scanning on large-area ellipsometric and reflectometric mapping techniques. It focuses mostly on wafer-scale like large glass substrates but on a relatively smaller mapping area scale, compared to that of the Semilap FPT systems.

[41].During conventional ellipsometric mapping, data collection is relatively slow and uses a small scanned spot. We know two industrial systems which are capable of measuring big (square-meter size) samples: the Semilab FPT system [40] and the Woollam AccuMap [41].

Figure 3.1. AccuMap SE (Left) and Semi-lab FPT system (Right)

Both systems use a “traditional” SE device (100k USD price) in special big moving/scanning systems, measuring the big samples point by point. The Woollam brochure states that “Data Acquisition Rate: <6 s per point (includes time for movement to new point, automated alignment, and data collection)” so it can measure one big area during several 10 minutes.

As previously mentioned, ellipsometry determines angle of incidence dependent relative amplitude ratios and phase difference shifts of orthogonal electric field components typically defined as parallel and perpendicular to the plane of incidence upon specular reflection of light from a planar surface. [2] Thus, collimated light beams are conventionally used with a well-defined angle of incidence at the reflecting surface. An established method for large-area mapping has been to move both the source and detector units of an ellipsometer in a specular reflection configuration over the surface. This is a widely used standard method for measuring large panels (e.g., solar or display with sizes even over meters) in industrial projects [42][43]. When measuring in a roll-to-roll (RtR) configuration, the movement of the substrate can also be used as a means of moving the spot on the surface [16]. A typical application of point-by-point mapping is photovoltaic (PV) because the quality of panels is largely dependent on the lateral uniformity. Razooqi Alaani et. al. [17] showed an example of PV optimization by mapping using the CdS/CdSe/CdTe multilayer structure Figure 3.2(a–d) and Figure 3.3 (a-d). The goal was to optimize the performance of the devices by correlating cell parameters with these two effective thicknesses. Measuring one point does not take more than a few seconds even using spectroscopy; however, it adds up to tens of minutes when measuring hundreds of points.

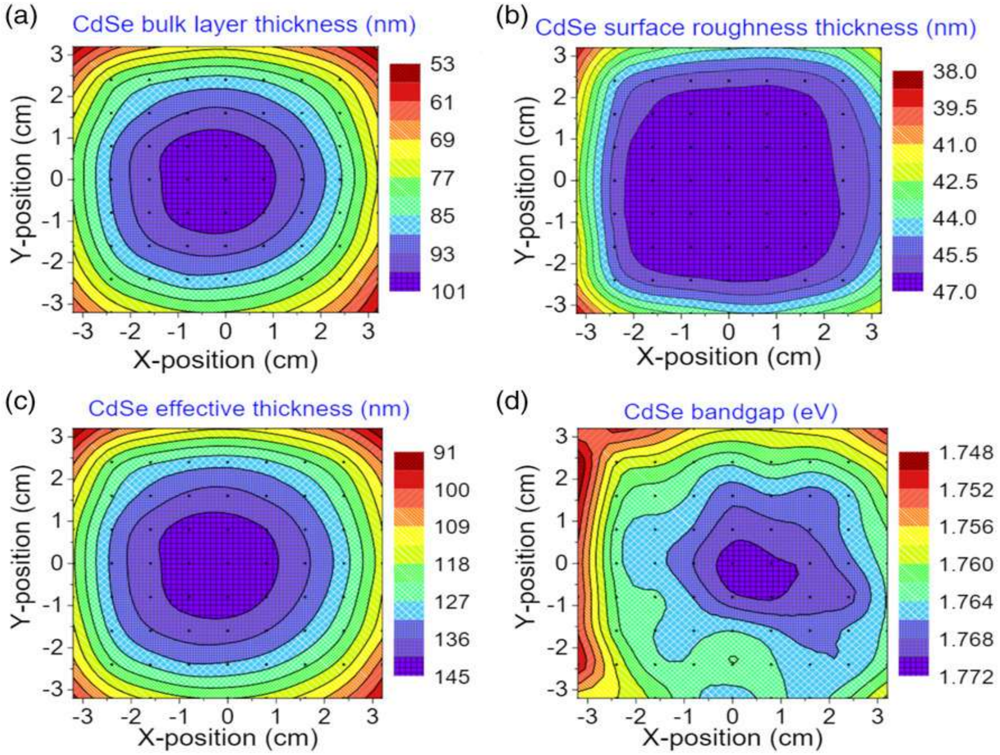

Figure 3.2. Maps over an area of 6.5 cm × 6.5 cm for a CdSe calibration film with an intended effective thickness of 145 nm deposited on a TEC™15/HRT substrate at a room temperature [17].

(a) bulk layer thickness (b) surface roughness layer thickness

(c) effective thickness, and (d) bandgap

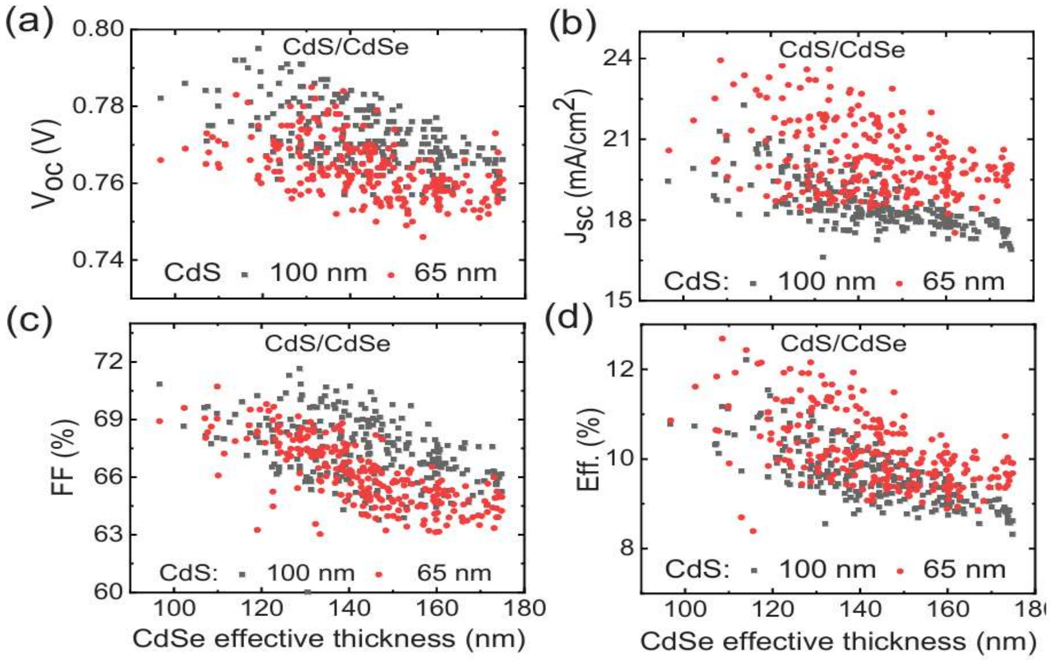

Figure 3.3. Correlations between Mapping-SE calibration of CdSe effective thickness at the precise solar cell location and the solar cell parameters.

(a) pen-circuit voltage Voc, (b) short-circuit current density Jsc, (c) fill-factor (FF) and (d) efficiency for solar cells fabricated with maximum CdS effective thicknesses of 65nm and 100 nm and a maximum CdSe thickness of 175 nm.

The low thickness range of the data set for 100 nm CdS overlaps with the maximum thicknesses of the data set for the 65 nm CdS [17].

3.2.2. Small Area Scanning or Mapping

Dynamic Imaging Micro-ellipsometry (DIM) is a rapid, high-resolution, full-field mapping/imaging ellipsometric technique [18] which uses focused monochromatic (laser) light to achieve high lateral resolution. The basic approach of combining an optical system derived from conventional ellipsometry with video and image processing has been retained. The DIM system can use a Polarizer, Compensator, Specimen, and Analyzer (PCSA) optical system or a Polarizer, Half-wave plate, Specimen, Compensator, and Analyzer (PHSCA) configuration. The polarization rotation is usually under direct computer control, enabling automated operation that greatly facilitates statistical analysis of the instrument’s response.

A special measuring technique is Fourier scatterometry [19], when a focused spot is created by a high numerical aperture (NA) microscope objective (MO), and the scattered illumination is collected by the same MO. In this configuration, each point of the back focal plane of the MO is uniquely related to a given reflection and azimuth angle. Fourier scatterometry allows the measurement of small and weakly reflecting samples over a wide range of reflection angles. Using high-NA MOs, the angles of reflection cover the range from 0 to over 70 (72 for NA=0.95), and the distance of the objective is only several hundred wavelengths from the sample surface. The whole back focal plane image that includes the response of the sample at all conical angles can be recorded within less than a second.

By using coherent illumination and a scanning focused spot, the phase can be modulated and the phase difference between the overlapping orders can be determined [20], increasing the sensitivity as compared to phase-insensitive incoherent Fourier scatterometry. A further advantage of the coherent illumination is that the size of the focused spot is much smaller (below one micron in the visible wavelength range). The performance of coherent Fourier scatterometry can further be increased by combining it with interferometry [21]. Using interferometry, the complete scattering matrix is evaluated. The absolute phase distribution of the diffracted orders is retrieved using a known reference beam. The ellipsometric approach can be considered as a variation of the interferometric method, in which the reference beam for one polarization is that of the orthogonal polarization about the plane of incidence.

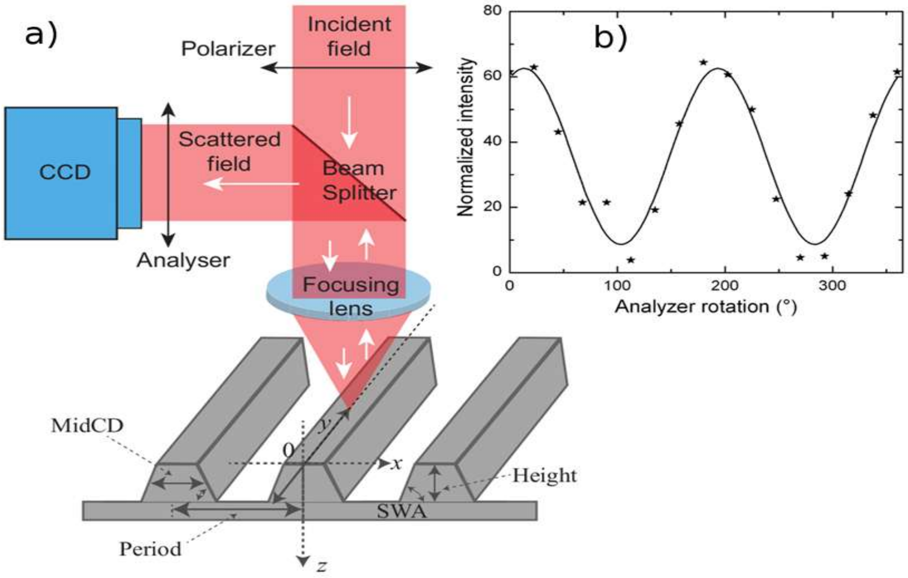

Figure 3.3. (a) Setup of ellipsometric Fourier scatterometry. (b) Intensity signal at an arbitrary pixel of the CCD as a function of polarizer rotation at the output side [22].

Figure 3.3 illustrates an extension of Fourier scatterometry, aiming at increasing the sensitivity by measuring the phase difference between the reflections polarized parallel and perpendicular to the plane of incidence. The ellipsometric approach requires no addition-al hardware elements compared with conventional Fourier scatterometry. Furthermore, incoherent illumination is also sufficient, which enables spectroscopy using standard low-cost light sources [22]. The advantages of ellipsometry over other approaches are that a simple hardware can be used, there is no need to measure the input wave front parameters, incoherent illumination is sufficient, enabling the use of spectroscopy with conventional light sources.

3.2.3. Large Area Imaging

Although micro-imaging ellipsometry is a well-established technique [23-25], so far much fewer efforts have been made for large-area imaging of thin films. Our Laboratory proposed a divergent light source configuration for large-area imaging [26]. Using this arrangement, the surface is illuminated from a divergent point source, and the reflection from the measured surface is imaged by a spherical or parabolic mirror and correction optics to a charge-coupled device (CCD). All the pixels on the CCD correspond to one point of the sample surface. The modulation of the polarization creates a periodic variation of the intensity in each pixel, from which the map of (Ψ, Δ) pairs can be determined at the given wavelength of illumination. Spectroscopic macro-imaging ellipsometry can only be realized in this configuration by measuring maps at different wavelengths one by one.

The "pinhole version" of this kind of instrument uses an illumination by an almost diffuse, "divergent beam" of light that provides a collection of rays with diverse angles of incidence at every point of the sample. Precise "angle-selection" is performed on the detector side by a pinhole camera (Fig. 3.4). The pinhole works as an "angle-of-incidence filter," selecting only one light beam from every direction (or sample position) [27-29].

The arrangement of divergent light source ellipsometry [10] can be seen in Fig. 3.4, where the white light source, narrow rectangular aperture, compensator and film polarizer make a single set (indicated from 1-4 respectively) , spherical mirror(5), sample (6), then the cylindrical mirror-corrected beam, analyzer, pinhole and correction–dispersion optics (indicated from 7-10 respectively) form another single set with a separate CCD detector array (11).

Spectroscopy can also be realized by measuring along a single line using the second dimension of the CCD as the spectroscopic direction, whenever there is a possibility of moving the substrate. Here, each point of a line can be measured simultaneously in a spectroscopic way. By moving the sample, a 2D map is created, in which each point includes a spectroscopic measurement [30].

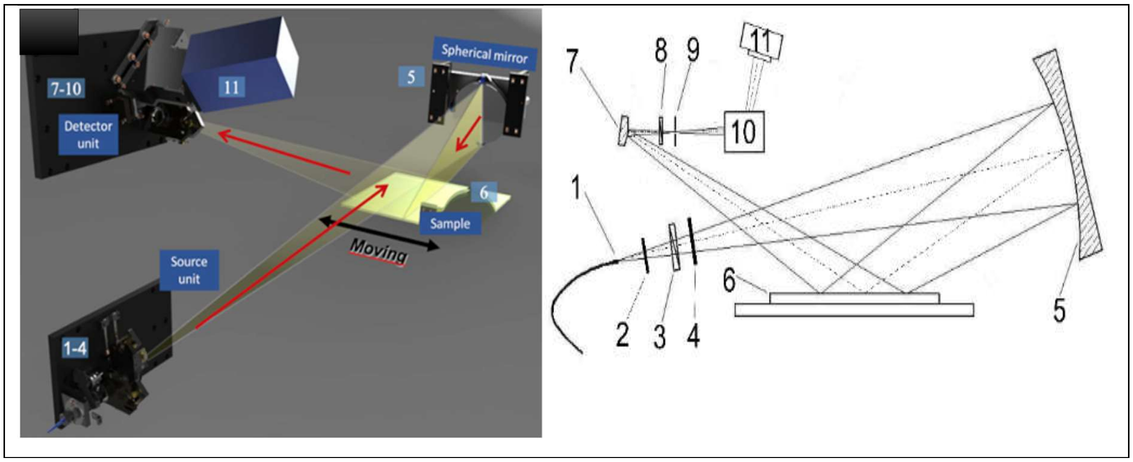

Figure 3.4.Picture (left), and Schematics (right) of the large area-imaging tool using a divergent light source.

(1) "White" light source, (2) narrow, rectangular aperture, (3) film-polarizer, (4) compensator, (5) spherical mirror (6) sample, (7) cylindrical mirror, corrected beam, (8) analyzer, (9) pinhole, (10) correction-dispersion optics, (11) CCD detector array [10].

As shown in Figure 3.5 and 3.6, several prototype expanded-beam spectroscopic ellipsometers have been developed that use uncollimated (non-parallel, diffuse) illumination with a detection system consisting of an angle-of-incidence-sensitive, pinhole camera for high-speed, large-area imaging/mapping applications [31].

Figure 3. Large area imaging tool prototype for a 300 mm sample size [31].

Figure 4. Large area imaging tool prototype for 450-600 mm sample size [31].

Notice that there is a robotic arm at the left side of the above imaging device photo.

3.2.3.1. Roll-to-Roll thin film photovoltaics-like sample

A 15-cm sample-size expanded-beam spectroscopic ellipsometer was applied for in-situ, high-speed imaging/mapping analysis of large area spatial uniformity for multilayer-coated substrates in Roll-to-Roll (RtR) thin film photovoltaics (PV) [30].

The instrument allows for imaging width-wise and mapping length-wise for uniformity evaluation at the high linear substrate speeds required for real-time, in-situ, and on-line analysis in RtR thin film PV: Ag, ZnO, and n-type hydrogenated amorphous silicon (a-Si:H) layers of an a-Si:H n-i-p structure deposited on a flexible polyimide substrate in the RtR configuration. Prototype for 150 mm sample-size, located within the Center for Photovoltaics Innovation and Commercialization at University of Toledo (Ohio).

Spectroscopic ellipsometry data across a line image was collected as the substrate was translated by a roll-to-roll mechanism. A coated area of 45 cm × 12 cm was analyzed in this study for layer thickness and optical properties by applying the appropriate analytical models for the complex dielectric functions of the Ag, ZnO and n-type Si:H layers [30].

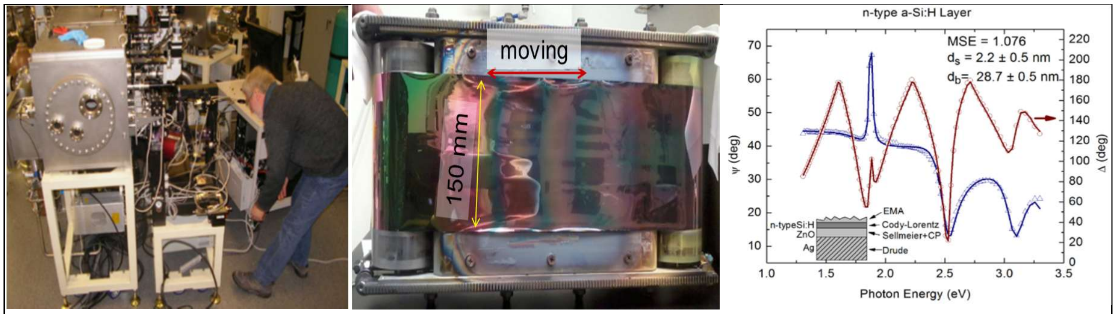

Figure 5. Expanded-beam ellipsometer multi-chamber cluster tool for in situ analysis (Left), a ZnO layer deposited by magnetron sputtering onto Ag-covered plastic foil in a cassette roll-to-roll model machine (center) and n-type a-Si: H layer best fit (right).

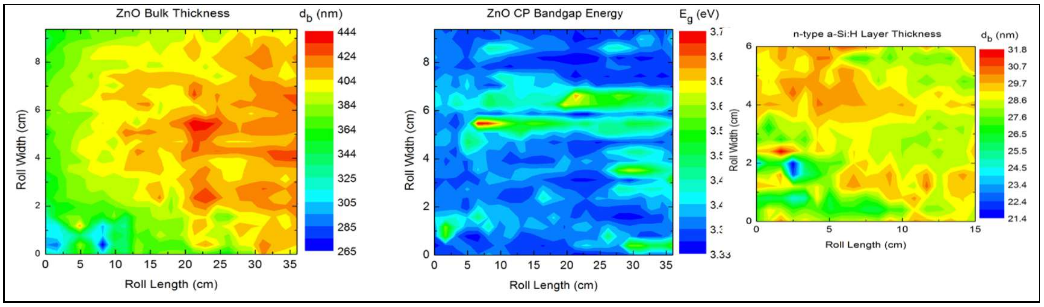

Figure 6.8. Thickness map for ZnO (left), the band gap critical point energy map for ZnO (center) and thickness map for n-type a-Si:H (right).

This tool is located within the Center for Photovoltaics Innovation and Commercialization University of Toledo (Ohio) and can measure a sample size of up to 150 mm.

Figure 3.7 shows the prototype that was integrated into a multi-chamber cluster tool for in-situ analysis and example of best fit (lines) to experimental (ψ, Δ) spectra (points) at a single point (Cody-Lorentz expression for the n-layer complex dielectric function) [30].

Map of the layer thickness, for ZnO, map of the band gap critical point energy for ZnO, and thickness map for n-type a-Si: H are shown in figure 3.8**.**

A prototype for 150 mm sample-size, located within the Center for Photovoltaics Innovation and Commercialization at University of Toledo (Ohio), has been integrated into a multi-chamber cluster tool for in-situ analysis. After a new layer deposition step the cassette roll-to-roll model machine (right picture) was moved back to the measuring chamber (without breaking the vacuum) and was measured again by the expanded beam mapping SE [30].

An a-Si/ZnO/Ag/plastic-foil structure was measured in two steps. First, the ZnO-layer was deposited onto the RtR sample and was measured. Second, the whole layer structure (after the a-Si deposition) the cassette roll-to-roll model machine was moved back to the measuring chamber (without breaking the vacuum) and measured again by the expanded beam mapping SE (Figure 3.7).

The speed of the measurement system makes the instrument suitable for use on production lines. The precision enables the detection of sub-nm thicknesses, and refractive index and extinction coefficient changes of 0.01. Alternative commercial instruments for SE mapping must translate the sample in two dimensions. Even a 15x15 cm2 sample with cm-resolution requires >200 measurements and at least 15 min. By imaging along one dimension in parallel, the expanded-beam system can measure with similar resolution in 1-2 min.

3.2.4. Small area Imaging

The first microscopic imaging ellipsometer which was constructed and published first in 1988. This imaging ellipsometer uses a CCD camera as a detector integrated with a frame grabber board in a PC [32].

One interesting application is micro-mechanically exfoliated mono- and multilayers of molybdenum disulfide (MoS_2) investigation by spectroscopic imaging ellipsometry, see Fig. 3.9. The complex dielectric functions from single and triple layers MoS_2 were determined, and the lateral homogeneity of the complex dielectric function for monolayer MoS_2 was investigated with a spatial resolution of 2 μm. Only minor fluctuations were observed, which could be caused by lateral modification in the van der Waals interaction caused by the preparation [33].

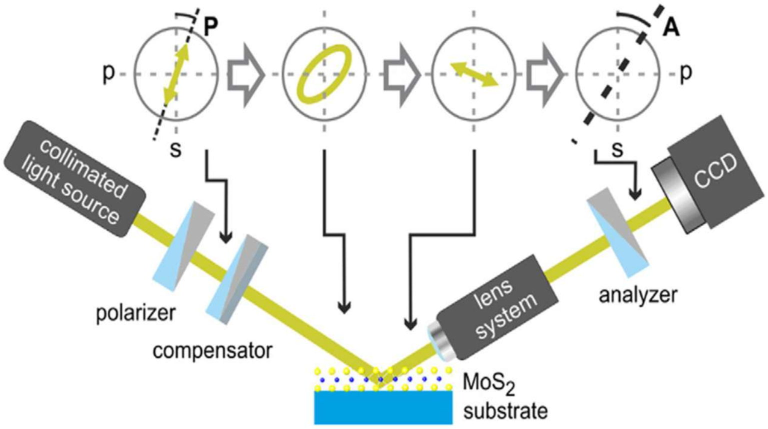

Figure 7. Small area imaging tool ellipsometry setup using a collimated light source [33].

a) Scheme of the small area imaging tool b) picture of the small area-imaging tool

* Scale bar: 50 µm

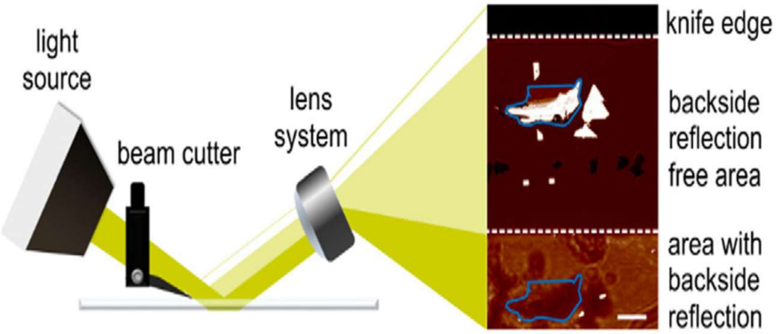

Figure 8. Beam cutter alignment between light source and sample, optional [33].

The polarizer-compensator-sample-analyzer configuration for the reflected light was used and the sample is illuminated by collimated light. The additional lens system between sample and analyzer allows imaging with micrometer resolution. The lateral resolution is only limited by the optical system on the detector side, defined by the lens system and the CCD-camera; see Figure 3.10. The optional beam cutter alignment between light source and sample utilizing a knife-edge suppresses effectively signal from reflections stemming from the backside of the transparent substrates. The picture on the right displays a large area view of the imaging ellipsometry contrast picture taken of a MoS_2 flake on double-sided polished sapphire using the beam cutter. In the dark region on top, the incoming light is blocked. In the middle area, reflections from the backside are selectively blocked with a sharp image of the MoS_2 flake and silicon alignment marker, while the lower part shows a blurred image of the MoS_2 flake that is a reflection from the flake on the backside of the substrate (scale bar denotes 50 μm).

4. Research Instrumentation and Methodology

4.1. Instrumentation and Experimental Setup

The Woollam M-2000DI rotating compensator spectroscopic ellipsometer is an optical mapping tool, upgraded to NIR (near infrared radiation), with a perfect combination of speed and accuracy. Measurements covering the entire spectral range from deep ultraviolet to near infrared are accomplished in seconds–making the M-2000 DI ideal for a large range of applications like quick quality control, real-time process monitoring and in situ control, uniformity mapping, and much more.

The Woollam M-2000DI ellipsometer is used with a perfect combination of speed and accuracy, as a control measurement, refer figure 4.1.

M2000DI Ellipsometer *g*eneral Specifications:

- Wavelength range of 191-1690 nm, corresponding to photon energies of 0.7-6.5 eV.
- Automatic scan over 15x15 cm area, with a micro-focused (ca. 0.2 mm) spot.
- Angle of incidence: 45-90 degree.
- Measurement time 1 sec per spot.
- Bandwidth about 10nm (NIR) with a rotation rate of 20Hz [39].

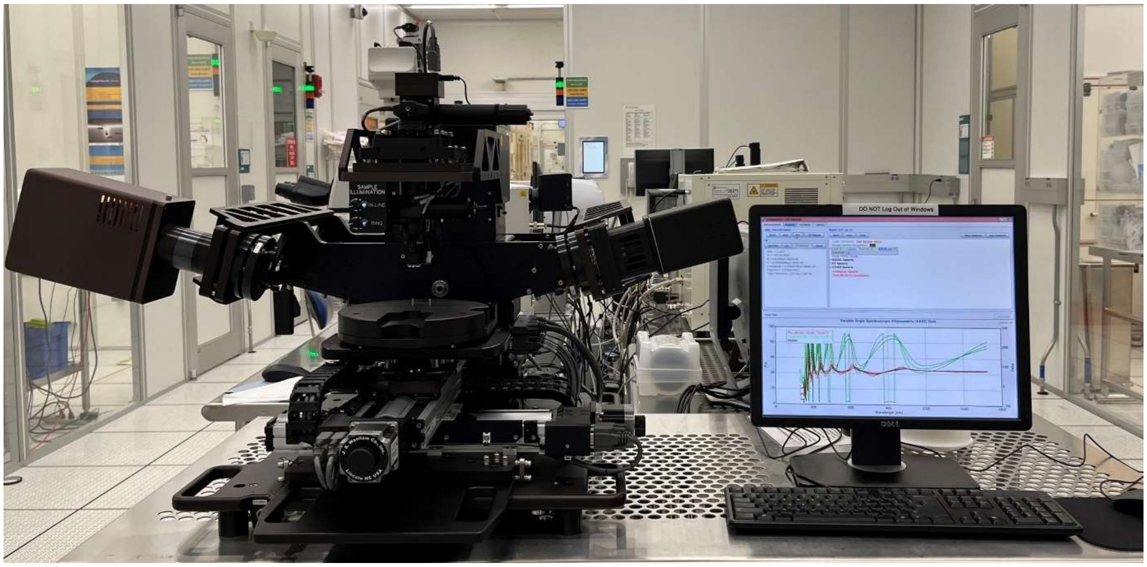

Figure 9 M2000DI J.A. Woollam Ellipsometer [58].

The J.A. Woollam Spectroscopic Ellipsometer (SE) system with the CompleteEase software installed is used to give out a very rich information about the optical properties, layer thicknesses and other related parameters of the sample, after a careful and detailed data analysis.

The optical constants of a given sample may include the refractive index (n), the extinction coefficient (k), dielectric function and absorption coefficient (α).

Similar measurements will help the calibration of the optical mapping tool prototype.

4.1.1. Prototype building using different parts

The original concept of the divergent beam-imaging device, Figure 4.2 below, consists of

1). Light-source (LED-panel) 2). Diffuser sheet

3). Film-polarizer 4). Analyzer

5). Detector (pin-hole + CCD-detector) 6). A Sample

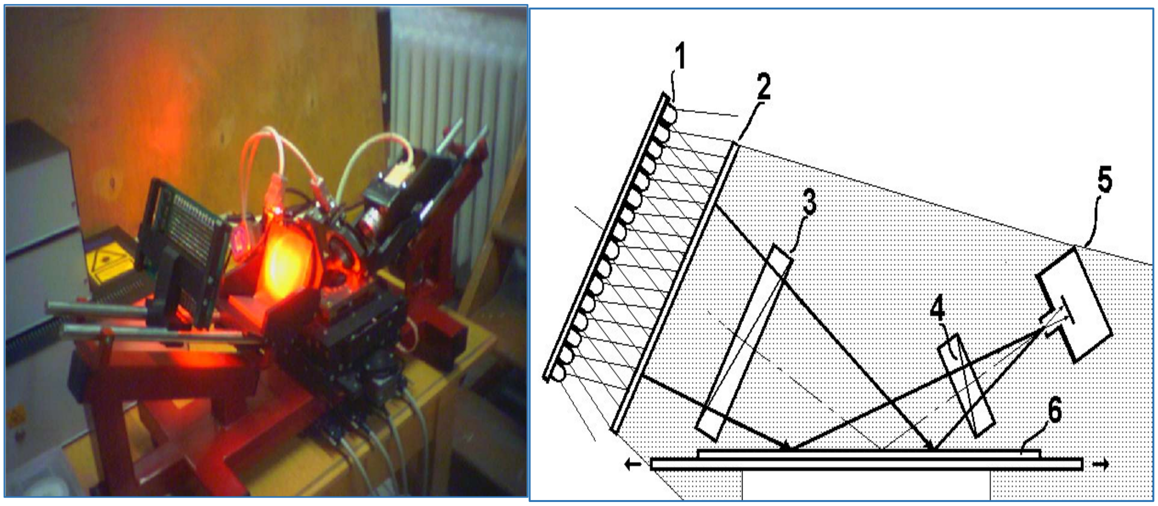

Figure 10 Original concepts of the non-collimated beam ellipsometer

The new concept of the optical mapping tool prototype is without the polarizers, which is going to be discussed next, in the experimental setup section.

4.1.2. Experimental Setup

The new concept of the non-collimated beam ellipsometer prototype is set up as shown in Figure 4.3 and Figure 4.4.

- **Light source**: LCD TV, serving as a polarized RGB color light source (built-in polarizer sheet) is used, ‘C’ in Fig. 4.4 and ‘1-4’ as a single set, in Fig. 4.3.

- **Sampling**: usually, different type of thin films samples, for example silicon dioxide on silicon wafer, 'B' in Fig. 4.4 and 5 and 6 in Fig. 4.3 (Sample and Sample holder respectively).

- **Detection System**: A polarization sensitive camera behind a pinhole, 0.2mm in diameter, is used. The polarization sensitive camera sensor serves the polarization state data from each position (plus three RGB colors in each position), 'A' in Fig. 4.4 and 7 and 8 in Fig. 4.3 (Pinhole and a polarization Camera sensor respectively**).**

The actual physical photograph experimental set up in our laboratory is shown in figure 4.4.

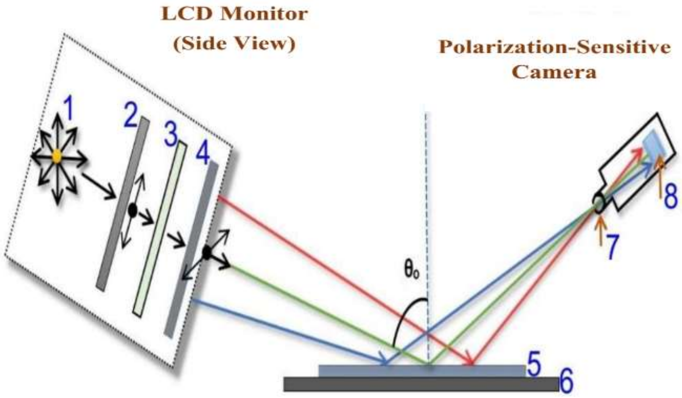

Figure 11 Schematic diagram of the non-collimated beam ellipsometer experimental setup

(Optical mapping tool from inexpensive parts)**.**

1**).** Light source	2**).** Vertical polarizer	3). Liquid crystal cell	4). Horizontal polarizer
5**).** Sample	6). Sample holder	7). Pin hole (sub-mm size)	8). Camera sensor

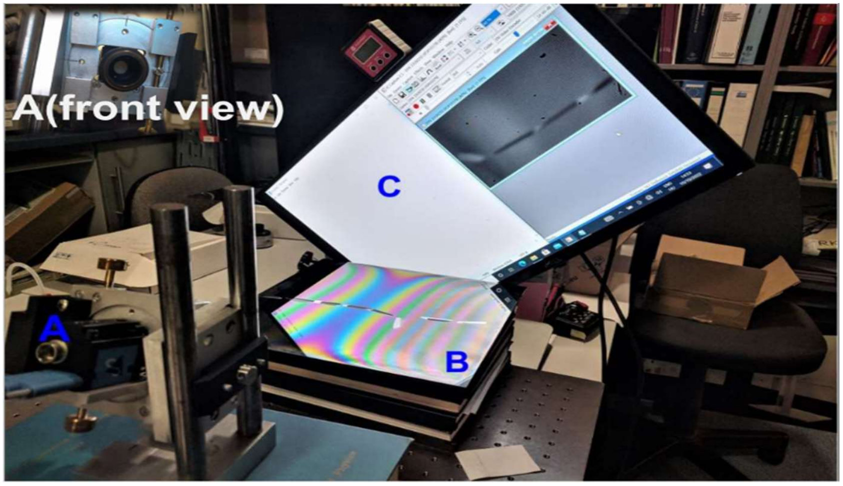

Figure 12 Experimental setup demonstration

A. Polarization sensitive camera B. Sample and Sample holder

C. LCD monitor (Dell UltraSharp™ U2412M, GB-LED, rotated into 45^0 position)

Our optical mapping tool consists of a polarization sensitive camera (The Imaging Source Company's DYK 33UX250 USB 3.0 Polarsens camera, a 2/3 inch Sony CMOS Pregius Polarsens sensor of model IMX250MYR Integrated with 4-Directional Wire Grid Polarizer Array) with a pinhole of sub-mm size in front of it. Besides, a Sample holder and an LCD monitor (Dell UltraSharp™ U2412M, GB-LED) as a light source for illumination of the selected sample. Detailed images are shown in the figure below.

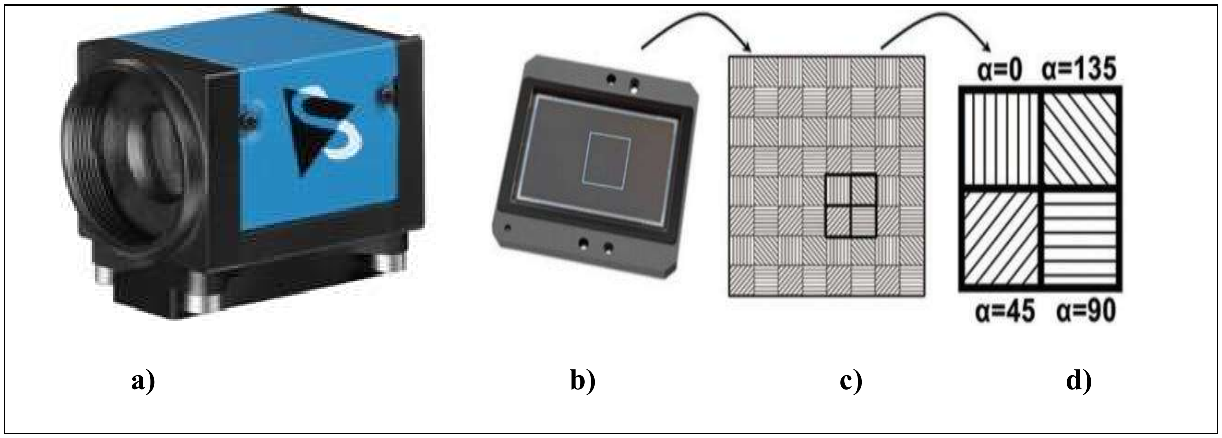

Figure 13. Schematic structure of a 2/3 inch Sony CMOS Pregius Polarsens sensor (IMX250MYR) [59].

a). Polarization sensitive camera **b)**. Camera sensor

c). Polarizer array matched to detector pixels and

d). Unit cell (Super-pixel), 2x2 pixel photodiodes

As shown in Figure 4.5 d), a super-pixel is a set of four neighboring pixels, each with different polarizer orientations, 0°, 45°, 90° and 135° [60].

Details on the specifications of the DYK 33UX250 USB 3.0 PolarSens camera is provided in Table 1, appendix.

Notice that, our optical mapping ellipsometer emits a non-collimated beam from the monitor screen as a source of light, despite most conventional ellipsometers usage of collimated light beams with a well-defined angle of incidence. Our arrangement shows similarity to the solution of Bakker et al [37], using a computer screen as a light source and a webcam as a detector in an imaging off-null ellipsometer. It is a noteworthy to mention that the basis of the work is a patent from our Institute, Horváth Z Gy et. al. [26].

The non-collimated beam ellipsometer set up is shown in Figure 4.3. An LCD -LED monitor serves the polarized RGB colored light, see the built-in polarizer sheet, number 4 in Fig. 4.3 and a polarization sensitive camera behind a pinhole (7&8) together.
In our large area mapping tool setup, the LCD-LED monitor (Dell UltraSharp U2412M, GB-LED backlight) is mechanically oriented at 45° relative to the sample plane. The alignment is measured using a digital angle gauge with a precision of 0.1°**.** When the LCD polarization axis is aligned in a straight-through configuration relative to the Polarsens (Sony IMX250MZR) polarization-sensitive camera, we can detect the extinction of the polarization sensitive camera better than 10^{-2}.

When the LCD monitor is rotated to a position where its output polarization is aligned parallel to the camera's analyzer direction, the detected intensity ideally reaches a minimum (extinction). In a perfect polarizer–analyzer pair, this would yield zero throughput**.**
The figure below shows the extinction ratio (ER) versus the wavelength of light, for the 2/3 inch Sony CMOS Pregius Polarsens sensor (IMX250MZR/ IMX253MZR/IMX264MYR) polarization sensitive camera. The IMX250MZR sensor was used in our experiment assembly.

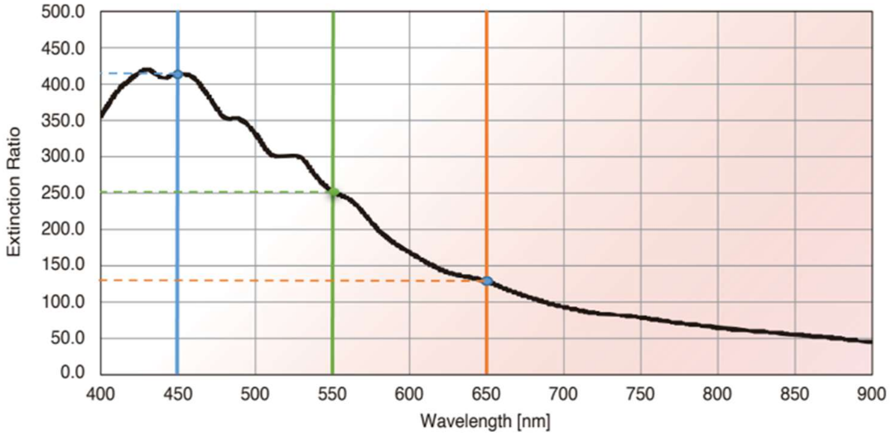

Figure 4.6. Extinction ratio versus wavelength of the 2/3 inch Sony CMOS Pregius Polarsens sensors. (https://www.sony-semicon.com/en/products/is/industry/polarization.html)

In our experiment setup, the minimum and maximum wavelengths of light are 450nm (Blue) and 650nm (Red).

From the graph above, 450 nm corresponds to ~ 415 ER ~ 2.41x10^{-3} extinction and

650 nm corresponds to ~ 130 ER ~ 7.7x10^{-3} extinction.

According to the above extinction ranges, an extinction better than 10^{-2} can be detected from the polarization sensitive camera, IMX250MZR sensor, which is within the detectable range.

During their calibration work of the polarization image IMX250MZR sensor, Connor Lane et. al. found that the polarization measurements of the camera with blue-green light are generally more precise than with the red light, as the extinction ratio of the sensor is about three times higher for these shorter wavelengths, blue and green light [60]. The accuracy and stability of the collected polarization data are direct consequences of the camera sensor's extinction ratio. The lower the extinction ratio and the inconsistency of the polarizer, the less becomes the accuracy of the measurement [65]. The extinction ratio of polarization image sensor is the ratio of the sensitivity of transmission axis light to the sensitivity of extinction axis light. A shorter distance between the polarizer and the photodiode improves the extinction ratio and the incident angle dependence.
[https://www.sony-semicon.com/files/62/flyer_industry/IMX250_264_253MZR_MYR_Flyer_en.pdf]

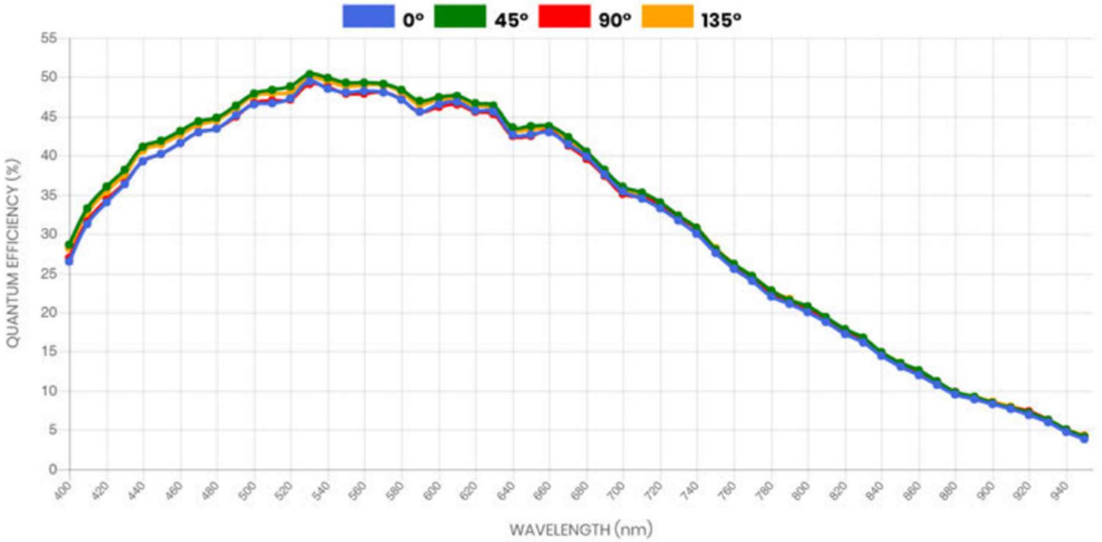

Figure 4.7. Quantum efficiency versus wavelength of the unit cell of the IMX250MYR camera sensor

https://d1d1c1tnh6i0t6.cloudfront.net/wp-content/uploads/2018/11/Going-Polarized-Presentation.pdf

The polarization sensitive camera sensor (The Imaging Source Company's DYK 33UX250 USB 3.0 Polarsens camera, color polarization image sensor IMX250MYR equipped with four on-chip four-azimuth polarizers), serves the polarization state data, from 0, 45, 90, 135-degree rotation positions and a three-color (RGB) Bayer arrangement micro color filter in each position. IMX250MYR sensor is equipped with 2,448 × 2,048 PDs in total, which form 612 × 512 blocks ,as every single block is a matrix of a 16,(4×4), Photodiodes (PDs) [57].

G-colored filter can be detected in two regions (G1 and G2) in the same block, which have almost similar spectral characteristics. This suggests that the rank of the spectral crosstalk matrix is only three because it is practically a three-color sensor. Furthermore, although the micro polarizer has four azimuths, the rank of the polarization crosstalk matrix is only three, as per Malus's law. Therefore, because the total ranks of the crosstalk matrix is maximum nine (3 [polarization] × 3 [color]), the maximum number of bands that can be imaged with this color polarization image sensor is nine [57].

Using the color polarization image sensor IMX250MYR, the observation image with 16 channels was obtained with the combination of four polarization azimuths and four colors (R, G1, G2, and B; practically three colors) [57].

This arrangement is equal to a conventional static photometric rotating analyzer ellipsometer.

The sample is illuminated by a non-collimated light through a fixed polarizer at an azimuth of 45 degrees to the plane of incidence. The reflected light passes through a virtual "rotating analyzer" and the intensity is captured by a two-dimensional position sensitive photodetector system at four different angular positions of the analyzer.

Minimum 3 different analyzer positions are required. These four polarization states (intensity) data (at 0, 45, 90, 135-degree rotation positions) are enough (the fourth data is good to reduce the error) to determine the ellipsometric angles: ψ and Δ. Our camera serves the data for 3 colors, so we have 3x2 measured ψ and Δ.
As part of our large area optical mapping tool configuration, there is a fixed 0.2mm diameter pinhole in front of the polarization sensitive camera as shown in figure 3.3 in the experiment setup.

The chosen pinhole diameter of 0.2 mm was not selected arbitrarily; it was determined through a balance-of-constraints analysis between two competing requirements: lateral resolution and detected optical intensity,based on a fundamental trade-off in optical systems.

In imaging ellipsometry, reducing the pinhole diameter improves lateral resolution because it limits the cone of rays reaching the detector, but this simultaneously reduces the detected intensity, which increases noise and lengthens the required acquisition time. Increasing the pinhole size has the opposite effect: stronger signal but degraded spatial resolution due to increased angular spread, and the angular cone small enough not to noticeably degrade lateral resolution or angle-of-incidence fidelity.

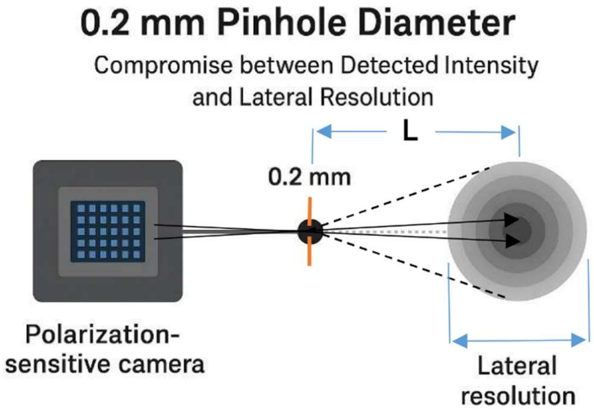

Figure 4.8. Scheme illustrating the geometric spatial resolution of a pinhole camera

The optimal pinhole size (D_{optm}) is the diameter that minimizes the **total spot size** (or blur radius) of the light beam on the sensor plane.

A). Lateral resolution

Resolution in a pinhole system is limited by the larger of two spot sizes: geometric blur and diffraction blur.

i). Geometric Blur (R_{geom}) Rays from a single object point hitting the sensor are spread over a circle whose size is proportional to the pinhole diameter (D).

$$R_{geom} \propto D \qquad (19)$$

ii). Diffraction Blur (R_{diff}): Light waves passing through the small aperture spread out (Airy disk effect), proportional to the wavelength (λ) and inversely proportional to the pinhole diameter (D).

$$R_{diff} \propto 1/D \qquad (20)$$

The total blur is the combination of these two effects. The minimum total blur, and thus the maximum resolution, occurs where the geometric blur size is approximately equal to the diffraction blur size.

$$D_{optm} \approx \mathrm{sqrt}(4\lambda L) \qquad (21)$$

Where,

L is the effective optical path length, the distance from the pinhole to the sensor/detector plane, and

λ is wavelength of the light.

Note that, the 0.2 mm choice more or less satisfies the result of applying equation 3, in association of the specific optical path length (L), roughly between 1.5cm and 2cm and considering the central wavelength (λ) of the light source.

B). Detected Optical Intensity

The signal strength hitting the detector is determined by the amount of light that passes through the aperture.

$$\text{Detected Intensity } (I_{det}) \propto \text{Area (or } D^2), \quad I_{det} \propto D^2 \tag{22}$$

A larger pinhole always yields a higher intensity, leading to a better **Signal-to-Noise Ratio (SNR)**. This is crucial for polarization measurements where the signal is split and often weak, particularly during extinction measurements.

According to the equation 22, a 0.1mm pinhole diameter would provide four times less light intensity and consequently needs longer time to reduce the noise but counterintuitively would likely result in relatively worse overall resolution, because the image blur would be dominated by diffraction, leading to much noisier, less sharp data.
The 0.2 mm pinhole is an appropriate pinhole diameter we used that meets our target lateral resolution (i.e., before the geometric blur dominates), thereby maximizing the collected light and SNR of our specific system. It is an appropriate compromise between the two opposing blur effects while maximizing the necessary optical signal.

The monitor LCD-LED monitor used in this assembly, Figure 4.4, has an LED backlight source and an LCD screen monitor, which produces a linearly polarized light, a core requirement of the spectroscopic ellipsometry technique for the measurement of the change in polarization state of the measurement beam.

It is noting worthy that not all commercially available monitors are useful for this technique. For example, the standard OLED (organic light emitting devices) monitors cannot be directly used as they inherently produce unpolarized light, or very weak polarized light, if any.

QLEDs (Quantum Dot LEDs) do not inherently produce a linearly polarized light, the output of the QLED display is a linearly polarized as the LCD architecture always includes a front polarizer, after passing through the LCD structure that modulates the quantum-dot backlight.

There are some ongoing research works that focus on specially designed OLEDs, like LP-OLED (Linearly polarized OLEDs), to directly emit a linearly polarized light intrinsically, eliminating external polarizers, for various applications. One research demonstrates incorporating a bi-functional meta-electrode constructed with an elliptical Nano-pillar array. This meta-electrode simultaneously controls polarization and improves light extraction, achieving a tunable polarization extinction ratio [63] and other similar research demonstrated that highly polarized emission could be realized by utilizing materials with well-defined molecular alignment and constructing a micro-cavity structure to amplify the polarized light [64]. There are also other ongoing research on pol-less OLEDs (polarizer free OLEDs) too.

Research Materials

Silicon dioxide is one of the most studied materials and widely used in the semiconductor industry, due to its huge abundance, affordability, and technological importance[24]. It has many applications in microelectronics components like gate oxides, dynamic random access memories, etc. While studying the inhomogeneity of SiO_2 thin films and photoresist layers by spectroscopic ellipsometry, Rosu et. al. proved the homogeneity of the SiO_2 film to be a maximum of 1% across the sample, qualifying it as a patterned large-area reference sample for film thickness [24]. This makes SiO_2 (on silicon substrate) a key material in most of our calibration methods.

Polysilicon is one of the most important materials for silicon-based electronic devices. It can be used in the production of very large scale integrated (VLSI) devices. Doped polysilicon is frequently utilized as resistors in static memory circuits, gate electrodes, and connection materials [45].

It is crucial for silicon-based electronic device fabrication and monitoring processes, with properties influenced by deposition processes and temperatures [45].A Transition from amorphous to polysilicon occurs between 550°C and 595°C, affecting crystallinity, morphology, and optical characteristics [46].

As B. Gruska conclusion notes, ellipsometry in the UV-visible and NIR spectra range is ideal for measuring polysilicon films, both directly deposited on silicon and on SiO_2 /Si, without a sample reference requirement for calibration [45].

Note that, Polysilicon films are composite materials of crystalline and amorphous silicon, with increased surface roughness correlating to greater film thickness.

4.2. Data Collection and Processing Methods

The data collection in our research work is purely experimental.

When the ellipsometer device is set, and put the relevant sample at the sample holder, and device is on and an automatic imaging ellipsometry takes place and the change in the polarization state of the measurement beam are recorded in real time with a software linked to the polarization sensitive camera installed in a computer. The polarization state intensity data (see Fig. 4.5) from each position data is then exported into a separate storage, ready for further analysis, as these data are not the direct parameters of interest. The tan (ψ) and cos (Δ) values are calculated real-time from the polarization state intensity data, as defined previously. Further data analysis is done using a homemade Matlab or Python software to reach to the final stage of the parameters of interest, optical constants, angle of incidence, and thin film thickness. MSE, mean square error, the discrepancy between the theoretical and experimental values is calculated to know the precision of the device, in comparison to our conventional ellipsometer in our laboratory, J. A Woollam M2000 DI ellipsometer.

4.3. Limitations and considerations

Despite the fast, large surface area sample analysis capability, stable and strong performance of our optical mapping tools, some limitations are worth noting for considerations.

Generally, systemic errors in may emerge from the non-ideal LCD-LED monitor polarization, ± 0.1° uncertainty of the digital angle gauge used to set the orientation of the monitor at 45^0 with respect to the horizontal plane of the sample. Sony IMX250MYR Polarsens sensor may also pose a minor error in the polarization beam measurement.

The dominant source of errors in our assembly is the non-ideal LCD monitor polarization. Accordingly, the LCD-LED monitor calibration was carried out using a rho-correction method, to correct the measurement errors that may rise from the imperfect optical designs, wavelength dependent polarization light states and spatial non-uniformity of the LCD monitor. This calibration method has been discussed in detail in the next chapter.

During the LCD/LED monitor fixation in our apparatus, a digital angle gauge with a 0.1^0 angle uncertainty was used. This contributes to minor systematic errors in our experimental measurements.

I have demonstrated this effect using a specifically written Matlab code simulation. I considered an Air / SiO_2 / Si optical model, which is often called the ellipsometry calibration standard sample, using three wavelengths of light, Red (450nm), (Green) 550nm and Red (650 nm).

The simulation code quantifies the effect of the angle of incidence (AoI) uncertainty (±0.1°) on amplitude ratio (Ψ), phase difference (Δ) and fitted thickness.

I have also deduced the standard deviation (std) and Mean thickness parameters.

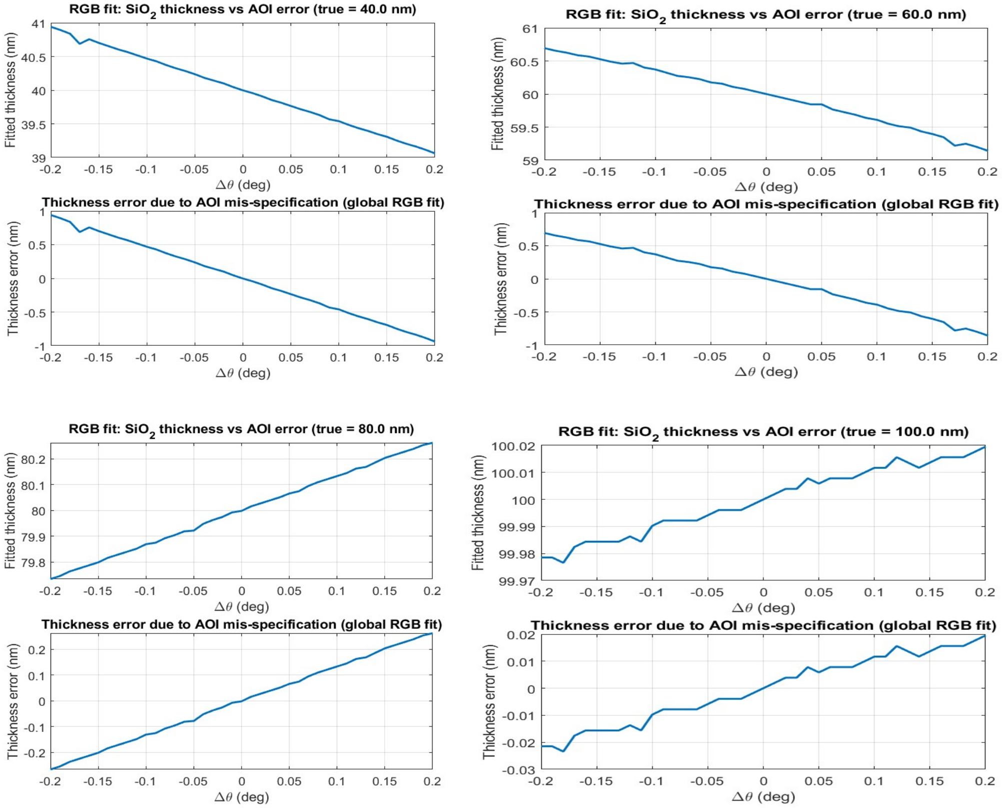

Figure 4.9. The simulation of fitted thickness and thickness error maps of 40, 60, 80 and 100nm thick SiO_2/Si samples.

As a demonstration, the simulation result of a nominal 60nm thick SiO_2 on Si wafer, the perturbed data (angle gauge $\pm 0.1^0$) data is given below.

```
Ψ, Δ sensitivity to AoI (RGB) at θ0 = 70.00°, d = 60.0 nm
            λ=450 nm: Ψθ = 42.4029°, Δθ = 87.0356° | dΨ/dθ =-0.0061, dΔ/dθ =-3.7121
                  +0.1°: ΔΨ = -0.001°, ΔΔ = -0.372° | -0.1°: ΔΨ = +0.001°, ΔΔ = +0.371°
            λ=550 nm: Ψθ = 31.5433°, Δθ = 85.4961° | dΨ/dθ = 0.0723, dΔ/dθ =-3.9722
                  +0.1°: ΔΨ = +0.008°, ΔΔ = -0.398° | -0.1°: ΔΨ = -0.007°, ΔΔ = +0.397°
            λ=650 nm: Ψθ = 25.5498°, Δθ = 90.1145° | dΨ/dθ = 0.0136, dΔ/dθ =-4.5238
                  +0.1°: ΔΨ = +0.002°, ΔΔ = -0.453° | -0.1°: ΔΨ = -0.001°, ΔΔ = +0.452°

Fitted thickness using all three wavelengths
                         +0.1° AoI error:  d_fit = 59.621 nm (err = -0.379 nm)
                         -0.1° AoI error:  d_fit = 60.342 nm (err = +0.342 nm)

Thickness statistics due to ±0.1° AoI uncertainty
Mean thickness     = 59.982 nm
Standard deviation (std)    = 0.3604 nm
```

The figure below shows a 0.3604 nm standard deviation and a mean thickness of 59.982 nm for a nominal 60nm SiO_2/Si sample during a $\pm 0.1^0$ perturbation of the AoI, which show the minor effect of the uncertainty posed in our measurements. The other remaining 40, 80 and 100nm samples have similar range of values, for their respective scale.

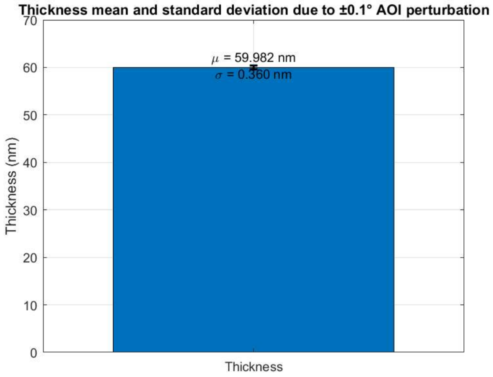

Figure 4.10. Mean thickness and standard deviation of a nominal 60nm SiO_2/Si sample simulation during a $\pm 0.1^0$ perturbation of the AoI.

As the rotation angle of the LCD-LED monitor light source significantly influences the incident polarization state of the light, the major reasons behind the 45^0 monitor`s orientation with respect to the plane of the sample, as discussed below.

Spectroscopic ellipsometry requires an oblique angle of incidence [2], as no useful information can be collected at normal incidence or parallel angle of incidence.

a) During normal incidence, AoI, $\Theta=0^0$.

In this case, the electric field components, r_p and r_s, counter the same boundary conditions. From the Fresnel equations,

Cos θ_j= Cos θ_k =1, which yields to $r_p = r_s$, $\Delta=0$ and tan (ψ) =1

As a result, the detector (the polarization-sensitive camera in our case) will record a zero phase difference, despite a constant ψ and Δ values, meaning no polarization change. Remember that Spectroscopic ellipsometry measures the change in the polarization state of the measurement beam.

b) Similarly, at parallel incidence, AoI, $\theta=90^0$,
The measurement beam travels along the sample surface, and roughly, a constant phase difference occurs. Ideally, no reflected beam can reach the ellipsometric detector, resulting in no valid measurements can be done either.

c) At Brewster angle, we get maximum phase difference leading to maximum sensitivity and optimal measurement [2].

Regarding systematic errors that may arise from the camera sensor, Connor Lane et. al. in their, calibration of a polarization image sensor and investigation of influencing factors work showed that higher omnidirectional extinction ratio of the IMX250MZR sensor for wavelengths in the blue- green range compared to the longer wavelengths of red light, graphically shown in figure 4.9 After an appropriate calibration of a polarization image sensor using the super-pixel calibration method, Connor Lane et. al. research work confirm that the Measurement errors that may arise from these sensors is very low [60].

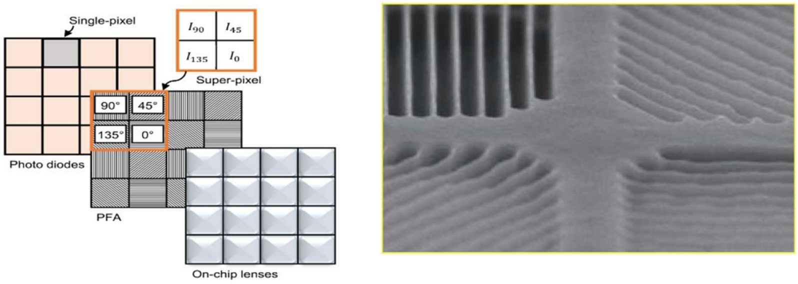

Figure 4.11. Structure of the Sony polarization image sensor and the polarizer image.

From the measurement beam of light perspective, our optical mapping tools use multi-color (RGB) light sources. To be specific;

- In our macro imaging ellipsometer, an LCD/LED monitor emits out a Red (650nm), Green (550nm) and Blue (450nm) polarized color band light sources and
- In the microscopic ellipsometer, RGB Laser module emits out a Red (638nm), Green (520nm) and Blue (450nm) as a point-like light from laser diodes.

The above list clearly shows our newly optical mapping tools use multi-color wavelengths. A broader spectral range, usually from UV-NIR, would further enhance the sensitivity of the light detector, optimize the goodness of fit in our data analysis and it would have a broader materials spectrum to be investigated, which would avoid spectral range limitation.

Below are some common points to be considered for a better flexibility and enhancements.

For a maximum sensitivity, a broader spectral range source of light would elevate the goodness of the imaging tools.

To enhance the frame acquisition of the imaging ellipsometers, incorporating polarization state modulators, like photo elastic or ferroelectric, would be suggested. Similarly, adding real time environmental control modules would open a new door for an in-situ growth monitoring.

Developing a benchmark ellipsometric parameters datasets from these tools would also help for comparison and reproducibility for future researchers in this field.

5. Experimental Results and Discussion

As a general preview, this chapter begins with the basic ellipsometric measurement, after the post-experimental setup, and then an early and simple calibration method, followed by other different calibration and validation methods, and then eventually the monitor calibration method by the rho-correction procedure. The experiments span from a sample at a single-position calibration into a multi-position calibration sample, to validate the imaging speed, the large area imaging capability of the mapping tool, integrated with the stability of the tool`s hardware, with no moving parts. Additionally, the research work evaluates and validates the macro and micro imaging capability of the optical mapping tool.

As an academic norm, to understand the strengths and limitations of our research work, every single measurement is verified with theoretical facts and independent experimental results of the J.A. Woollam M2000 DI ellipsometer in our laboratory.

The cumulative body the experimental results constitutes a foundation core support of the thesis statements, as discussed in detail in the subsequent sections.

5.1. Large area (Macro) Imaging

In principle, as the angle of incidence varies along the surface, a point-by-point angle of incidence calibration is needed using the well-known silicon dioxide/silicon (SiO_2/Si) sample. Each pixel gets a calibrated angle value. The procedure is similar to a conventional ellipsometry measurement. Standard ellipsometric databases are used to gather the fundamental optical characteristics, such as the extinction coefficients and refractive indices.

The key variables to be computed include the angle of incidence (AoI), SiO_2 layer thickness and the MSE values to evaluate the goodness of fit between the established theoretical model and experimental ellipsometric datasets.

Besides, the experimental ellipsometric data analysis of the results need to be automated to optimize data processing time and guarantee a quicker evaluation of a sufficient number of measurement samples.

As an early start, a measurement on a SiO_2 on a Si wafer is carried out on three different thicknesses: 60nm, 80nm, and 100nm. Matlab automated measurement images of the SiO_2/Si samples are shown in Figure 5.1.

As a demonstration of preliminary results, the direct raw ellipsometric data values, tan (Ψ) and cos (Δ), maps of a 60nm SiO_2/Si substrate measurements for the RGB spectrum are shown in the figure below, before their incorporation into the Fresnel equations for data analysis. The figures show measured ellipsometric angles, tan (Ψ) and cos (Δ) values, for each color bands, blue (450nm), green (550nm) and red (650nm) which are similar, but not the same as ellipsometric angles depend on the wavelength of the measurement beam. A clear part of a circular figure gradient can be observed from the figures, which is the actual shape of the SiO_2/Si sample. The spikes show areas where there is no sample, outside the circular edge of the sample. The photograph of the 60nm SiO_2/Si sample handling procedures and positions is shown in figure 5.4.

The corresponding ellipsometric raw data maps for 80nm and 100nm SiO_2/Si samples can be found in the appendix.

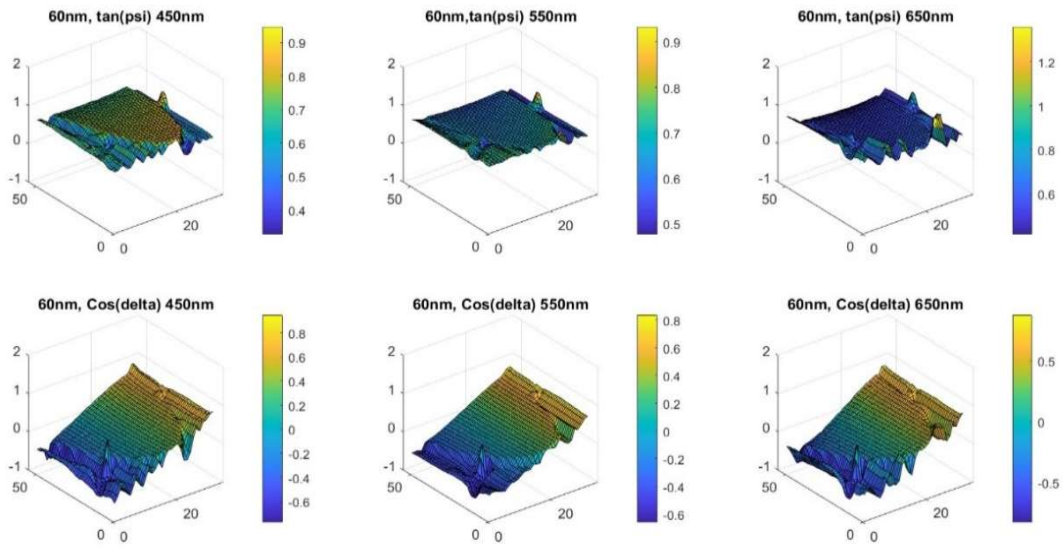

Figure 5. 1. hjhj

Figure 14. A 60nm SiO_2/Si substrate tan (Ψ) and cos (Δ) data values from the RGB light source.

The image below shows the computed angle of incidence calculated from the three samples, using the automated homemade Matlab code.

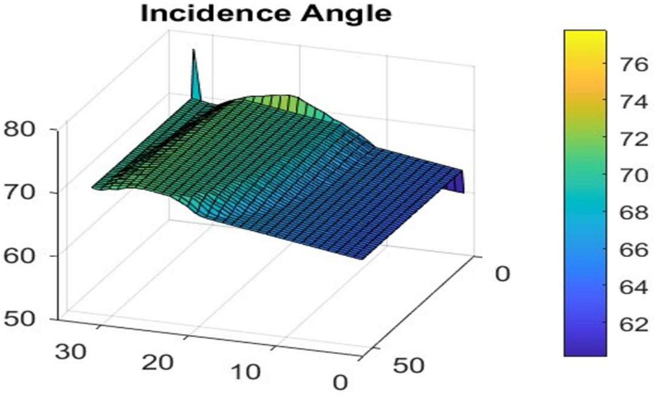

Figure 15. The common angle of incidence for the 60, 80 and 100nm thick SiO_2/Si samples

Note that, the angle of incidence is the angle between the incident beam and the surface normal to the sample. It depends on the instrument optics, or the geometry of the experimental setup. In contrast, the choice of the angle of incidence strongly affects the ellipsometric angles (Ψ and Δ). Therefore, for a stable experimental setup, every corresponding specific data points of a sample, even for different samples of different thicknesses, have the same corresponding angle of incidence. Nevertheless, there exist variation in the incidence angle against the spatial variation over a specific sample surface.

As described in the previous chapters, SiO_2/Si sample is a well characterized, stable and reproducible material, always used as a standard reference material in the field of ellipsometry for calibration. Hence, a nominal 60nm SiO_2 on a 20cm silicon wafer is chosen for our first calibration of the optical mapping tool from inexpensive parts. The experimental encompassed three distinct steps: Angle of Incidence (AoI) calibration, a SiO_2 sample thickness determination, and subsequent Mean Squared Error (MSE) analysis.

In figure 5.3, the computed SiO_2/Si thickness from the J.A. Woollam M2000DI ellipsometer (completeEase software) and from our large area (macro) imaging tool from inexpensive parts, a uniform variation gradient of the angle of incidence and the associated MSE value maps are shown. The mean square error (MSE), the of goodness-of-fit, observed is relatively low.

Note that, the primary region of interest is the center area of the sample, as areas outside the edge of the sample show relatively higher MSE values. The center area of the sample in Figure 5.3 b) indicates a sample thickness of about 60-61 nm thickness, which is close to the nominal 60nm thickness. Moreover, the measurement from our large-area optical mapping tool from inexpensive parts exhibits a good concordance with the conventional J.A. Woollam M2000DI ellipsometer, with an approximately 2 nm thickness discrepancy.

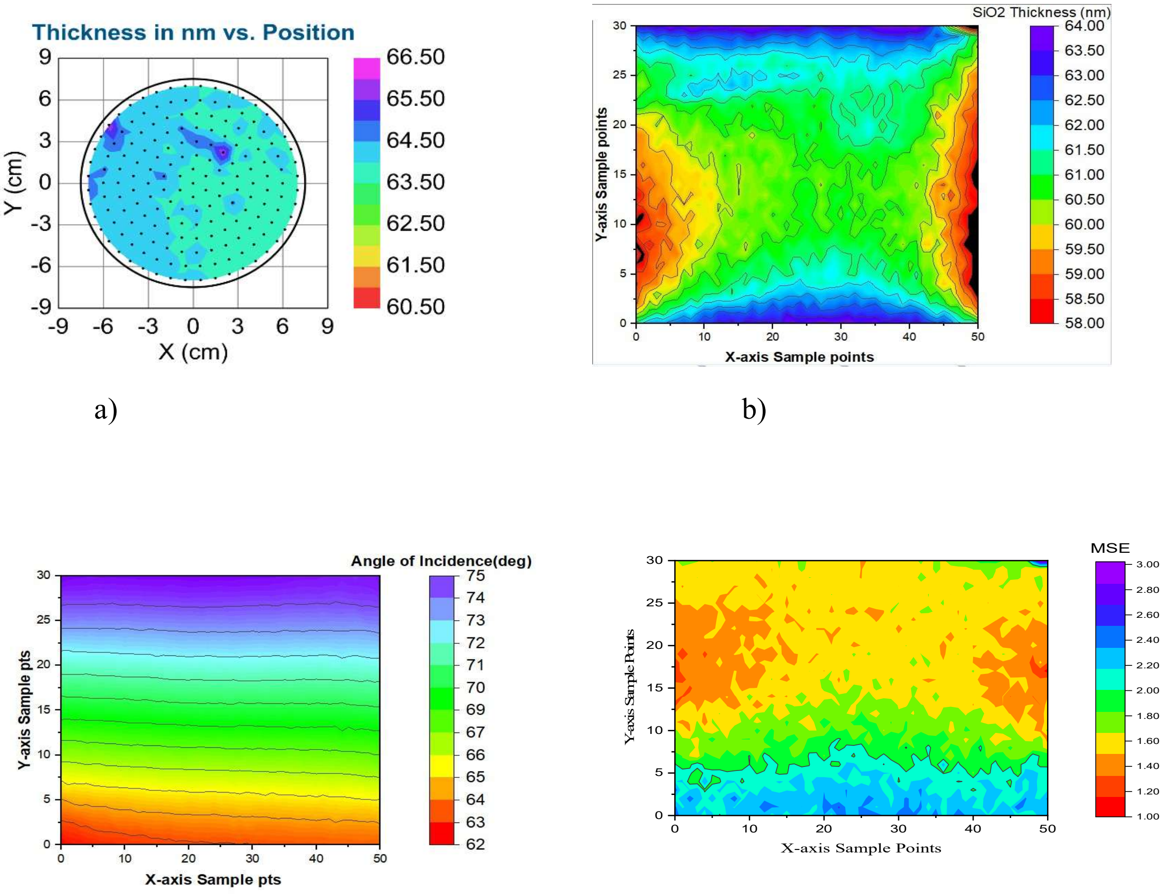

a) b)

c) d)

Figure 16. A nominal 60nm Silicon dioxide sample on a 200mm silicon wafer, (SiO_2/Si) maps

a) SiO_2 thickness ,from the J.A. Woollam M2000DI ellipsometer (completeEase software)

b) SiO_2 thickness , from our newly developed imaging tool

c) the angle of incidence and d) the associated MSE values

The total acquisition time of the above imaging experiment does not take more than 4 seconds, which is a very short period, especially when compared to the conventional ellipsometers, which typically would take more than 20 minutes.

To validate the spatial performance of the newly developed imaging ellipsometric mapping tool, comparative experiments were conducted on nominal 60 nm SiO_2/Si sample at three distinct surface positions left, center and right respectively, as shown below.

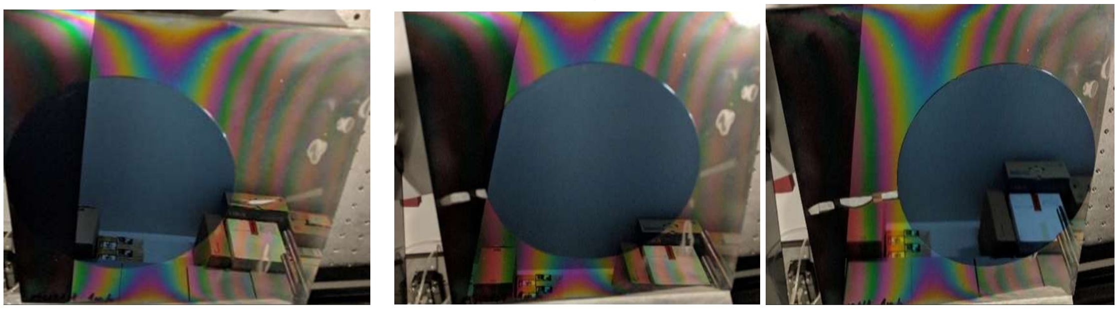

Figure 17. Photograph of the nominal 60nm thick SiO_2 on a silicon wafer in three distinct positions, left, center and right respectively.

To do this measurement, the first step is to measure and evaluate the actual angle of incidence calibration for each coordinate, using the standard SiO_2/Si sample. This was done by placing the oxide sample at three different positions. The thickness results of this calibration are shown in Figure 5.5.

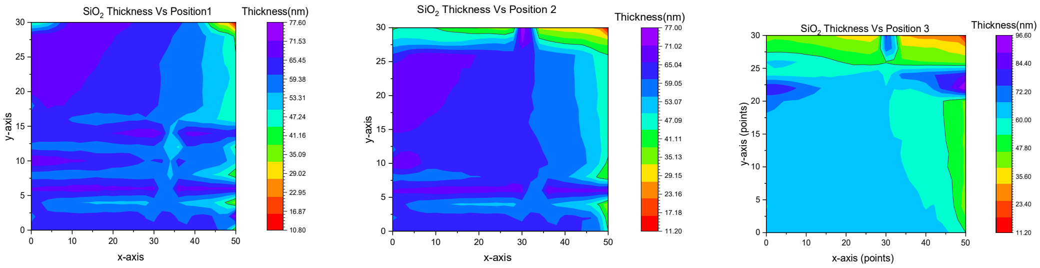

Figure 18. Thickness maps of the nominal 60nm SiO_2 on a silicon wafer in three distinct positions, position 1, 2 and 3 respectively.

Note that, the results of the measurement of the calibration from our prototype tool shows points of high MSE values and less MSE values for specific regions within each position, as expected, due to overlapping layers.

Note that, the M2000 ellipsometer can map only 15 cm diameter area in one cycle, where as our optical imaging tool assembly maps bigger area than the actual size of the measured Si-wafer, which made measurements in different positions, three in this case, feasible.

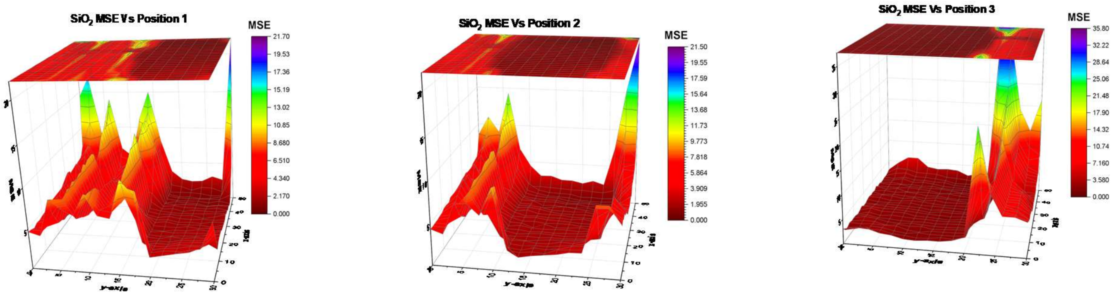

Figure 19. 3D maps of the MSE values for the SiO2 in three distinct positions position 1 , 2 and 3 respectively.

From the above figure, it is evident that, regions within the SiO_2 sample show less MSE and regions outside the edge of the sample show higher MSE values on each positions.

Given that lower Mean Squared Error (MSE) values denote better measurement precision, a good calibration was achieved by selectively extracting the minimum MSE value at each corresponding positional coordinate from the three distinct positions, thereby synthesizing a new, equivalent single MSE map as shown in the Figure 5.7. (a).

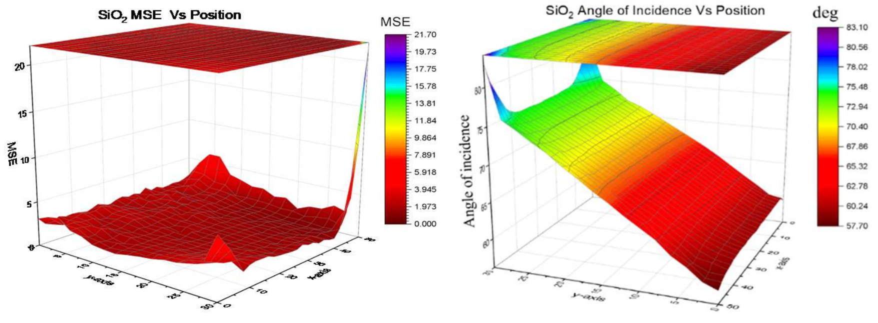

a) **b)**

Figure 20. a). MSE calibration map and b). Angle of incidence calibration map for 20cm diameter, nominal 60nm thick SiO_2.

These lowest MSE values in Figure 5.7 (a) are in turn used to calculate the corresponding angle of incidence calibration, Figure 5.7. (b).

The pinhole camera couples the sample points directly to the sensor matrix pixels one-by-one. This detection system is almost without a background. The measured area is determined by the size of the monitor and the sensor-pinhole, pinhole-sample and sample monitor distance-ratios. The lateral resolution is also determined by the distance ratios and the pinhole diameter. The pinhole diameter (presently 0.2 mm) is a compromise between the detected intensity (measuring time, presently 1-4 seconds) and the lateral resolution. One can see the illustration of the resolution (presently better than 5 mm) in Figure 5.8, where a chessboard-like etched silicon dioxide-covered silicon wafer “delta-contrast” picture. The bright parts are the original (nominally 100 nm thick) oxide layer, the dark squares are the 4x4 mm sized etched native oxide covered silicon surface. In the figure below, the MSE map shows where the sample is (low MSE, blue part) and the squares in the thickness-map.

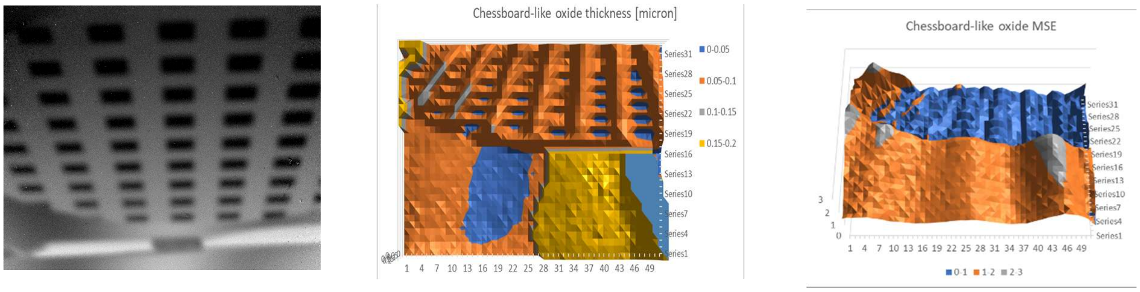

Figure 21. Illustration of the resolution of the experimental setup

Silicon dioxide-covered silicon wafer “delta-contrast” picture (left), Chessboard-like Oxide thickness map (center) and the corresponding MSE map (right).

Next, poly-Si-on-SiO$_2$ samples were measured. The films were deposited onto 6-inch (15.24cm) silicon wafer. We used the calibrated angle-of-incidence values to determine the thicknesses. Fig. 5.9 and 5.10 show the results. The regions of the low MSE values show location of the samples and the regions with relatively higher MSE values are areas outside of the sample. We must note that the perspective shortening makes worse the upper part. We show the thickness map of the “lower” part in Fig. 5.10. We compare the results with the M2000 results, too.

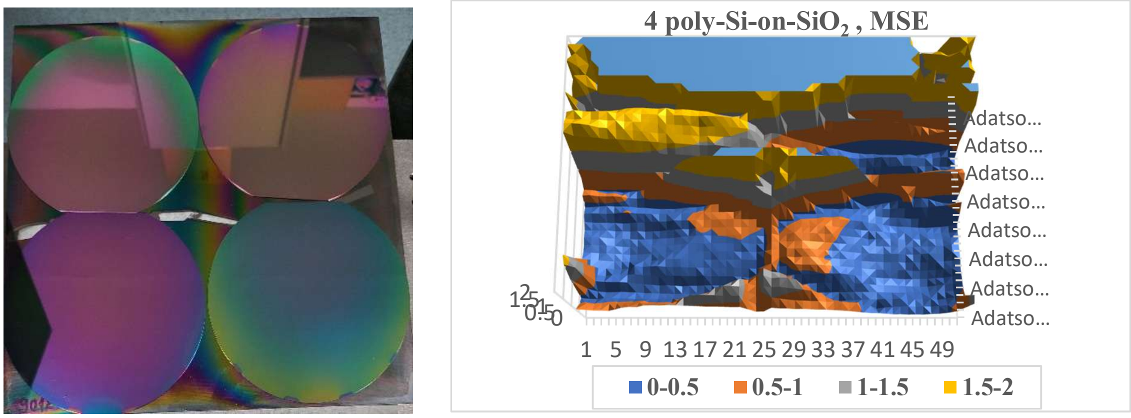

Figure 22. Photograph of poly-Si-on-SiO$_2$ samples on 6-inches (15.24 cm) Si-wafers (left) and their corresponding MSE map (right).

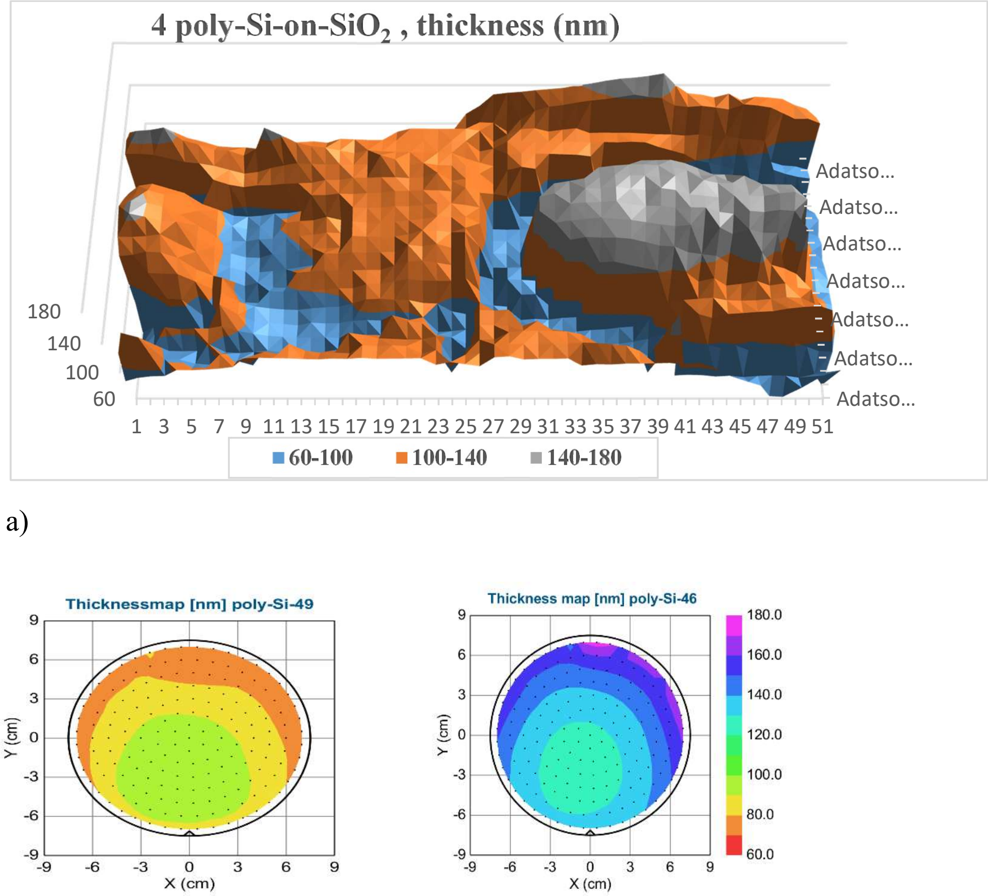

a)

b)

Figure 23. Thickness maps of Poly-Si samples on SiO$_2$/Si.

a) 4 poly-Si on SiO$_2$/Si thickness map measured by our large-area mapping tool ellipsometer
b) Poly-Si-49 (left) and Poly-Si-46 (right) thickness maps on SiO$_2$/Si measured by J.A. Woollam M2000 DI ellipsometer.

5.1.1. Monitor calibration using rho correction method

In the previous Chapter, we experienced some systematic difference in the thickness maps between our mapping tool and the M2000DI measurements .Checking a device or setup for accuracy and precision, as well as attempting to fix any flaws or malfunctions through calibration and validating it with other equivalent standard models, is a typical scientific technique. In spectroscopic ellipsometry, an appropriate treatment of instrument imperfections minimizes measurement errors [1].

To optimize the sensitivity and precision of our macro-imaging tool, the LCD/LED monitor calibration and then compensating the discrepancies with necessarily correction is crucial for better results.

Theoretically, the LCD monitor should send a perfect linearly polarized RGB (Red (650nm), Green (550nm) and Blue (450nm)) light beams towards the sample. To consider this, we performed a direct control measurement as can be seen in Figure 5.12. However, each light wavelength leaves the screen with somehow imperfect polarization state mainly due to imperfect optical designs, wavelength dependent polarization light states and spatial non-uniformity. These this may give rise to systematic wavelength dependent errors, and therefore affects the ellipsometric data outputs. The main parts of a typical LCD monitor are shown in the flow chart below.

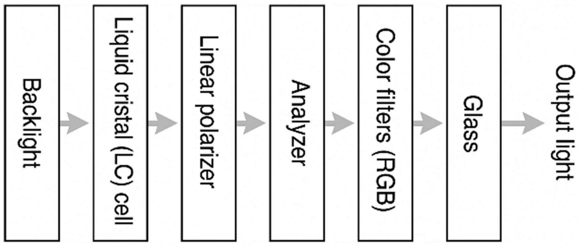

Figure 24. Main parts of a typical LCD monitor

To start our calibration process with, we direct the polarization sensitive camera to the monitor without any reflecting sample, then we measure each tan (ψ) and cos (Δ) values for each RGB lights.

Theoretically, for a perfectly linearly polarized, the values are supposed to be unity, one. Nevertheless, the images in figure 5.13 tan (ψ) and cos (Δ) values result of direct-monitor measurements clearly shows the need for a monitor calibration and implementing the ρ-monitor-correction.

The polarization state from the monitor depends on the angle formed from the relative position of the monitor and the polarization sensitive camera in the experimental setup. See the schematic diagram below.

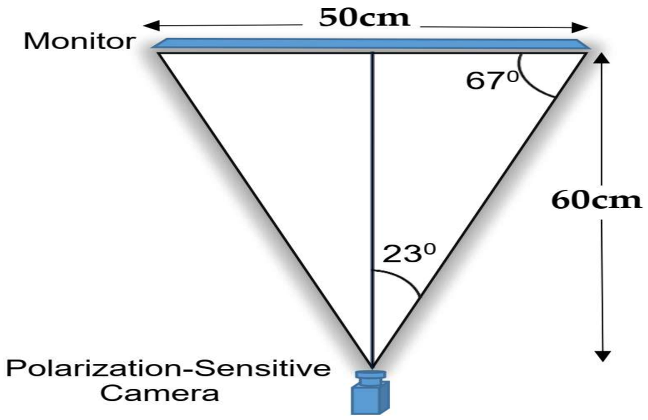

Figure 25. Angle of incidence diagram scheme from the monitor-camera view.

The systematic values deviation from one (1) in the tan (ψ) and cos (Δ) maps clearly show the fact that a point-by-point ρ (rho)-correction calibration is needed.

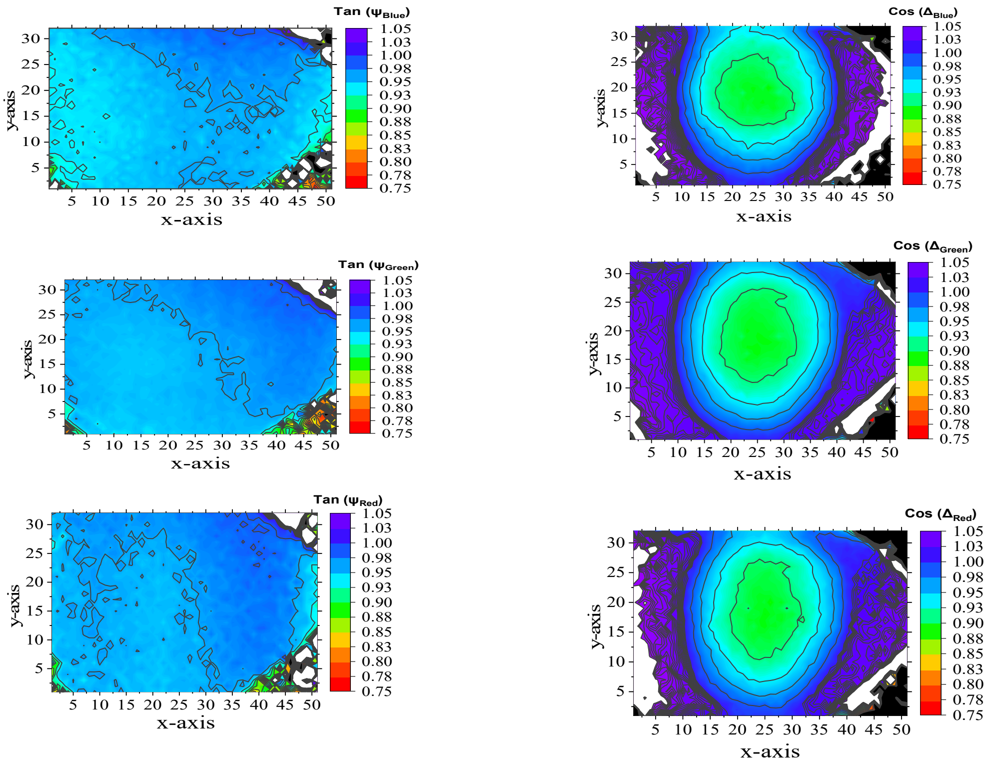

Figure 26. Experiment results of the tan (ψ), left block, and cos (Δ), right block, values for RGB color of the direct monitor measurements

In the figures above, the x and y-axes represent the pixel group in the sample, 51x32 and the z-axis (color band) shows the spectrum of the tan (ψ) and cos (Δ) values in each corresponding category, depending on the type of the map.

Three SiO_2 sample with different thicknesses (nominally 40 nm, 60 nm and 100 nm) on Silicon substrates were used for the calibration process:

The equation below is used to during our Monitor-correction experiment:

$$\rho_{opt} = \rho_{meas} * \rho_{\mathrm{monitor}} \tag{23}$$

(It is different for each point and each wavelength)

Where,

ρ_{opt} is the measured value with perfect light source

ρ_{meas} is the actually measured value and

ρ_{monitor} is the ρ-correction.

We measured three SiO_2/Si samples with different thicknesses. We determine 3*N*2 ψ and Δ (where N is the number of different wavelengths, presently 3) and we should calculate (fit) 2*N+3+1 unknown calibration values for a full calibration: N*real (ρmonitor) and N*im(ρ_{monitor}) + 3 thicknesses + 1 actual angle of incidence in each points and each wavelengths. Each thickness and angle-of-incidence in the sample depends only on location, but the ρ-corrections (ρ_{monitor}) are location and wavelength dependents. This implies ρ-corrections give more insight on the nature and status of the sample measurement.

In our calibration process, we fit the angle-of-incidence (wavelength independent), the three thicknesses (wavelength independent), and the ρ_{monitor} (location and wavelength dependent) point-by-point for each pixel throughout the sample.

A special software or program is required to perform this complicated calibration process, because we should fit the results in a complicated manner, fitting all the 10 unknown parameters in the same time using the measurements of the 3 different oxides. A Matlab program with some other complementary software was used in our case to analyze and interpret the experimental values.

a) b)

Figure 27. Position order of a SiO2 sample, on six different positions at different places.

(a) Sample position order model (b) Sample at 3rd position

Each 20 cm diameter oxide samples were placed at six different positions on the 30x30 cm holder, see Figure 5.14. After the fitting procedure, we get the thickness values, the angle-of-incidence values, the $\rho_{monitor}$ values, and the MSE (mean square error, the goodness of the fit), which is the squared difference between the measured and calculated ψ and Δ values. The fitted thickness, the angle of incidence and ρ (rho) values were refined. Areas of less MSE values were selected, as they show a good fit. As each oxide sample is put at a specific position on the substrate, significant errors can be seen several places due to the edges or the insufficient illumination from the monitor.

Three SiO_2/Si samples of nominally 40, 60 and 100 nm thickness were used for the calibration process and another nominally 80 nm SiO_2/Si sample is analyzed using the calibration values from the three oxide samples. The experimental data is collected for each three oxide samples and then six different positions of each sample is used in the calibration process. The experimental figures shown in this paper are mostly deduced by excluding pixels with high MSE values that deviate the results from the true expected values, prioritizing points of only low MSE. Figure 5.15 (b) shows the MSE-map of the central 20x15 cm part where the measurement proved to be reliable.

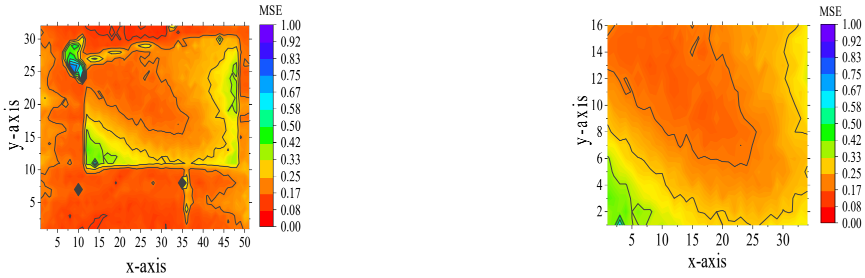

(a) (b)

Figure 28. (a). Merged MSE full map (b). Low MSE pixels map

The result of the angle-of-incidence calibration is shown in Figure 5.16. Using the same criterions (low MSE, smooth map), we refined the angle-of-incidence map (Fig. 5.16 b) from the angle-of-incidence full map (Fig. 5.16 a). We can see that the angle-of-incidence varies smoothly across the surface, which agrees with the theoretical values. This refined angle-of-incidence map is used latter to evaluate the nominally 80 nm SiO2/Si sample thickness map.

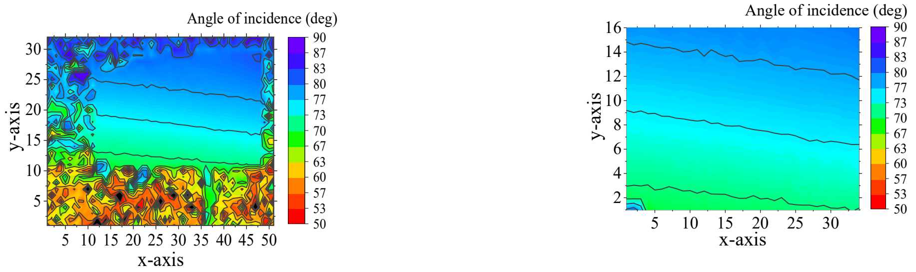

(a) b).

Figure 29. a). Angle of incidence full map b). Angle of incidence with high MSE pixels removed

The corresponding calibration process for the merged thickness maps of the oxide samples (nominally 40, 60 and 100 nm thickness) are shown below in Figure 5.17.

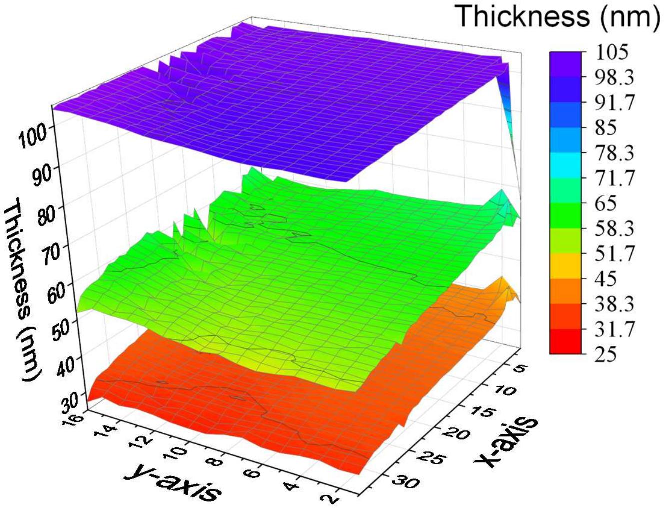

Figure 30. Thickness maps of nominally 40 nm, 60 nm and 100 nm of SiO_2/Si samples (low MSE areas) from the refined central 20 cm x15 cm part of the sample.

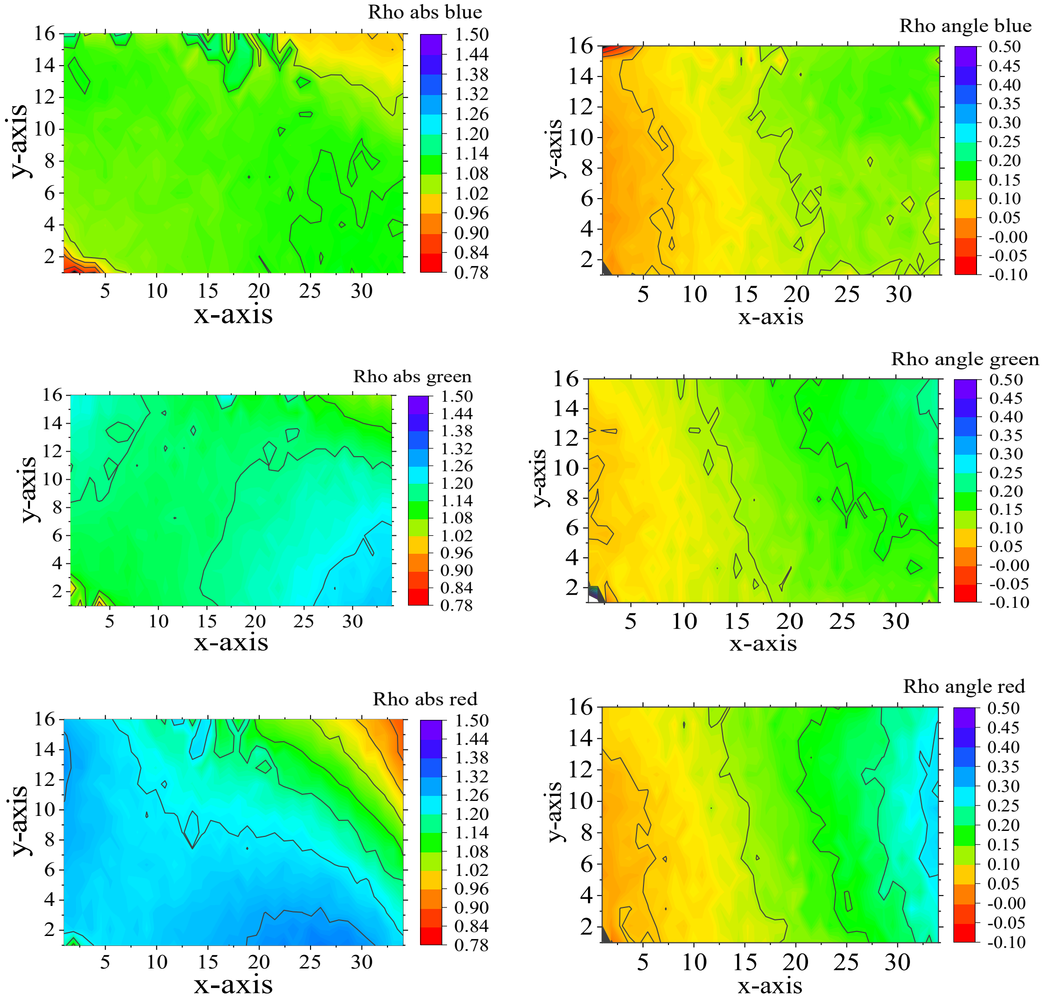

Figure 31. The calibrated $\rho_{monitor}$ values. Left column: real $\rho_{monitor}$, right column: phase shift-correction in rad. Upper row: blue (450 nm), Middle row: green (550 nm), Lower row: red (650 nm).

The calibrated $\rho_{monitor}$ values for the specific setting of the device are also mapped, see Figure 5.18. These values differ only by less than 0.3 from the ideal values, so we can use them to evaluate independent measurements.

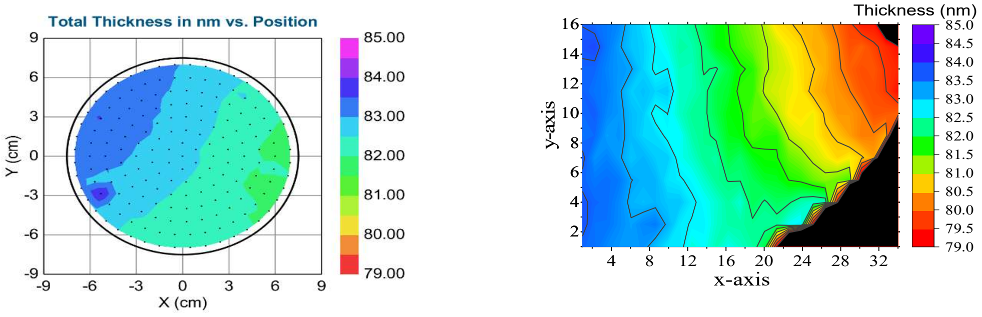

a) b)

Figure 32. a) Nominally a 80 nm oxide sample thickness map by Woollam M2000 DI SE

b) Thickness map of same SiO2/Si sample 20x15 cm area by the non-collimated, calibrated mapping tool.

Note that our M2000 DI can map only the central 14 cm diameter area of the 20 cm diameter sample.

We used a nominally 80 nm thick, 20 cm diameter SiO_2/Si sample to check the results of the calibration. We used the calibrated $\rho_{monitor}$ values to correct the measured ellipsometric angles and used the corrected values to determine the thickness map. The thickness map of the 80 nm oxide sample in Figure 5.19 (b) appears to be smooth enough. Note that, the interval between consecutive colors in the scale bar is only 0.5 nm.

An independent checking measurement of the same sample is also made by the Woollam M2000 DI ellipsometer, as shown in the Figure 5.19 (a). The agreement of the thickness measurement made between our non-collimated ellipsometer after correction, and the conventional Woollam M2000 DI ellipsometer is only within 1nm, which is a good agreement.

Overall, we developed a multi-color ellipsometric-mapping tool from inexpensive parts and applied a new calibration, rho-correction method, to make the thin film thickness measurement fast and accurate. Our new optical mapping equipment made by an ordinary color LED monitor and a polarization sensitive camera can measure big area in one second shot, while conventional ellipsometric devices needs several minutes to scan big area. After this calibration, the accuracy of our device is found to be less than 1 nm.

5.1.2. A new Bayesian evaluation method of the multi-color ellipsometric mapping on large surface area samples

Our group (Kálvin, S.; Zereay, B.N.; Juhász, G.; Major, C.; Petrik, P.; Horváth, Z.G.; Fried, M.: *A New Method of Evaluating Multi-Color Ellipsometric Mapping on Big-Area Samples*. Sci 2026, 8, 17. https://doi.org/10.3390/sci8010017) further developed the evaluation of the ellipsometric mapping measurements on the same experimental imaging device. The evaluated samples are SiO_2/Si and Polycrystalline layers deposited on Si-SiO_2 substrates using a new Bayesian evaluation method. [69]

In such a configuration, the polarization state of the illumination and the local angle of incidence vary spatially and spectrally, rendering conventional spectroscopic ellipsometry inversion methods hardly applicable. To address these limitations, a multilayer optical forward model was augmented with instrument-specific correction parameters describing the polarization state of the monitor and the angle-of-incidence map. These parameters were determined through a Bayesian calibration procedure using Si-SiO_2 wafers. Note that, we usually use the Si-SiO_2 wafers since these samples are well-established widely used references in ellipsometry. The Bayesian method was combined with simulated annealing (SA) to use as global optimization algorithm designed to deal with the global minimum or maximum of any given function [66-68].

The use of non-ideal and imperfect optical components, however, requires a departure from conventional ellipsometric evaluation strategies. Instead of relying on directly reconstructed tan ψ and cos Δ values, the present work [69] employs an intensity-based forward model and a Bayesian evaluation [70-73] framework. This approach allows the measured RGB intensity signals to be analyzed directly, while consistently accounting for instrumental correction parameters, measurement noise, and prior information on the sample structure.

In principle, the Bayesian Probability Theory (BPT) [70-73], provides a natural and consistent framework by treating all unknown quantities probabilistically and by explicitly incorporating prior physical knowledge, such as realistic parameter ranges, smoothness constraints, and independent calibration information. This method considers the limited amount of spectrum information suggests that all unknown parameters cannot be uniquely determined using the measured data alone, in addition to the fundamental challenges of multi-stage data evaluation in ellipsometry [69]

As an early calibration process, a usual norm in ellipsometry, nominally 60 nm, 80 nm, and 100 nm SiO_2 samples on silicon substrates were selected. Similar to our previous monitor calibration process using the rho correction method, in subsection 5.1.1, this framework follows similar procedures but now using the Bayesian Probability Theory, using the same validation system, the Woollam M-2000DI SE system as a reference.

Bypassing the rigorous numerical and probability equations of the BPT in [69.], the final calibration maps using the Bayesian method are shown below.

Nominal thicknesses of 60 nm, 80 nm, and 100 nm SiO_2/Si samples of 30x30 cm^2 surface area were used for an early calibration.

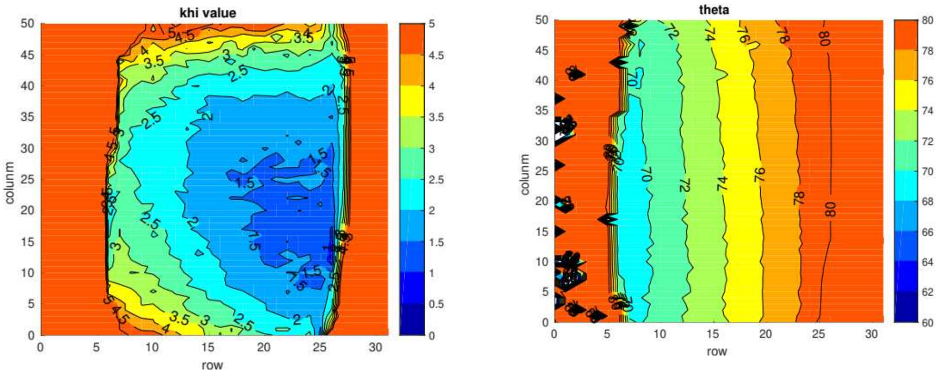

a). b).

Figure 5.20. a). Full camera field of view of χ^2 map and

b). calibrated AoI map (right) of SiO_2/Si samples.

The above figures show the χ^2 (equivalent of MSE defining for the RGB intensity signals) map and the calibrated angle of incidence surface maps, respectively. Note that the angle of incidence is common for the three thicknesses, as it depends on the relative geometry of the experimental setup mainly, the light source, sample holder and the light detector. As the measurement are taken at the full camera field of view, 30 cm by 30 cm surface area (50 by 30 pixel groups in x and y dimensions), deviations can be seen at the edge of the maps, a remainder that the central part is the area closer to the nominal values in both cases, which is to be considered later in this section.

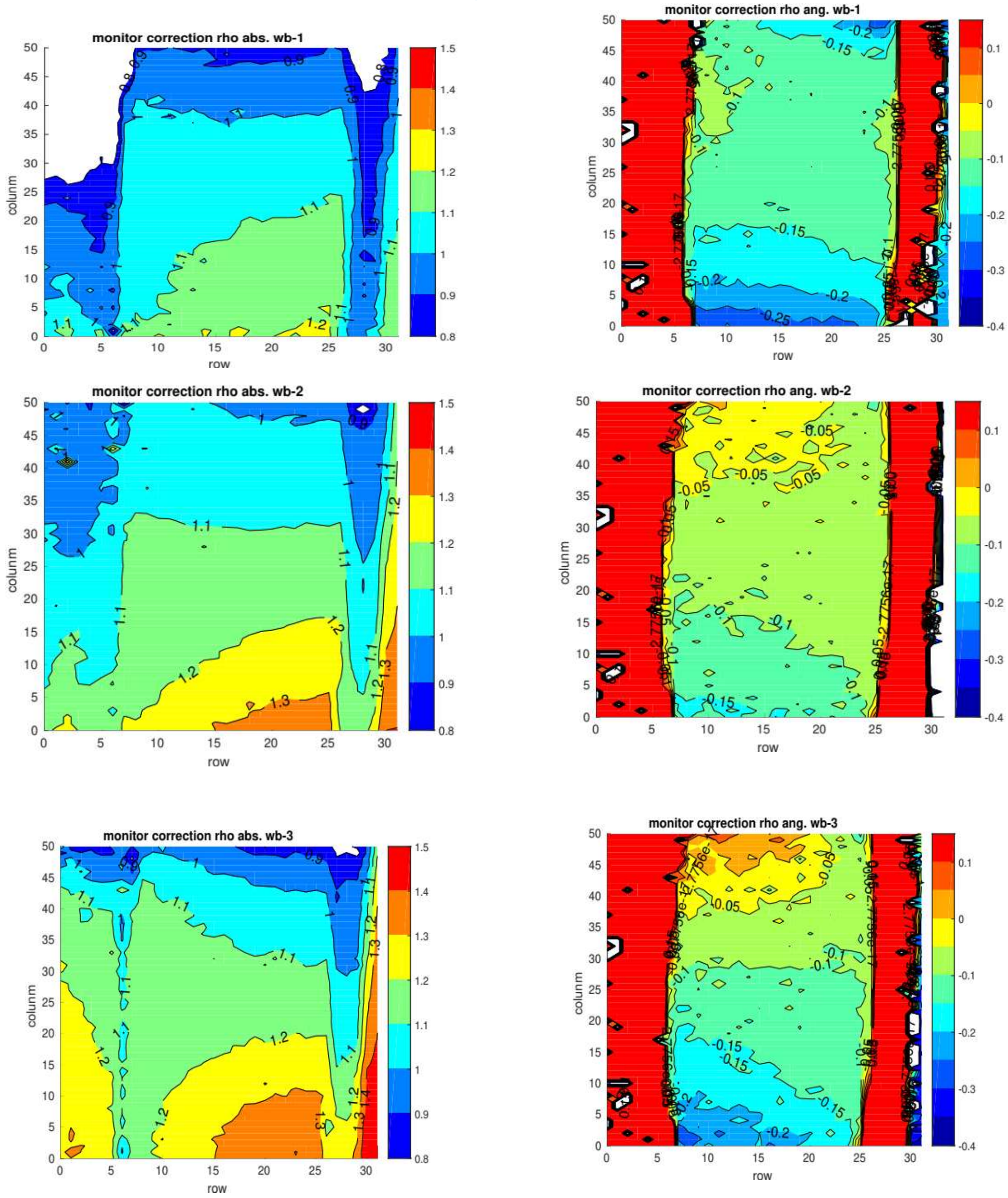

monitor correction rho abs. wb-1

monitor correction rho ang. wb-1

monitor correction rho abs. wb-2

monitor correction rho ang. wb-2

monitor correction rho abs. wb-3

monitor correction rho ang. wb-3

Figure 5.21. Maps of calibrated rho monitor values.

Left columns: absolute value of rho monitor, Right columns: phase shift-correction maps.

In the above Figures, the maps show the rho monitor-correction factor from the calibration maps part, the maps on the left column show the absolute rho values while right columns show for the rho phase shift case. From the above maps, which are recorded from the full camera field of view (50x30 pixel group points) there are more deviations at the edges from the nominal values (with absolute values close to unity and phases close to zero) and less deviations in the central part more or less at the 40 x 24 pixel group points, which is the main area of our consideration.

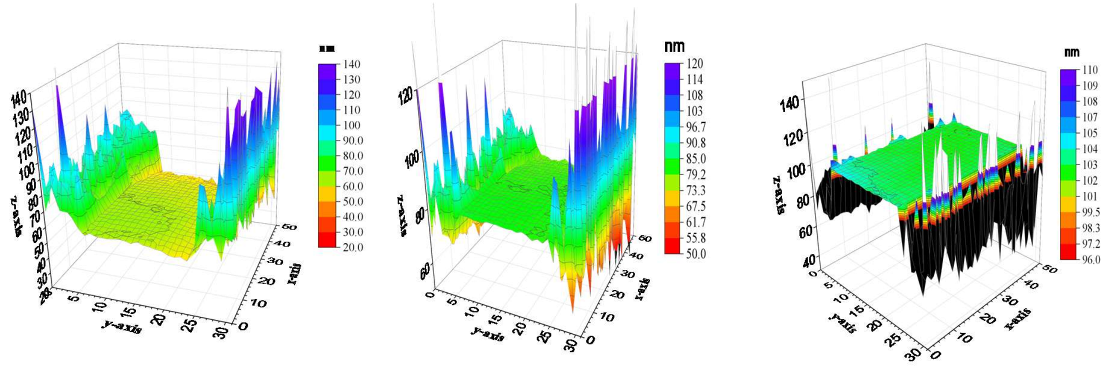

Figure 5.22. Thickness maps of SiO_2/Si samples with nominal thickness of 60 nm, 80 nm, and 100 nm, left to right, respectively.

The above figures show the thickness maps of nominal thickness of 60 nm, 80 nm, and 100 nm of the SiO_2/Si samples, from the full camera field of view, 50x30 pixel group points.

We can notice that there are some thickness spikes at the edges and the part with minimum deviation is the remaining parts, the 20x15cm surface area, which is the area selected for our calibration and hereafter referred as valid areas.

The maps shown below (Figures 5.23 and 5.24), the χ^2 , angle of incidence and the calibrated rho monitor-correction (absolute and phase shift values for the RGB channels) maps are parts of the previously shown maps, but selected in such way that the areas having less deviations and closer to their corresponding nominal values. We can see that the valid areas are (8-40) pixels groups by (8-24) pixel groups, or physically central area, 20x15 cm^2 , of the sample.

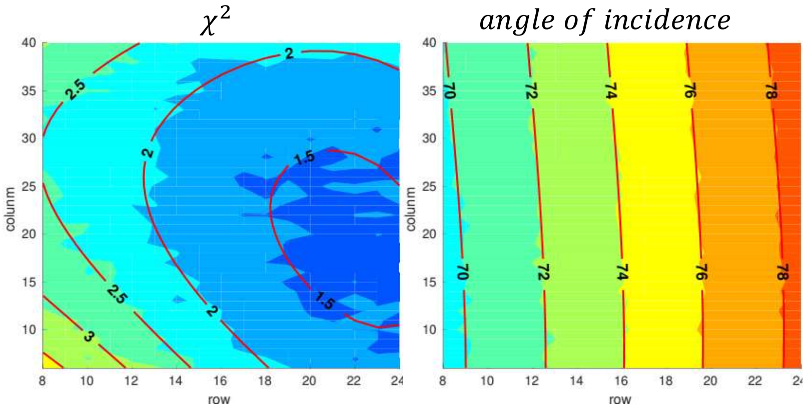

Figure 5.23.χ^2 map (left) and angle-of-incidence map (right) on the valid area, 20x15cm^2.

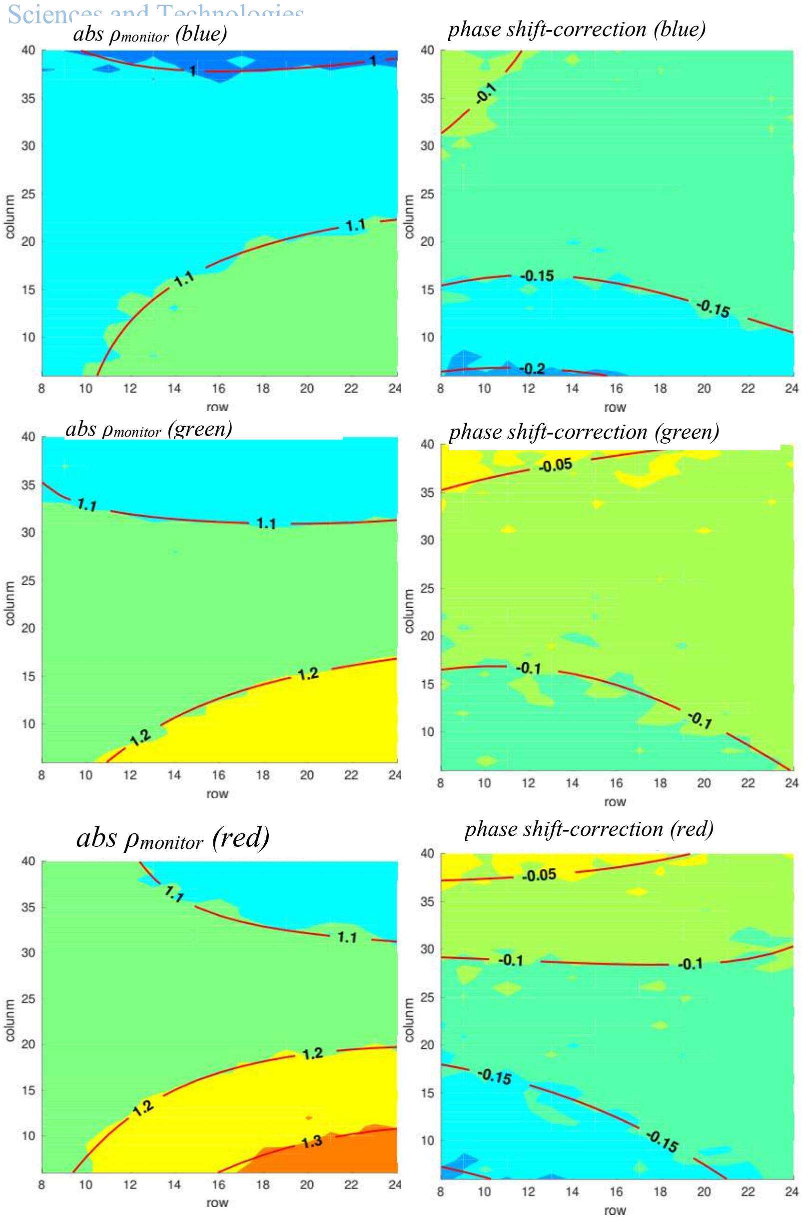

Figure 5.24. Calibrated (rho) ρ-monitor values on the central valid area, 20x15cm^2.

In the above calibrated rho correction figures, the left column maps show the absolute value of ρ-monitor correction while the right columns show the phase shift-correction maps, for each RGB color channels, Blue (450 nm),Green (550 nm) and Red (650 nm) color channels in both columns from top to bottom. The data shown is for the selected valid areas of the samples, 20x15 cm^2.

It is worth noting that the uncertainty values, arising from both systemic and statistical errors, in these data are important as the calibration values, as these uncertainties are useful parameters in the polycrystalline silicon samples analysis, which are going to be eventually discussed in this very section at later. These uncertainties were taken into account by fitting the quadratic surface into the calibrated values within the selected valid 20x15cm ^{2} surface area [69], whose cumulative results are show in Figure 5.23 and Figure 5.24.

In this procedure two SiO_2/Si wafers, nominally 20 nm and 120 nm thick SiO_2/Si oxides, Figure 5.25 and Figure 5.26 were independently analyzed in our imaging device and compared to another independent experiment done with the same samples in the Woollam M2000 DI ellipsometer in our laboratory.

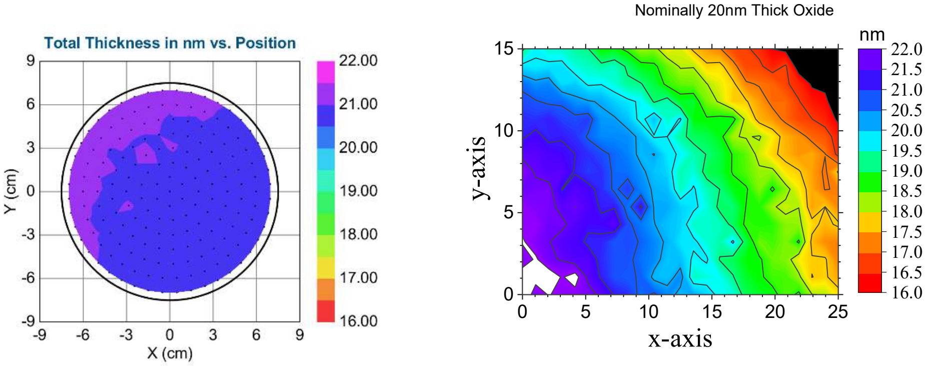

Figure 5.25.A nominally 20 nm SiO_2/Si thickness map on a 20 cm diameter Si-wafer.

Left: Woollam M2000 ellipsometer map, 14cm diameter

Right: from our inexpensive imaging device, 20cm diameter.

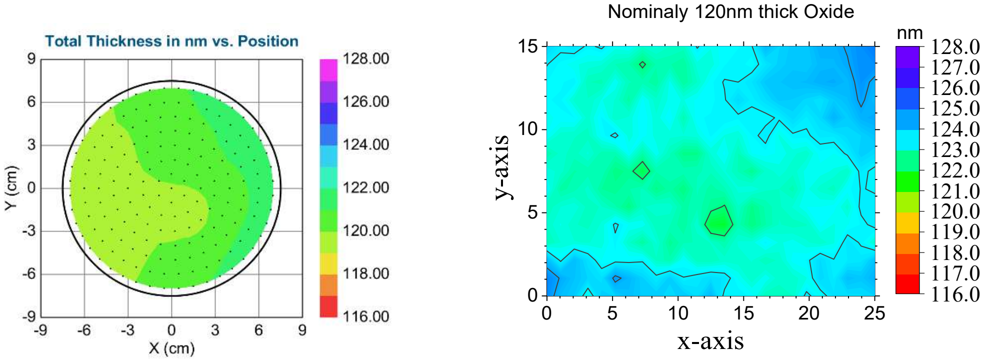

Figure 5.26. A nominally 120 nm SiO_2/Si thickness map on a 20 cm diameter Si-wafer.

Left: Woollam M2000 ellipsometer map, 14cm diameter

Right: from our inexpensive imaging device, 20cm diameter.

Note that the conventional M2000 DI ellipsometer inherently measures a sample of surface area with a maximum of 15 cm diameter, which is only the central part of the 20 cm measured by our newly developed imaging ellipsometer, otherwise the thickness bars in the each maps shown in Figure 5.25 and Figure 5.26 are divided into 12 equal color bars of only 0.5nm, which is more or less comparable to the atomic layer of the oxides. The 12 equal color bars is chosen to fit the default color scale interval of the CompleteEase software of the Woollam M–2000 DI SE.

The most important observation from these experiments is that, there is only less than 1nm oxide thickness values discrepancy between the two independent measurements, for each samples, carried out from our large area imaging tool and the conventional Woollam M–2000 DI SE.

Multilayer validation of the Bayesian analysis

To further evaluate the consistency of the calibration posterior obtained from the previous reference samples as informative prior in the Bayesian analysis, multilayer structures of Poly-Si on SiO_2 on Si Samples were selected to be analyzed using similar methodology. Two polycrystalline–silicon on silicon-dioxide samples prepared through the standard chemical vapor deposition (CVD) deposition on 6-inch-diameter (roughly 15 cm) crystalline silicon wafers. a-Si denotes an amorphous silicon layer.

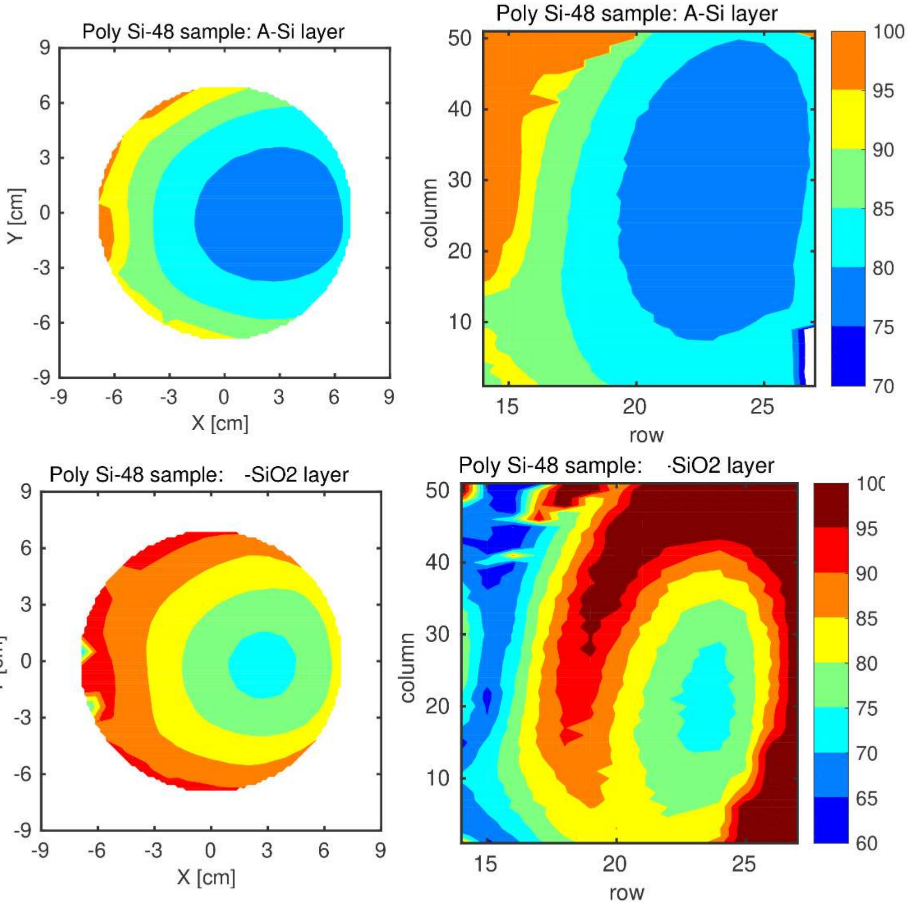

Figure 5.27. Thickness maps from the first poly-Si–silicon-dioxide film structure on a 6-inch-diameter Si-wafer by a Woollam M2000 ellipsometer (left) or by our device from cheap parts (right)

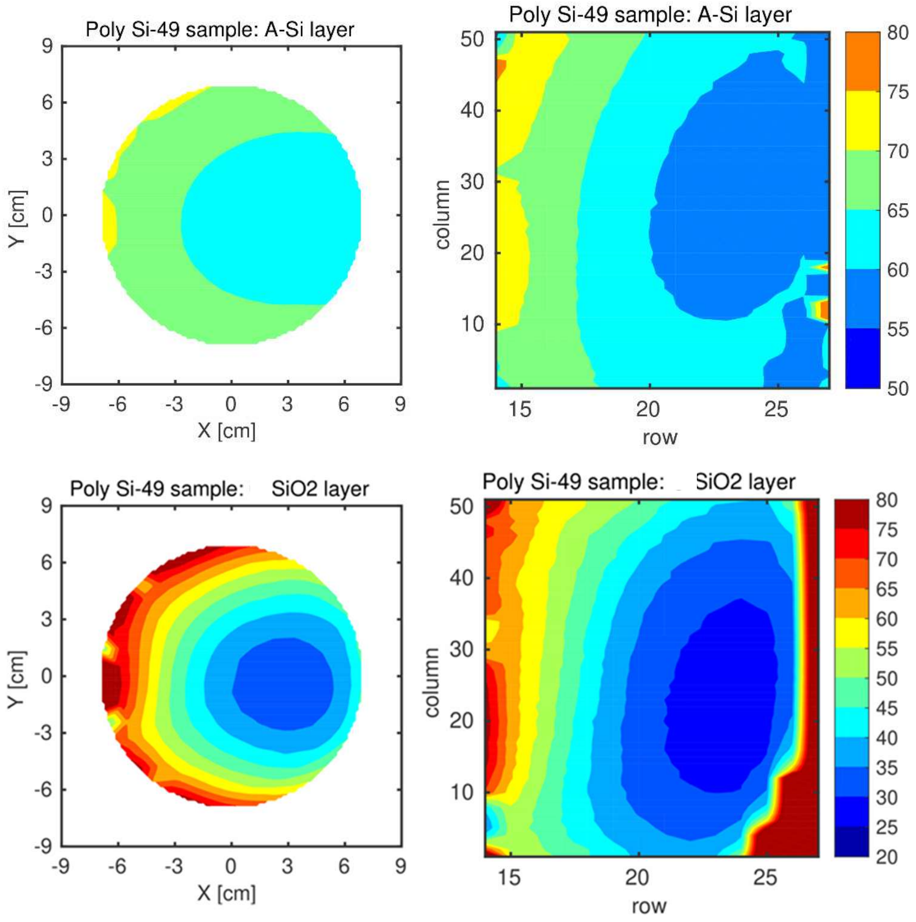

Figure 5.28. Thickness maps from the second poly-Si–silicon-dioxide film structure on a 6-inch-diameter Si-wafer by a Woollam M2000 ellipsometer (left) or by our device from cheap parts (right)

The agreement between the poly–Si thickness values obtained from our RGB ellipsometer and the conventional J.A. Woollam M2000 DI ellipsometer falls approximately within 1 nm, despite the fundamental spectral and spatial resolution differences between these two systems, summarized in Table 5.1 below.

Table 5.1. Fundamental differences between M2000 DI SE and our RGB ellipsometer.

System	M2000 DI SE	RGB ellipsometer
Mapping type	Scanning	Imaging
Spectra bands	Full spectra at each point	Three broadband spectra
Spot size	1mm	~ 5mmx5mm
Area coverage	Max 15 cm diameter	30x30 cm^2 (Theoretically ~150 cm)

To further quantify the agreement, a comparative error analysis was performed for the second poly–Si/SiO$_2$/Si sample, using the device with smaller pixel groups. Figure 5.29 and Figure 5.30 show the smoothed thickness maps of fitted values of poly-Si and SiO$_2$ layers (left maps), the differences between the smoothed and M2000 thickness values (middle maps), and the distribution of the thickness differences.

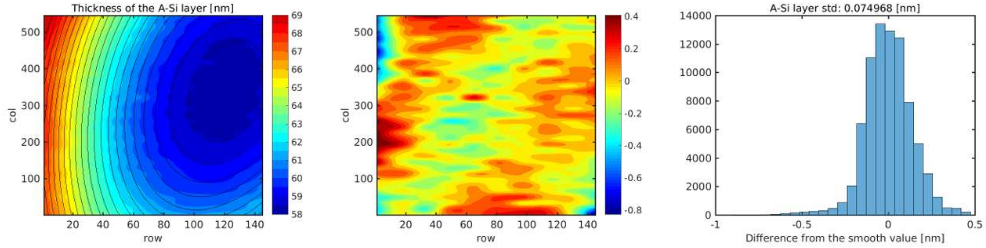

Figure 5.29. Smoothed thickness map of poly-Si layer (from Figure 5.28). Difference in the smoothed and M2000 thickness values. Histogram of the thickness differences. One color is 0.5 nm. Here, the valid area is shown with smaller pixel groups.

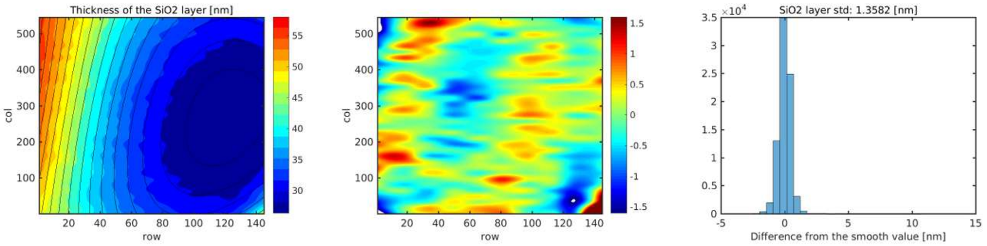

(a) (b) (c)

Figure 5.30. a) Smoothed thickness map of SiO$_2$ layer (from Figure 5.28) b). Difference in the smoothed and M2000 thickness values. c). Histogram of the thickness differences.
One color is 0.5 nm. Here, the valid area is shown with smaller pixel groups.

All in all, in the current method, the intensity-based forward model integrated with the Bayesian evaluation framework, considers into account the optical and structural imperfections and their corrections which were previously investigated in the LED-LCD monitor light source setup, measurement noise and previous information on the sample structure while enabling direct analysis of the recorded RGB intensity signals. This method turns out to be an appropriate way of treating this cases and closely agrees with our previous results, the monitor calibration using the rho method.

It is evident that the three RGB broadband spectral channels limitation, while this configuration is sufficient for robust thickness mapping of well-defined layer structures, it restricts the amount of independent spectral information available for simultaneously determining multiple optical parameters. Despite these limitations, the results show that the calibrated RGB ellipsometric mapping system, combined with a Bayesian evaluation strategy, provides reliable and quantitatively interpretable thickness maps for technologically relevant SiO_2/Si and poly-Si/SiO_2/Si structures. The method is therefore well suited for applications where fast, large-area mapping and transparent uncertainty quantification are more critical than full spectroscopic parameter reconstruction [69].

5.2. Small area (Microscopic Imaging)

5.2.1. Prototype of a new microscopic ellipsometer using point-like light source

At present, ellipsometric microscope is described in published patent document US5, 754,296 [61]. That system typically employs a collimated illuminating beam along with imaging optical elements and lenses to perform micron-resolution imaging of the sample, illuminating all measured sample points with light at an identical angle of incidence [51]. A similar optical approach is presented in a publication [35], which also describes an imaging ellipsometer. In this setup, a parallel beam illuminates the sample, and an imaging lens creates an image of the sample on the surface of the detector. This solution focuses on the analysis of biological protein samples and indicates that the method can detect the presence of specific protein layers as well as the interactions of different protein layers on the substrate surface. The imaging ellipsometry biosensor (IEB), first proposed in 1995 [36] has advanced from a simple concept to a powerful biosensor with high throughput, high sensitivity, specificity and low sample consumption. IEB can be applied to detect antigen– antibody complexes on a substrate. The biosensor system is utilizing specificities of biomolecular interactions in combination with protein-patterned surfaces. Visualization of the thickness distributions of thin layers (protein patterns) on a surface is achieved by using imaging ellipsometry. The biosensor system has the advantages of high spatial resolution, fast data acquisition, and simplicity in use [35].

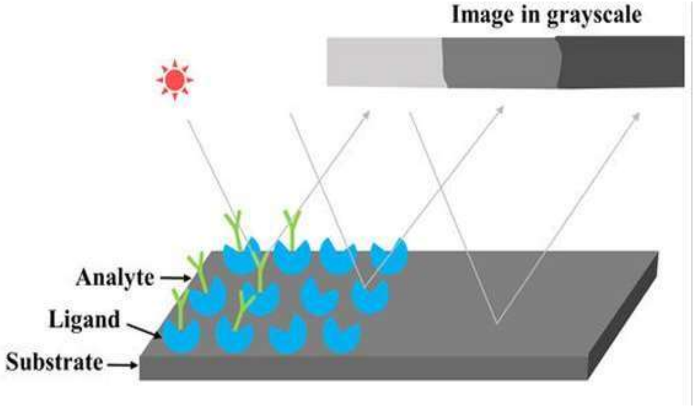

Figure 33. The principle of imaging ellipsometry biosensor (IEB) for detection of biomolecule interactions.

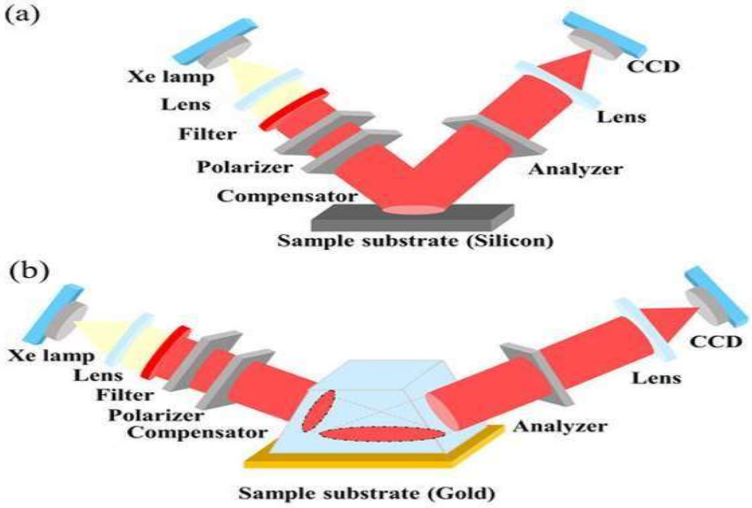

Figure 34. Schematic illustration of (a) imaging ellipsometry biosensor (IEB) in the external reflection condition and (b) total internal reflection imaging ellipsometry biosensor (TIRIEB).

A trapezoidal prism is used to couple the detection beam to the sensing surface. The polarized collimated beam is propagated perpendicularly to the prism and onto the sensing surface [35].

Our Laboratory developed and applied a new microscopic ellipsometer which is an optical magnifying device using a non-collimated light beam without a lens, which is suitable for measuring the change in polarization state of light reflected from or passing through very small (~1 mm^2) surfaces or volumes of various materials. The lateral resolution of this microscopic ellipsometer is in the order of microns, thus enabling the rapid and simultaneous mapping examination of these materials with high resolution. This optical testing device is particularly advantageous for the high-resolution, non-destructive, rapid, and simple optical mapping examination of very small surfaces of various materials, e.g. thin layers deposited by physical or chemical means, or biological samples on a substrate. This device is capable to make similar measurements like the above imaging ellipsometry biosensor (IEB) but cheaper device.

Our device can use direct or virtual point light source with a polarizer. The angle-of-incidence is varied point-by-point so a special optical calibration method is needed using appropriate SiO_2 sample. After the calibration, different samples were measured and analyzed: continuous and patterned thin layers (Chromium-film on glass, a-Si, a-C, Au, Ag, protein) to determine the precision. The lateral resolution is better than 5 microns.

The basis of the work is a patent from our Institute: Major C, Fried M, Horváth Z Gy, Juhász G, Petrik P: Patent pending: P2400376, 2024.

In the picture below is the newly developed optical mapping ellipsometer prototype.

Figure 35. RGB laser, pinhole-polarizer-(optional) compensator, sample, sample-holder, polarization-sensitive camera.

As shown in Figure 5.33, the newly developed microscopic ellipsometer uses a point light source from an RGB laser module. The device can use direct or virtual point light source with a polarizer. We tried to use a few microns size of a real or virtual point light source creating non-collimated illumination, and the sample was illuminated with light of adjustable polarization state. The miniature real or virtual light source by focusing a collimated light beam to a focal point using lens or using the end of a light guide fiber with micron size core was tried, too. During our investigations, we concluded that an ideal solution for the implementation of a high-resolution optical magnifying device is to direct a non-collimated beam from a sufficiently small, point-like source located near the sample onto the surface to be examined. The light is reflected from that surface, without imaging optical elements, lenses, and mirrors, to a detector system located at an appropriate distance. As a result, each object point can be measured at only one incidence (reflection) angle in a single step, and each object point corresponds to a different angle. Thus, the single image detected as a recording provides angle-dependent reflection data for the range of angles corresponding to the system's field of view. This means that each sample point measured at a different incidence angle with a resolution on the order of microns.

The best results were achieved using a point-like light source by focusing a collimated laser beam into an extremely (1–5 micron diameter) small pinhole, as this allows for significant noise reduction in the intensity distribution of the beam profile using the pinhole, using the Airy-disc as illumination spot, see Fig. 5.31.

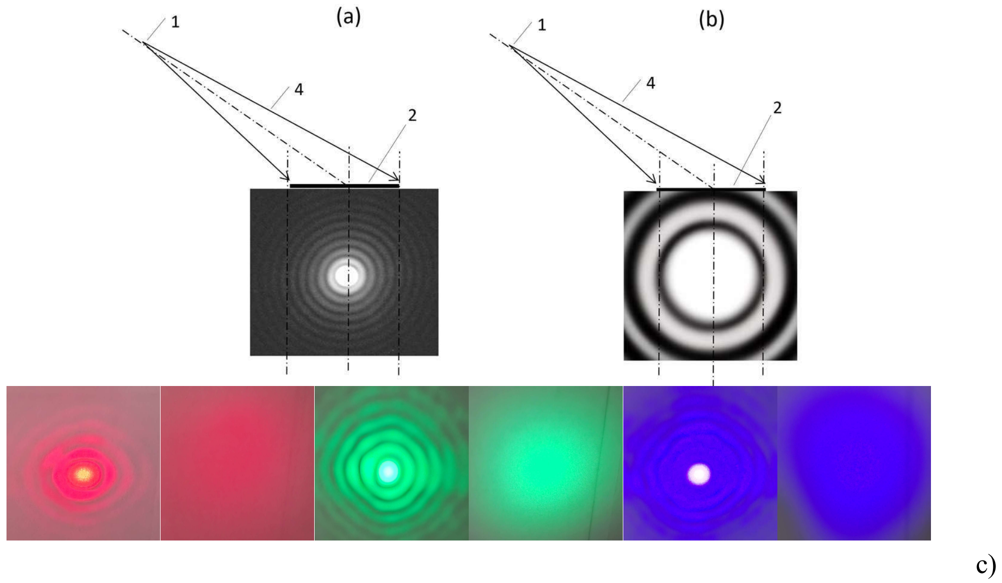

Figure 36. Light bending at the edges of the light source with respect to the wavelength

(a) For a relatively large light source size

(b) For a relatively small light source size and

(c) Picture of Airy-discs after 10 or 2 micron sized pinhole at different RGB colors.

We used a CMOS Pregius Polarsens sensor of model IMX250MZR, monochrome camera sensor that is sensitive to a polarization state, where the wavelength is controlled by the diode lasers. It is good for micron resolution, without moving parts, enabling shorter measurement times and simpler construction.

Optionally, one can use a compensator (λ/4 sheet), if the delta (Δ) ellipsometric angle is near 0 or 180 degrees, when Cos (Δ) is approaches 1 or -1. In such situations, we measure with quasi-rotating analyzer method, determining directly Cos (Δ) and the relative error is higher. Measuring the Cos Δ with 0.01 precision, the error in Δ is more than 5 degrees near 0 or 180 degrees, while the error in Δ is 0.5 degree near 90 degrees. This means more than 1 nm error in thickness near 0 or 180 degrees, while only 0.1 nm is the thickness error near 90 degrees.

However, the Δ value can be shifted with a compensator (λ/4 sheet) into a well measurable range, but it needs a very sophisticated, wavelength and position dependent, extra calibration. This can be the case if we want to measure on transparent substrate.

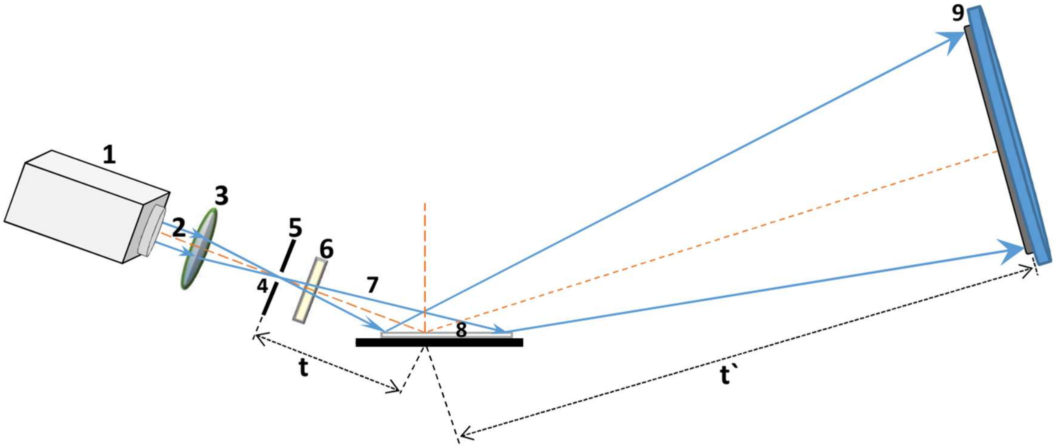

Figure 37. Best assessment of the micro-ellipsometer.

The light source (23) is a 3-color (465 nm, 520 nm, 635 nm) RGB diode laser, whose collimated light (6) is focused into a pinhole (5) by a lens (7), creating a point source (1). A film polarizer (10) is placed between the pinhole (5) and the sample (2), into the divergent beam (4). The camera is a polarization sensitive monochromatic version (3).

The Figure above shows the schematic draw of the best assessment of the device. The illuminating light source (23) in this case consists of a 3-color (465 nm, 520 nm, 635 nm) RGB laser source [62], whose collimated light (6) is focused into a pinhole (5) by a lens (7), thus creating a point source (1). The polarization state of the diverging beam (4) is adjusted by a polarization state generator (10) placed between the pinhole (5) and the sample (2), which in this case is a film polarizer, although other types of polarizers may also be used. The sample (2) being examined is arranged on a suitably designed (not separately indicated in the drawing) sample holder.

The surface of the sample considered to have a reflective surface is illuminated by diverging, linearly polarized light obtained from the pinhole (5). The light (4) reflected from the sample (2) falls on the sensor surface of the position and polarization-sensitive detector system (3), which in this case is a Sony polarizing computer-controlled digital CMOS monochrome camera, see Fig. 4.5.

The ratio of the distance (t) measured along the optical axis from the pinhole-sample to the sample-camera distance (t') results in a magnification of 25 times. The position and polarization-sensitive detector system (3) is conveniently formed by a special CCD matrix, above which micro-polarizers are arranged in a distribution of 0°-45°-90°-135° for every 2x2 pixel group, see Fig. 4.5. The size of an elementary pixel is 3.45 microns (Fig. 4.5 c), and the 2x2 pixel matrix or 'super-pixel' measures 7x7 microns (Fig. 4.5 b). The noise reduction and measurement accuracy could be enhanced through 4x4 super-pixel merging and the cooling of the detector (3). After the super-pixel merging, the detector (3) consisted of 255 x 306 merged pixels. The intensity ratios of the pixels in the detector (3) can determine the change in polarization state after the reflection of light on sample. The sample (2) can be displaced along at least one straight line in its own plane, e.g., in such a way that the examining arrangement outlined in Figure 5.35 is equipped to a manufacturing line that performs continuous movement. This displacement ensures that every point of the sample (2) passes at least once through the illuminating divergent beam of light (4) at every possible angle value of the detected cone angle range defined by the size of the pinhole (5) and the position and polarization-sensitive detector system (3) and their measured distances from each other. With the above device, the ellipsometric measurement of the sample (2) at more than ten thousand points simultaneously, at three wavelengths and with a lateral resolution of 5 microns, takes approximately 3 minutes, which is several orders of magnitude faster than devices that can measure point by point at a resolution of 5 microns.

As the arrangement involves different Angle-of-Incidence (AoI) that belong to all measured points, and a calibration process is needed to determine the AoI map before all other measurements. A SiO_2/Si sample of nominal thickness (20-80) nm is enough and we only need to fit the angle of incidence and the thickness (both parameters are wavelength independent) as unknown parameters in the simple optical model. Fig. 5.36 shows the result of such calibration process. The thickness map (Fig. 5.36 upper) shows values around 57 nm, the AoI map (Fig. 5.36 middle) shows values between 60-65 degrees. The MSE, the squared difference between the measured and calculated ellipsometric values (Tan ψ and Cos Δ) map shows the circular area where the light intensities are high enough to get reliable ellipsometric angles and where we can perform reliable microscopic measurements generally.

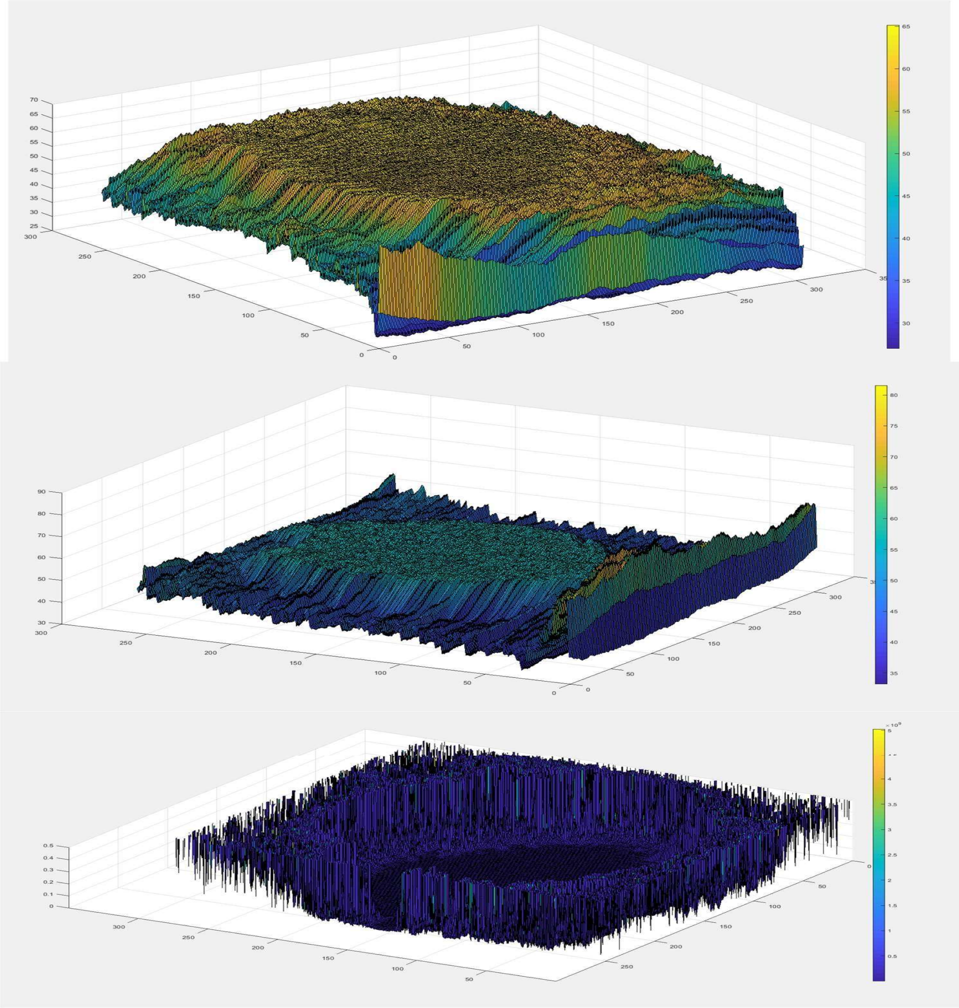

Figure 38. Angle-of-Incidence Calibration: SiO_2 layer on Si; SiO_2 thickness map [nm] (upper); Angle-of-Incidence [degree] map (middle); MSE map (lower).

Measurable area in this experiment is around 1 mm diameter.

Some selected measurements were carried out utilizing the prototype microscopic ellipsometer using point light source, but now without the compensator. The measurements are briefly discussed below for demonstration.

5.2.2. Measurement of ion implanted pattern

The sample, shown in Fig. 5.37, was made by Focused Ion Beam (FIB). We ion implanted 30 keV energy Ga-ions into 100 nm thick SiO_2 patterned crystalline Si-sample, converting the crystalline silicon (c-Si) into an amorphous silicon (a-Si) between the SiO_2 “walls”. The schematic pattern can be seen on the top part of the figure, where the dashed squares show the ion implanted 300x300 microns area. The narrowest lines are 10 microns wide.

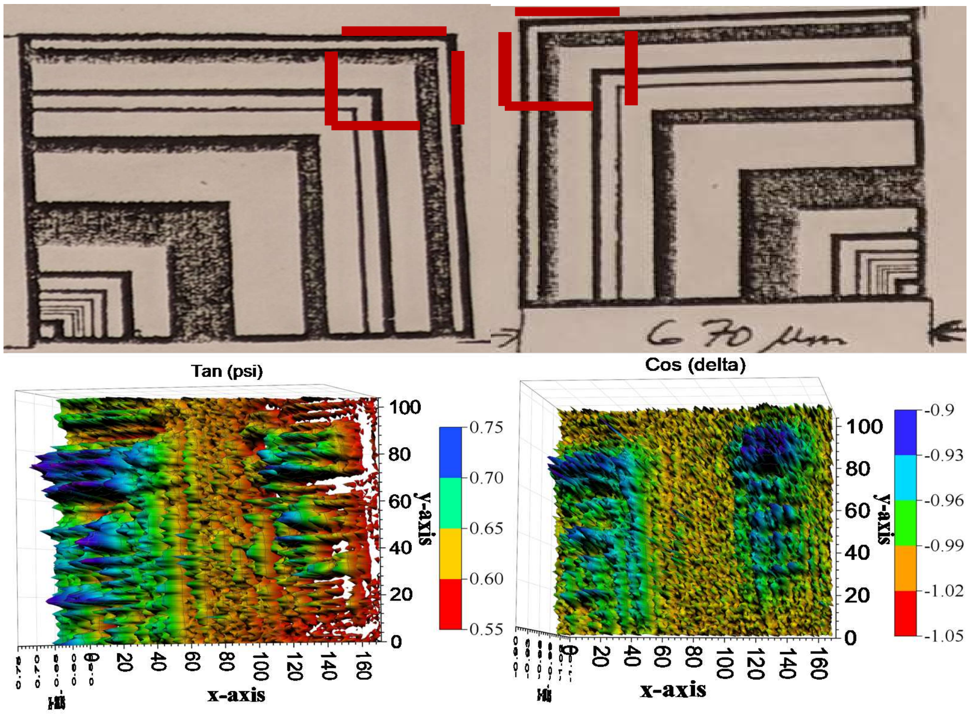

Figure 39. Ion implantation into oxide pattern, schematic pattern (top) and tan (psi) (bottom left), cos (delta) (bottom right).

After the ion implantation, we etched away the SiO_2 pattern, so we could measure the smooth Si surface with nearly 70 nm thick a-Si layers and unimplanted c-Si parts with only native oxide. One can see the patterned a-Si lines (Fig. 5.37, bottom left) and the low Mean Squared Error (MSE) values (Fig. 5.37, bottom right) corresponding to the a-Si lines. The unimplanted c-Si part is badly measurable, because of the nearly -1 Cos (Δ) values, causing high MSE (Mean Squared Error) values which show bad fit between measurement and calculation.

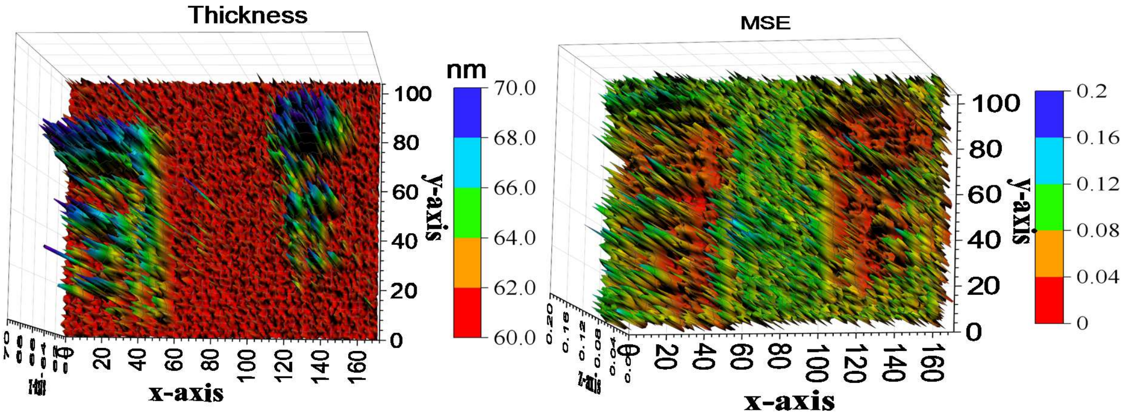

Figure 40. Ion implantation into oxide pattern, thickness in nm (left), and MSE (right).

5.2.3. Measurement of a Chromium micro-lithographic mask

The figure below, figure 5.39, illustrates another simplified sample, a Chromium micro-lithographic mask with 5x5 micron Cr squares on a glass substrate. We used the RGB laser module, whose collimated light is focused into a pinhole by a lens, see fig. 5.33. A linear film polarizer controls the polarization state of the diverging beam. After the sample, the chessboard-patterned, 5-micron side-length, square, chrome-coated layer creates an image of the sample on the detector due to the interference of light diffracted at the sides of the square elements, thus allowing the device to examine the surface elements of the sample. The reflected light falls onto the sensing surface of the position and polarization-sensitive detector system (polarization sensitive, computer controlled digital CMOS monochrome camera). The ratio of the distance of the pinhole pattern (t) to the sample-camera distance (t') gives a magnification of 25 times. With this setup, ellipsometric measurements of the sample can be performed at several tens of thousands of points simultaneously at 3 wavelengths. Fig. 5.39 a) and b) show the Tan ψ and Cos Δ "images", Fig. 5.39 c) shows the thickness map of the chromium with a resolution of about 5 microns. Fig. 5.39 d) shows the Mean Squared Error (MSE) map, showing good measurable places (low MSE) where the chromium film exists.

In case of the newly developed large area mapping tool using LCD-LED monitor light source, the DYK 33UX250 USB 3.0 Polarsens camera (a 2/3 inch Sony CMOS Pregius Polarsens sensor of model IMX250MYR) color sensitive camera variant was used, as shown in Figure 4.5. However, during the small area mapping tool microscopic ellipsometer that implements an RGB laser source light, the DZK 33UX250 USB 3.0 Polarsens camera (a 2/3 inch Sony

CMOS Pregius Polarsens sensor of model IMX250MZR) monochrome sensitive camera variant was used.

The monochrome sensitive camera variant offers relatively superior speed, flexibility and integration capability, which are crucial for real time optical mapping and imaging ellipsometry. In contrast, due to reduced sensitivity and polarization distortion, the color sensitive camera variant inherently compromise accuracy, resulting from the crosstalk and RGB filter interference because of the inclusion of the Bayer filter array. For colorimetric or multi spectral polarization imaging, though at the expense of the reduced sensitivity, the color sensitive camera variant excels the monochrome version.

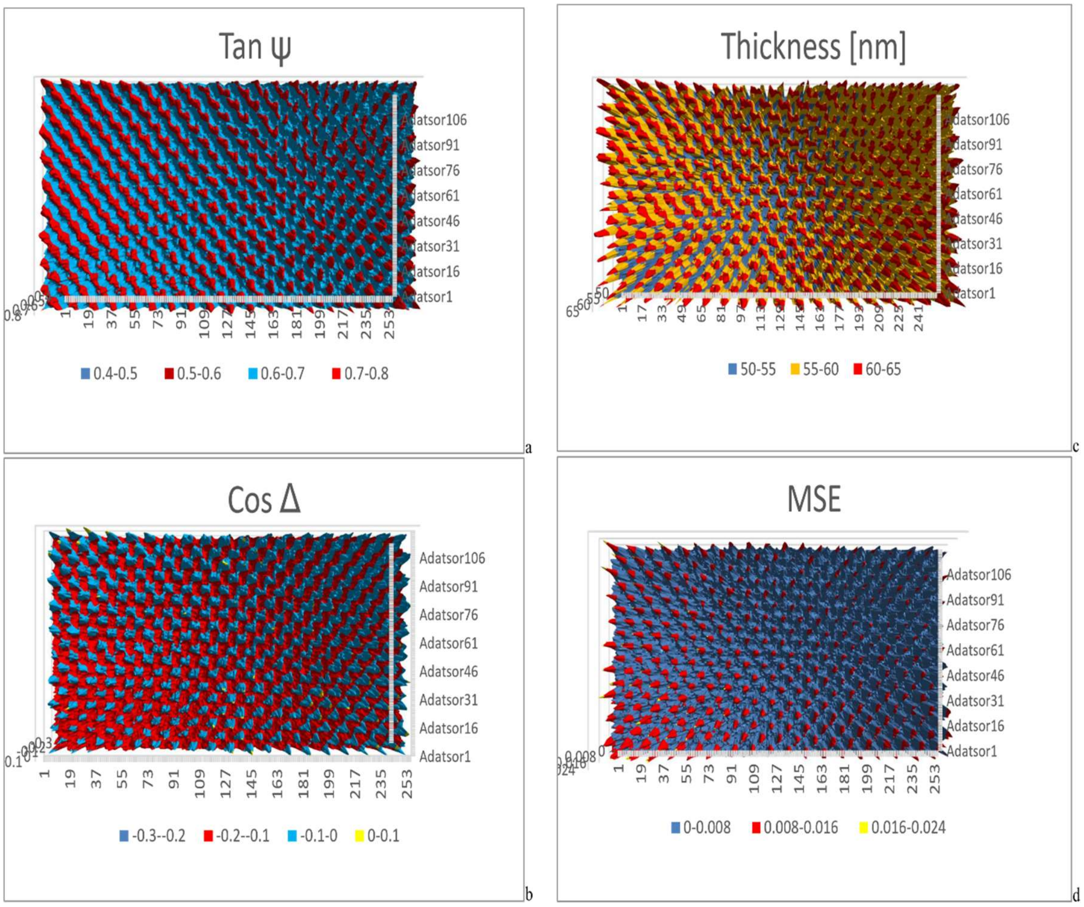

Figure 41. Micro-lithographic mask. 5x5 micron Cr squares on glass to check resolution Chromium layer thicknesses measured on the chessboard-patterned chrome-glass sample.

a) Tan (ψ) at 465 nm b) Cos (Δ) at 465 nm

c) Thickness map in nanometers d) The corresponding MSE map

Our device has advantageous effects that are mainly manifested in the visual representability of the measured data. The distortion-free image allows for simultaneous high resolution measurements over a wide range of angles, covering the small surface area of the examined sample. Visual representability means simultaneous measurement of many points of the sample without depth of field problem, reducing the measurement time. The reduction in measurement time also means applicability in production line and in real-time. It should be noted that the size and resolution of the generated image on the detector/screen can be simply regulated by changing the applied geometry.

5.2.4. Measurement of protein pattern

We prepared Polydimethylsiloxane micro-contact printing (PDMS μCP, short for stamp) with a chessboard-like pattern in sizes of 5 and 10 microns. Their optical microscopic images are shown in Figure 5.40. Unfortunately, the 5-micron version did not turn out well; it is not completely regular, therefore we present the results of protein measurements made with the 10-micron stamp. The used protein was Bovine serum albumin (BSA) which is a serum albumin protein derived from cows. Its shape is a prolate ellipsoid (14 × 4 × 4 nm). It is often used as a protein concentration standard in lab experiments.

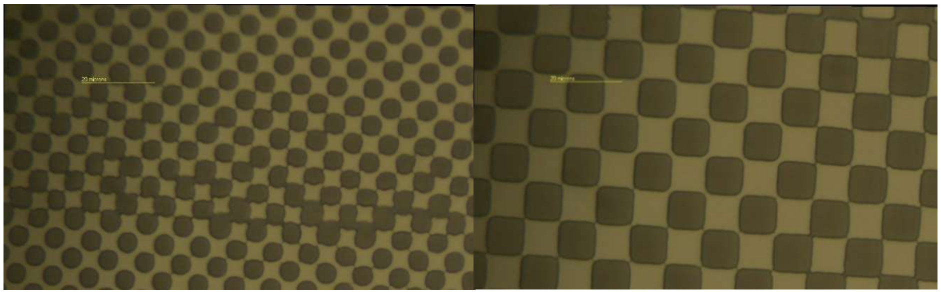

Figure 42. PDMS micro stamps, Left image: 5 μm and Right image: 10μm

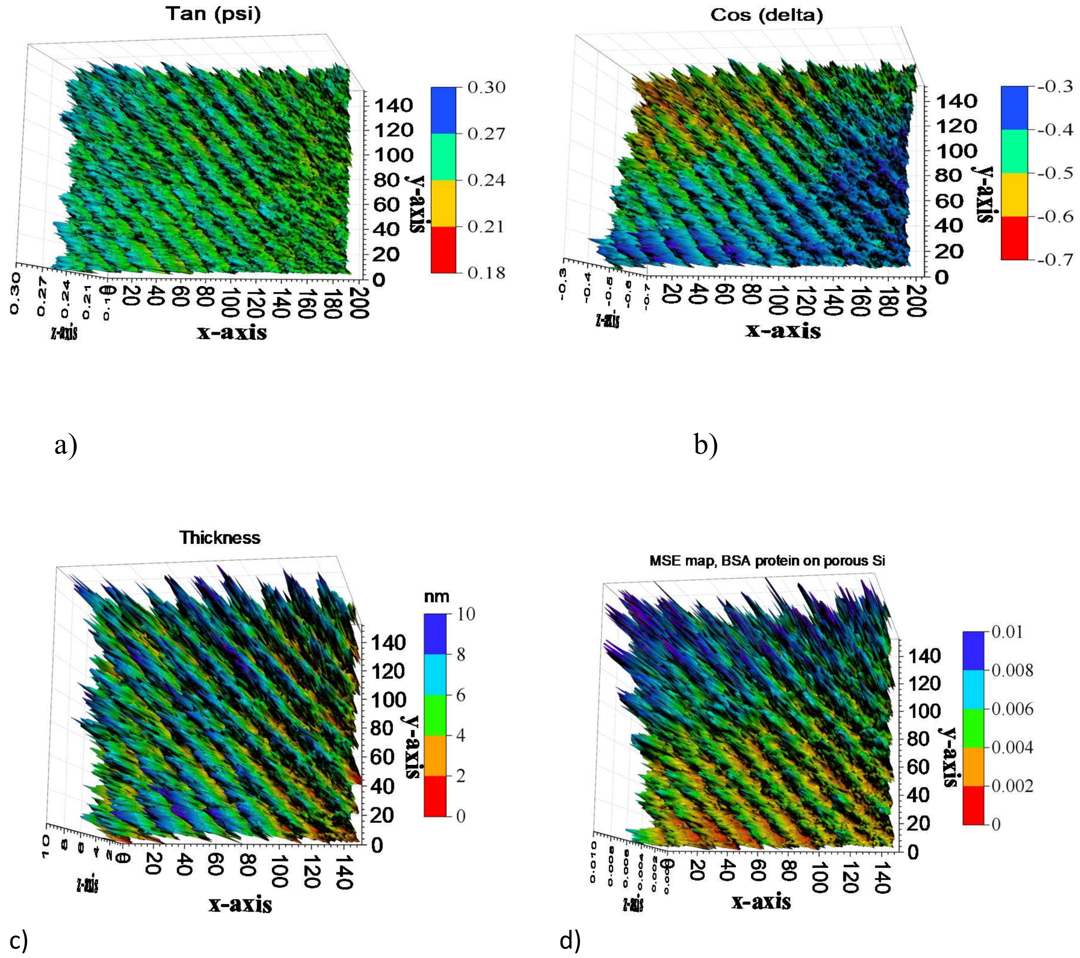

Figure 43. PDMS chessboard like stamps BSA protein. 10x10 micron stamp.

a) Tan (ψ) at 465 nm b) Cos (Δ) at 465 nm

c) Thickness map in nanometers and d) The corresponding MSE map

We showed the measurement results on a prepared sample in Fig. 5.41. The periodic structure in long-range contraction is already visible on the tan (ψ) and cos (Δ) maps, Fig. 5.30 a) and b), and due to different angles of incidence in various directions, the specific values vary continuously. The thickness map shows stripes because the protein squares meet at their corners, where the 5-micron resolution is not sufficient. The MSE map (Fig. 5.41 d) also indicates where the protein is (good fit, low MSE) and where the bare substrate is. With this method, it was possible to deposit the protein onto the surface of the sample at the designed thickness (510 nm), therefore it may serve as an alternative method for creating sensor surfaces.

6. Conclusion

Overall, we developed a multi-color ellipsometric-mapping tool from inexpensive parts and applied a new calibration method to carry out the thin film thickness measurement fast and accurate. Our new optical mapping equipment made by an ordinary color LED monitor and a polarization sensitive camera can measure big area in one second shot, while conventional ellipsometric devices needs several minutes to scan big area. After a careful calibration, the accuracy of our device is less than 1 nm.

In addition, in the newly developed microscopic ellipsometer prototype with a point –like RGB laser light sources, we have a device without depth of field problems, without of much of device calibration demand.

The device features relatively inexpensive components and contains no moving parts, making it extremely fast and capable of high throughput. It can be utilized in industrial, agricultural, and quality control applications that involve microscopy — such as by jewelers, geologists, and currency counterfeiting — as well as for laboratory and research purposes.

In biotechnology and medical fields, the device can be effectively used for a variety of purposes, including:

- Early tumor diagnosis
- Detection of clinical therapeutic markers
- Monitoring the binding of various molecules to surfaces
- Tracking environmental pollutants

To perform these analyses, one simply needs to prepare surface-sensitized samples tailored to the specific application and place them into the sample holder of the compact device. This allows for the detection of the presence of target substances in the test fluid.

The basis of the work is a patent from our Institute: Major C, Fried M, Horváth Z G, Juhász G, Petrik P: Patent pending: P2400376, 2024.

During the conventional ellipsometric mapping, the data collection is relatively slower and use a scanned small spot, while our new optical mapping tool from cheap parts measures a large area in one shot.

Therefore, the newly developed optical mapping tool from inexpensive parts, demonstrates functionality measurement capability, as confirmed by the initial characterization of the thermally grown SIO_2/Si reference sample. The obtained tan (Ψ) and cos (Δ) 3D surface graphs clearly demonstrate the mapping tools are of great characterization devices.

Generally,

- The new prototype is fast imaging (only seconds) and set up from cheap parts
- Ellipsometric data of large areas (even square meter size) can be collected in less than 10 seconds compared to the several minutes of “traditional” scanning methods.
- Wide mapping area, up to 150 cm is possible, if we use big LCD TV instead of a monitor.
- No moving parts, leading to higher stability.

Nevertheless, there are systemic limitations,

- Only three wide wavelength bands (RGB) are in action, which narrows the range of the light band source.
- Besides, there is a ‘0.1 degree’ angle uncertainty from the digital angle gauge used in rotation angle of the LCD monitor, which may be estimated to contribute to the experimental result deviation from the precise value as the incident polarization state of the light is determined by the rotation angle of the monitor.

Thesis Statements

1. I have shown that it is possible to make a non-destructive optical imaging device from inexpensive parts (LCD-LED monitors, TVs for light source and polarization sensitive camera as a light detector) to measure in one shot on large, macro area, sample sizes. [1, 2]
2. I have shown that it is possible to make a non-destructive optical imaging devices from inexpensive parts (RGB laser diodes for light source and polarization sensitive camera as a light detector) to measure in one shot on small (mm size), micro area, sample sizes. [3]
3. After an appropriate subsequent calibration processes, I have shown that the devices (in points 1 and 2) can image a sample surface with a 1 nm thickness resolution on several 10 thousand pixels. [1-3]

Related Publications

[1] Zereay, Berhane N.; Kálvin, Sándor; Juhász, György; Major, Csaba; Petrik, Péter; Horváth, Zoltán G.; Fried, Miklós, “Optical Calibration of a Multi-Color Ellipsometric Mapping Tool Fabricated Using Cheap Parts” PHOTONICS 11 : 11 Paper: 1036 , 11 p. (2024) IF: 2.1

[2] Sándor Kálvin, Berhane Nugusse Zereay, György Juhász, Csaba Major, Péter Petrik, Zoltán György Horváth, Miklos Fried, “A new method to evaluate multi-color ellipsometric mapping on big area samples”, Sci 2026, 8, 17. https://doi.org/10.3390/sci8010017 IF: 3.28 Q1 (Multidisciplinary)

[3] Csaba Major, Berhane Nugusse Zereay, György Juhász, Péter Petrik, Zoltán György Horváth, Péter Fürjes, Boglárka Kovács, György Zoltán Radnóczi, Sandor Kurunczi, Róbert Horváth, Levente Illes, Tamás Kolonits, Csaba Dücső and Miklós Fried, "A new type of microscopic ellipsometer utilizing point-like light source" submitted in Sci IF: 3.28 Q1 (Multidisciplinary).

In Proceedings

Nugusse, Berhane ; Juhász, György ; Major, Csaba ; Petrik, Péter ; Kálvin, Sándor ; Horváth, Zoltán György ; Fried, Miklós Multi-color ellipsometric mapping tool from cheap parts PROCEEDINGS OF SPIE - THE INTERNATIONAL SOCIETY FOR OPTICAL ENGINEERING 12428 pp. 134-141. , 8 p. (2023) IF: 0.28

Nugusse, Berhane ; Juhász, György ; Major, Csaba ; Petrik, Péter ; Kálvin, Sándor ; Horváth, György Zoltán ; Fried, Miklós “Optical calibration of the ellipsometric mapping tool from cheap parts” In: Fried, Miklós (szerk.) Symposium on Materials Science 2024 Mátraháza, Magyarország : Óbudai Egyetem (2025) 39 p. pp. 26-32. , 7 p.

Nugusse, Berhane ; Juhász, György ; Major, Csaba ; Petrik, Péter ; Kálvin, Sándor ; Horváth, Zoltán György ; Fried, Miklós “Multi-color ellipsometric mapping tool from cheap parts” In: Fried, Miklós (szerk.) Symposium on Materials Science 2022 Budapest.

7. Possible further developments

In this research work, we have successfully demonstrated the design, calibration and of a newly developed Macro and Micro imaging ellipsometers, which are both capable of measuring large area and small area samples with a faster speed, larger area mapping capacity when compared with the corresponding conventional ellipsometers.

However, as a continuous improvement of our mapping tool setups for further optimized and precise results, there remains a significant scope for the future enhancement, in terms of both the instrumentation and data analysis methods, using the current configuration as a baseline establishment.

a) Expansion of the Imaging field using a larger LCD monitors

In this current work, a liquid crystal display window (Dell Ultra-Sharp™ U2412M, GB-LED) with an active diagonal viewable size of approximately 61cm (24inches) is used in as the main source of a polarized measurement beam for our large area imaging ellipsometric arrangement as both the projection screen and the polarization modulator. Our small area-imaging tool (microscopic ellipsometer) uses an RGB laser light module for the same purpose.

In order to enable wide-field imaging of extended samples and wafer-scale structures, the current system configuration is planned to be upgraded in subsequent work employing a big LCD television panel that is more than 2 meters diagonal in dimension.

The future modification may give rise to,

- An expanded range of mapping area and a field of view
- Enhanced signal-to-noise ratio and image resolution
- Facilitate multi angle and multi wavelength imaging due to the ample area for parallel angle resolved illumination and data analysis.

Note that similar to our previous alignment, calibration and validation procedures, this new configuration will require careful optical realignments and advanced LCD window rho-correction methods.

b) Integration of a deep learning for a quicker automated data analysis and better accuracy

In the current research work, the ellipsometric data analysis and interpretation has merely relied on the WVASE (Woollam Variable Angle Spectroscopic Ellipsometry) and custom Matlab-based complementary modelling. Despite their reliable results, they remain computationally intensive for the pixel-by-pixel processing of high-resolution images data mapping.

Therefore, we propose a deep learning based ellipsometric data analysis, which obviously require a collection of huge ellipsometric data sets for training from the forward ellipsometric model or other experimental results of previous works. The adaption of this technique is expected to yield a rapid evaluation of the optical properties, thin film thickness extraction their roughness estimation, real time thickness mapping over large area pixel images on minimal time and computational cost.

The cumulative result of the above two improvements is expected to enhance the characterization of the large area device inspection and machine vision assisted material diagnostics.

The ultimate goal of this research is to transform these current mapping tools into an industrial inline characterization imaging ellipsometers, but from inexpensive parts.

8. Bibliography

[1]. Fujiwara H. and R. W. Collins, (2018). Spectroscopic Ellipsometry for Photovoltaics, Springer Series in Optical Sciences 212, Springer International Publishing AG, part of Springer Nature. https://doi.org/10.1007/978-3-319-75377-5_2

[2]. Fujiwara, H. (2007). Spectroscopic ellipsometry: principles and applications. John Wiley & Sons. https://doi.org/10.1002/9780470060193

[3]. Gauglitz and Vo-Dinh T, 2003, Handbook of Spectroscopy, Auf der Morgenstelle, Tübingen, Germany.

[4]. Maria, L, Michael, B, Giovanni, B, Denis, C, Christoph, C, Antonello, M, Karsten, F, Zorana, D, Norbert, E, Melanie, G, Rados, G, Dusˇan, H, Kurt, H, Josef, H, Razvigor, O, Zoran V. Popovic, O, 2009, ‘Spectroscopic ellipsometry and polarimetry for mateials and systems analysis at the nanometer scale: state-of-the-art, potential, and perspectives’, J Nanopart Res, Vol.11 pp. 1521–1554.

[5]. [A. Nazarov, M. Ney, I. Abdulhalim, Opt. Express 2020, 28, 9288]

[6]. Li, Yifei, Wu, Yifeng, Yu, Heshan, Takeuchi, Ichiro and Jaramillo, Rafael. 2021. "Deep Learning for Rapid Analysis of Spectroscopic Ellipsometry Data." Advanced Photonics Research, 2 (12).

[7]. Dien, N, Hongshen, L, Nisha, S, Raymond, L, Nikolas, J, Podraza, Marie, C, Stéphane, G, Seong, H, 2018, ‘Spectroscopic ellipsometry study of thickness and porosity of the alteration layer formed on international simple glass surface in aqueous corrosion conditions’, Nature partner Journal, Vol. 2 pp20.

[8]. Weber, J. W., Hansen, T. A. R., Van de Sanden, M. C. M., & Engeln, R. (2009). B-spline parametrization of the dielectric function applied to spectroscopic ellipsometry on amorphous carbon. Journal of Applied Physics, 106(12).

[9]. M. Gilliot, (2019). Wavelength-by-wavelength Kramers--Kronig consistent inversion of ellipsometry data. Optica Publishing Group, V58, p8153. https://opg.optica.org/ao/abstract.cfm?uri=ao-58-30-8153

[10]. Fried, M., Juhász, G., Major, C., Petrik, P., Polgár, O., Horváth, Z., Nutsch, A. Expanded beam (macro-imaging) ellipsometry. *Thin Solid Films* 2011, *519*, 2730–2736. [CrossRef]

[11]. Petrik, P., & Fried, M. (2022). Mapping and imaging of thin films on large surfaces. physica status solidi (a), 219(13), 2100800.

[12]. Harland G. Tompkins, 2005, Handbook OF Ellipsometry, Thin Films Materials Science Consultant Chandler, Arizona And Eugene A. Irene Department of Chemistry, University of North Carolina Chapel Hill, North Carolina pp 237.

[13]. Collins, R. W. (2018) 'Measurement technique of ellipsometry', Springer Series in Optical Sciences, 212(1), pp. 19–58.

[14]. Yu, W., Cui, C., Li, H., Bian, S., & Chen, X. (2022, August). FDTD-based study on equivalent medium approximation model of surface roughness for thin films characterization using spectroscopic ellipsometry. In Photonics (Vol. 9, No. 9, p. 621).

[15]. D. Abou-Ras, R. Caballero, C.-H. Fischer, C. A. Kaufmann, I. Lauermann, R. Mainz, H. Mönig, A. Schöpke, C. Stephan, C. Streeck, S. Schorr, A. Eicke, M. Döbeli, B. Gade, J. Hinrichs, T. Nunney, H. Dijkstra, V. Hoffmann, D. Klemm, V. Efimova, A. Bergmaier, G. Dollinger, T. Wirth, W. Unger, A. A. Rockett, A. Perez-Rodriguez, J. Alvarez-Garcia, V. Izquierdo-Roca, T. Schmid, P.-P. Choi, M. Müller, F. Bertram, J. Christen, H. Khatri, R. W. Collins, S. Marsillac, I. Kötschau, Comprehensive comparison of various techniques for the analysis of elemental distributions in thin films. *Microscopy Microanal.* **2011**, *17*, 728-51.

[16]. S. Logothetidis, D. Georgiou, A. Laskarakis, C. Koidis, N. Kalfagiannis, In-line spectroscopic ellipsometry for the monitoring of the optical properties and quality of roll-to-roll printed Nano-layers for organic photovoltaics, Solar Energy Mater. Solar Cells 2013, 112, 144-156.

[17]. M. A. Razooqi Alaani, P. Koirala, P. Pradhan, A. B. Phillips, N. J. Podraza, M. J. Heben, R. W. Collins, Tailoring the CdS/CdSe/CdTe multilayer structure for optimization of photovoltaic device performance guided by mapping spectroscopic ellipsometry, *Solar Energy Mater. Solar Cells* **2021**, *221*, 110907.

[18]. Ralph F. Cohn, James W. Wagner and Jerome Kruger, Dynamic Imaging Microellipsometry: Proof of Concept Test Results, *J. Electrochem. Soc.* **1988** *135,* 1033.

[19]. P. Boher, J. Petit, T. Leroux, J. Foucher, Y. Desières, J. Hazart, and P. Chaton, Optical Fourier transform scatterometry for LER and LWR metrology, *Proc. SPIE* **2005** *5752*, 192–203.

[20]. N. Kumar, P. Petrik, G. K. P. Ramanandan, O. El Gawhary, S. Roy, S. F. Pereira, W. M. J. Coene, H. P. Urbach, Reconstruction of sub wavelength features and nano-positioning of gratings using coherent Fourier scatterometry, *Opt. Express* **2014** *22*, 24678–24688.

[21]. S. Roy, N. Kumar, S. F. Pereira, and H. P. Urbach, Interferometric coherent Fourier scatterometry: a method for obtaining high sensitivity in the optical inverse-grating problem, *J. Opt*. **2013** *15*, 75707–75715.

[22]. P. Petrik, N. Kumar, M. Fried, B. Fodor, G. Juhasz, S. F. Pereira, S. Burger, H. P. Urbach, Fourier ellipsometry – an ellipsometric approach to Fourier scatterometry, *J. Eur. Opt. Soc. – Rapid* **2015** *10*, 15002.

[23]. U. Wurstbauer, C. Röling, U. Wurstbauer, W. Wegscheider, M. Vaupel, P. H. Thiesen, W. Weiss, Imaging ellipsometry of grapheme, Appl. Phys. Lett. 2010, 97, 231901.

[24]. D. Rosu, P. Petrik, G. Rattmann, M. Schellenberger, U. Beck, A. Hertwig, Optical characterization of patterned thin films, Thin Solid Films 2014, 571, 601-604.

[25]. D. Necas, I. Ohlídal, D. Franta, V. Cudek, M. Ohlídal, J. Vodák, L. Sládková, L. Zajíˇcková, M. Eliáš, F. Vižd'a ,Assessment of non-uniform thin films using spectroscopic ellipsometry and imaging spectroscopic reflectometry, Thin Solid Films 2014, 571, 573-578.

[26]. IMAGING OPTICAL INSPECTION DEVICE WITH A PINHOLE CAMERA”; Pub. No.: WO/2008/142468; International Application No.: PCT/HU2008/000058 Publication Date: 27.11.2008 International Filing Date: 23.05.2008, US 8437002 B2, Priority Data: P 0700366, 23.05.2007, HU, Inventors: Zoltán György Horváth, György Juhász, Miklós Fried, Csaba Major, Péter Petrik.

[27]. G. Juhasz, Z. Horvath, C. Major, P. Petrik, O. Polgar, M. Fried, Non-collimated beam ellipsometry, Phys. Stat. Sol. (c) 2008 5, 1081-1084. https://doi.org/10.1002/pssc.200777862

[28]. C. Major, G. Juhasz, Z. Horvath, O. Polgar, M. Fried, Wide angle beam ellipsometry for extremely large samples, Phys. Stat. Sol. (c), 2008 5, 1077-1080. https://doi.org/10.1002/pssc.200777859

[29]. C. Major, G. Juhasz, P. Petrik, Z. Horvath, O. Polgar, M. Fried, Application of wide angle beam spectroscopic ellipsometry for quality control in solar cell production, Vacuum 2009 84, 119-122.

[30]. A. Shan, M. Fried, G. Juhász, C. Major, O. Polgar, A. Nemeth, P. Petrik, L.R. Dahal, Jie Chen, Zhiquan Huang, N.J. Podraza, R.W. Collins, High Speed Imaging/Mapping Spectroscopic Ellipsometry for In Line Analysis of Roll to Roll Thin Film Photovoltaics, IEEE Journal of Photovoltaics, 2014 4:(1), 355-361.

[31]. M. Fried, On-line monitoring of solar cell module production by ellipsometry technique, *Thin Solid Films*, **2014** *571*, 345-355.

[32]. D. Beaglehole, Performance of a microscopic imaging ellipsometer, *Rev. Sci. Instrum.* **1988** *59*, 2557–2559.

[33]. S Funke, B Miller, E Parzinger, P Thiesen, A W Holleitner and U Wurstbauer, Imaging spectroscopic ellipsometry of MoS2, *Journal of Physics: Condensed Matter*, **2016** *28*, 385301.

[34]. Liu, H., Shen, J., Liu, W., Niu, Y., & Jin, G. (2020). Imaging ellipsometry biosensor: Basic theory, principles of operation, and applications. *Journal of Vacuum Science & Technology B*, *38*(2).

[35]. Haoyu Liu, Jia Shen, Wei Liu, Yu Niu, Gang Jin; Imaging ellipsometry biosensor: Basic theory, principles of operation, and applications. *J. Vac. Sci. Technol. B* **2020** *38(2),* 024002.

[36]. Gang Jin, Pentti Tengvall, Ingemar Lundström, Hans Arwin, A Biosensor Concept Based on Imaging Ellipsometry for Visualization of Biomolecular Interactions, *Analytical Biochemistry*, **1995** *232*, 69-72. https://doi.org/10.1006/abio.1995.9959

[37]. Bakker, J.W.; Arwin, H.; Lundström, I.; Filippini, D. Computer screen photoassisted off-null ellipsometry. *Appl Opt.* **2006**, *45*, 7795–7799. https://doi.org/10.1364/AO.45.007795 , [CrossRef] [PubMed].

[38]. Durão, L. M., & Loureiro, N. C. (2025). Non-Destructive Testing of Materials and Parts—Techniques, Case Studies and Practical Applications. *Materials*, *18*(14), 3312. https://doi.org/10.3390/ma18143312

[39]. jawoollam.com, Ellipsometry-FAQ J.A. Woollam (accessed on 27 Oct 2025 13:36 CET) https://www.jawoollam.com/resources/ellipsometry-faq#:~:text=The%20upper%20thickness%20limit%20for,better%20separated%20at%20longer%20wavelengths.

[40]. Semilab Co. Available online: https://semilab.com/hu/product/799/fpt (Accessed on 02 October 2025)]

[41]. J.A.Woollam Co. Available online: https://www.jawoollam.com/download/pdfs/accumap-se-brochure.pdf (Accessed on 02 October 2025)

[42]. Semilab Co., Spectroscopic Ellipsometry, Available online https://semilab.com/category/products/spectroscopic-ellipsometry-ltps (Accessed on 02 October 2025), M. Osborne, New Product:

[43]. J.A. Woollam's AccuMap-SE provides thin film measurement of panel uniformity, PCTech,

https://www.pv-tech.org/new_product_j-a-_woollams_accumap-se_provides_thin_film_measurement_of_pane/ (Accessed on 02 October 2025)

[44]. Collins, R. W., & Kim, Y. T. (1990). Ellipsometry for thin-film and surface analysis. *Analytical Chemistry*, *62*(17), 887A-900A.

[45]. Gruska, B. (2000). Ellipsometric analysis of polysilicon layers. *Thin solid films*, *364* (1-2), 138-143.

[46]. Ibok, E., & Garg, S. (1993). A characterization of the effect of deposition temperature on polysilicon properties: Morphology, dopability, etchability, and polycide properties. *Journal of the Electrochemical Society*, *140*(10), 2927.

[47]. Riegler, H. A user's guide to ellipsometry. By Harland G. Tompkins, Academic Press, New York 1993, 260 pp. hardback, ISBN 0-12-603050-0. *Adv. Mater.* **1993**, *5*, 778. https://doi.org/10.1002/adma.19930051034

[48]. M. N. Polyanskiy. Refractiveindex.info database of optical constants. *Sci. Data* 11, 94 (2024) https://doi.org/10.1038/s41597-023-02898-2

[49]. Aspnes, D. E., & Studna, A. A. (1983). Dielectric functions and optical parameters of si, ge, gap, gaas, gasb, inp, inas, and insb from 1.5 to 6.0 ev. *Physical review B*, *27*(2), 985. https://doi.org/10.1103/PhysRevB.27.985

[50]. Fodor, B., Kozma, P., Burger, S., Fried, M., & Petrik, P. (2016). Effective medium approximation of ellipsometric response from random surface roughness simulated by finite-element method. *Thin Solid Films*.

[51]. Shiyuan Liu, Weichao Du, Xiuguo Chen, Hao Jiang, and Chuanwei Zhang, "Mueller matrix imaging ellipsometry for nanostructure metrology," Opt. Express 23, 17316-17329 (2015) https://doi.org/10.1364/OE.23.017316.

[52]. Tompkins, H. G., & Hilfiker, J. N. (2015). Spectroscopic ellipsometry: practical application to thin film characterization. Momentum Press.

[53]. Politano, G. G., & Versace, C. (2023). Spectroscopic ellipsometry: advancements, applications and future prospects in optical characterization. Spectroscopy Journal, 1(3), 163-181.

[54]. Jellison Jr, G. E., & Modine, F. A. (1996). Parameterization of the optical functions of amorphous materials in the interband region. *Applied Physics Letters*, *69*(3), 371-373.

[55]. Salazar, D., Soto-Molina, R., Lizarraga-Medina, E. G., Felix, M. A., Radnev, N., & Márquez, H. (2016). Ellipsometric study of SiOx thin films by thermal evaporation. *Open Journal of Inorganic Chemistry*, *6*(03), 175. http://dx.doi.org/10.4236/ojic.2016.63013

[56]. Cushman, C., Smith, N., Kaykhaii, M., Podraza, N., & Linford, M. (2016). An introduction to modeling in spectroscopic ellipsometry, focusing on models for transparent materials: The Cauchy and Sellmeier models. Vacuum Technology & Coating, 7(01).

[57]. Ono, S. (2020). Snapshot multispectral imaging using a pixel-wise polarization color image sensor. Optics Express, 28(23), 34536-34573. https://doi.org/10.1364/OE.402947

[58]. https://www.nist.gov/laboratories/tools-instruments/nanofab-tool-j-woollam-m-2000-di-spectroscopic-ellipsometer (accessed on 21 Nov 2025, 1:10 am)

[59]. https://www.theimagingsource.com/products/industrial-cameras/usb-3.0-polarsens/dyk33ux250/ (accessed on 21 Nov 1:20 am)

[60]. Lane, C., Rode, D., & Rösgen, T. (2021). Calibration of a polarization image sensor and investigation of influencing factors. *Applied Optics*, *61*(6), C37-C45. https://doi.org/10.1364/AO.437391

[61]. https://patents.google.com/patent/US5754296 (accessed on 21 Nov 2025 4:34 am)

[62]. https://rgblasersystem.com/product/rgb0-3_sss-300mw-rgb-laser-module/ (accessed on 21 Nov 2025 4:44 am)

[63]. Wang, S. R., Li, L., Zhang, X. L., Bi, Y. G., Yang, Y. M., & Feng, J. (2025). Linearly polarized light emission in organic light-emitting devices with an elliptical Nano pillar array meta-electrode. *Optics Letters*, *50*(17), 5510-5513.

[64]. An, M. H., Ding, R., Zhang, X. L., Chen, S. N., Wang, Y. N., Ye, G. D., ... & Sun, H. B. (2022). Highly polarized emission from organic single-crystal light-emitting devices with a polarization ratio of 176. *Optica*, *9*(1), 121-129.

[65]. Ren, H., Yang, J., Liu, X., Huang, P., & Guo, L. (2020). Sensor Modeling and Calibration Method Based on Extinction Ratio Error for Camera-Based Polarization Navigation Sensor. *Sensors*, *20*(13), 3779. https://doi.org/10.3390/s20133779

[66]. Pincus, M. Letter to the Editor—A Monte Carlo Method for the Approximate Solution of Certain Types of Constrained Optimization Problems. Oper. Res. 1970, 18, 1225–1228. https://doi.org/10.1287/opre.18.6.1225

[67]. Kirkpatrick, S.; Gelatt, C.D., Jr.; Vecchi, M.P. Optimization by Simulated Annealing. Science 1983, 220, 671–680. https://doi.org/10.1126/science.220.4598.671

[68]. Polgar, O.; Fried, M.; Lohner, T.; Barsony, I. Comparison of algorithms used for evaluation of ellipsometric measurements: Random search, genetic algorithms, simulated annealing and hill climbing graph-searches. Surf. Sci. 2000, 457, 157–177

[69]. Sándor Kálvin , Berhane Nugusse Zereay, György Juhász, Csaba Major, Péter Petrik , Zoltán György Horváth and Miklós Fried. A New Method of Evaluating Multi-Color Ellipsometric Mapping on Big-Area Samples. Sci 2026, 8, 17. https://doi.org/10.3390/sci8010017

[70]. Sivia, D.S. *Data Analysis: A Bayesian Tutorial*, online ed.; Oxford University Press: Oxford, UK, 2006. https://doi.org/10.1093/oso/9780198568315.001.0001.

[71]. Gregory, P. *Bayesian Logical Data Analysis for the Physical Sciences: A Comparative Approach with Mathematica® Support*; Cambridge University Press: Cambridge, UK, 2012; ISBN 9780511791277. https://doi.org/10.1017/CBO9780511791277.

[72]. Barradas, N.P.; Keddie, J.L.; Sackin, R. Bayesian inference analysis of ellipsometry data. *Phys. Rev. E* **1999**, *59*, 6138–6151. https://doi.org/10.1103/physreve.59.6138.

[73]. Toussaint, U.V.; Dose, V. Bayesian Inference in Surface Physics. *Appl. Phys. A* **2006**, *82,* 403–413.

9. Appendix

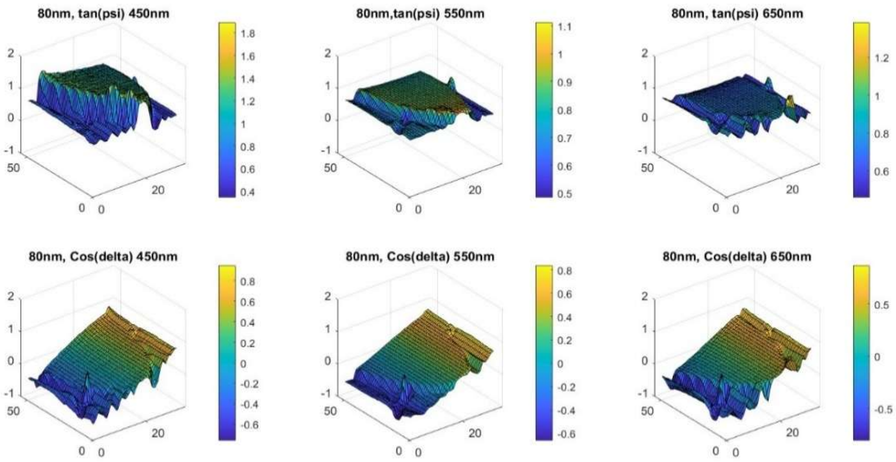

Figure 9.1. A 80nm SiO_2/Si substrate tan (Ψ) and cos (Δ) measurements for RGB spectrum

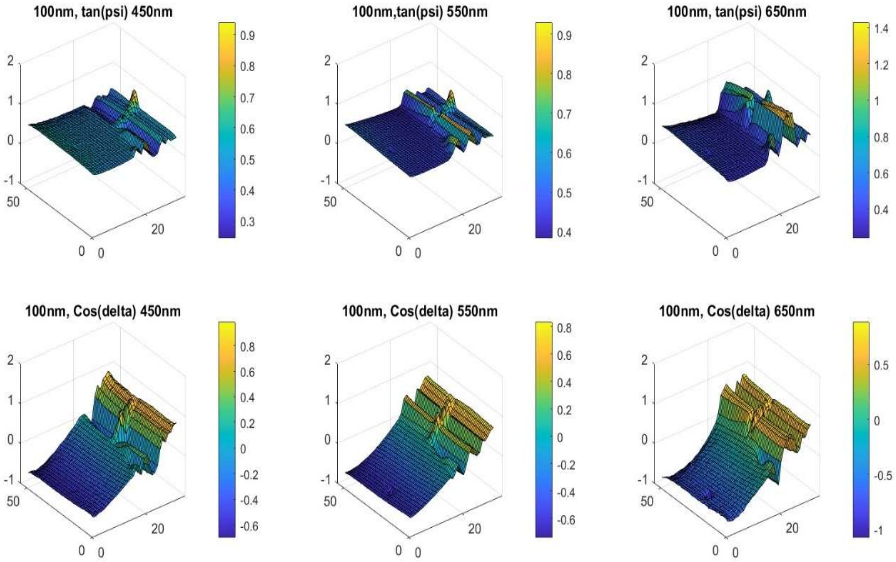

Figure 9.2. A 100nm SiO_2/Si substrate tan (Ψ) and cos (Δ) measurements for RGB spectrum

Table 1. Specifications of the DYK 33UX250 USB 3.0 Polarsens camera.

Vision Standard	USB3 Vision
Dynamic Range	12 bit
Resolution	2448x2048
Frame Rate at Full Resolution	75 fps
Pixel Formats	8-Bit Polarized Bayer (BG)12-Bit Polarized Bayer Packed (BG) 16-Bit Polarized Bayer (BG)
IR-Cut filter	Yes
Sensor Type and Specification	Sony IMX250MYR, CMOS Pregius Polarsens
Shutter Type, format	Global, 2/3 inch
Pixel Size	H: 3.45 µm , V: 3.45 µm
Lens Mount	C/CS
Interface	USB 3.0
Supply voltage	4.75 VDC to 5.25 VDC
Current consumption	approx. 800 mA @ 5 VDC
I/O Connector	12-pin connector for trigger and strobe or general purpose input/output
Dimensions	H: 29 mm, W: 29 mm, L: 43 mm
Mass	65 g
Shutter	1 µs to 4 s
Gain	0 dB to 48 dB

* For the *monochrome* version of the camera, DZK 33UX250 USB 3.0 Polarsens camera, the only change from the DZK 33UX250 USB 3.0 Polarsens color camera are the sensor format and sensor type where,

Sensor Format: 8-Bit Polarized Mono,12-Bit Polarized mono Packed,16-Bit Polarized Mono

Sensor type: Sony IMX250MZR

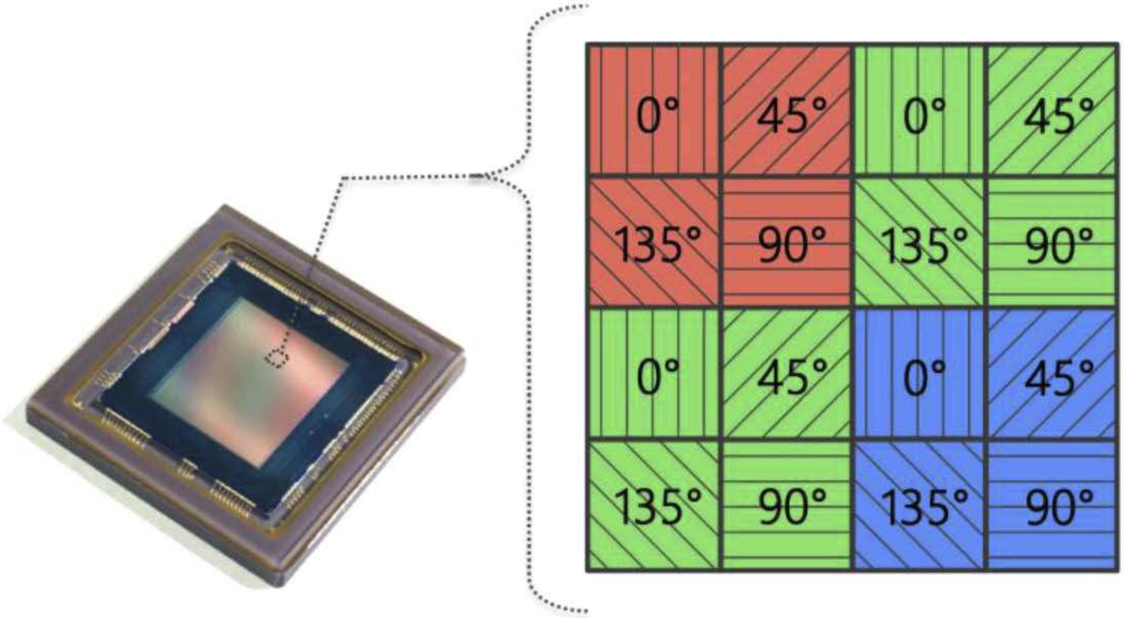

Figure 9.3. Sony IMX250MYR CMOS color polarization image sensor. (R: G1: G2: B)

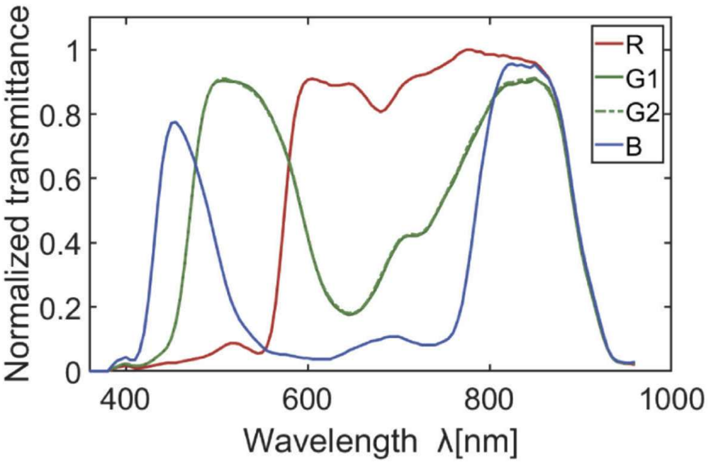

Figure 9.4. Normilized transmittance of the color filter of the color polarization image sensor.

The above graph shows a normalized transmittance for the Sony IMX250MYR CMOS color polarization image sensor for R,G,G2 and B color channels across a range of wavelengths 400nm - 1000nm.

The blue B channel has high transmittance in the visible blue light range (400nm-500nm),green at 500-600nm and R around 600-700nm,and extends into the near-infrared (NIR) spectrum.

(Ono, S. (2020). Snapshot multispectral imaging using a pixel-wise polarization color image sensor. *Optics Express*, *28*(23), 34536-34573.) https://doi.org/10.1364/OE.402947

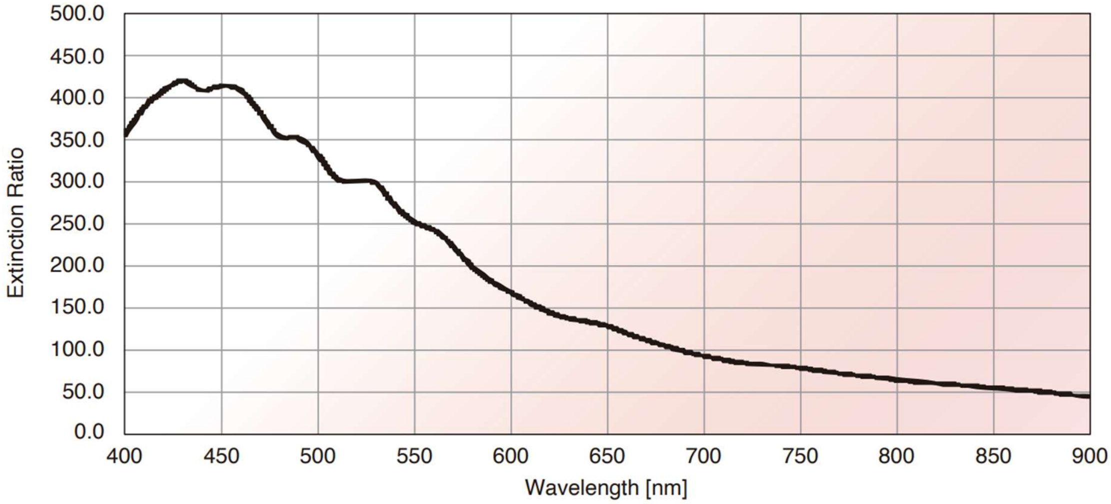

Figure 9.5. Omnidirectional Extinction Ratio (Minimum) is highest at around 420 when the wavelength is about 430nm. The ratio gradually decreases as the wavelength increases. The data may vary according to test environment. For IMX250MZR/IMX264MZR/IMX253MZR Omnidirectional Extinction Ratio (Min.)

Source:https://www.sony-semicon.com/files/62/flyer_industry/IMX250_264_253MZR_MYR_Flyer_en.pdf

Or https://www.sony-semicon.com/en/products/is/industry/polarization.html

(Sony Semiconductor Solutions Corporation, “Polarization image sensor with four-directional on-chip polarizer and global shutter function,” 2021, https://www.sony-semicon.co.jp/e/ products/IS/industry/product/polarization.html)

Both , Accessed on 21 Nov 2025 2: 10 am, 2:14 am ,

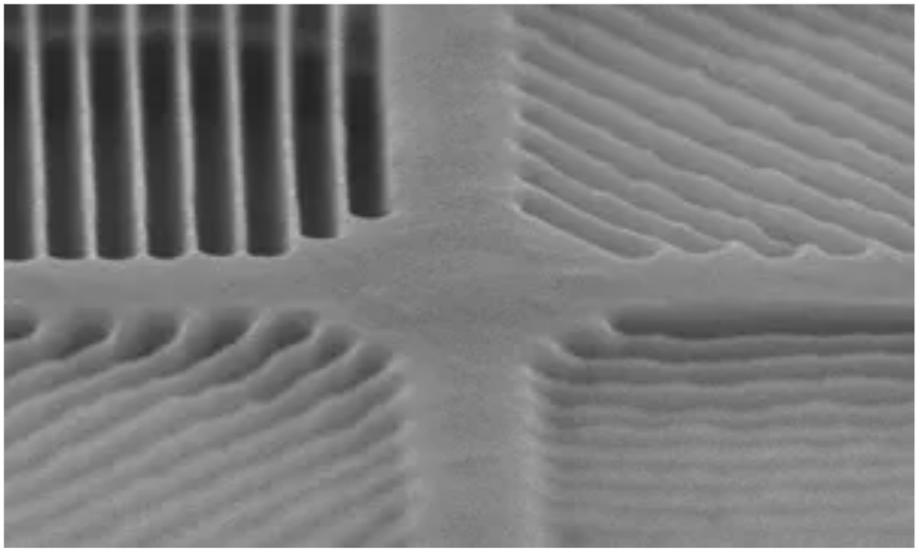

Figure 9.6. Polarizer image

Source: https://www.sony-semicon.com/en/technology/industry/polarsens.html

21 November 2025 2: 28 am

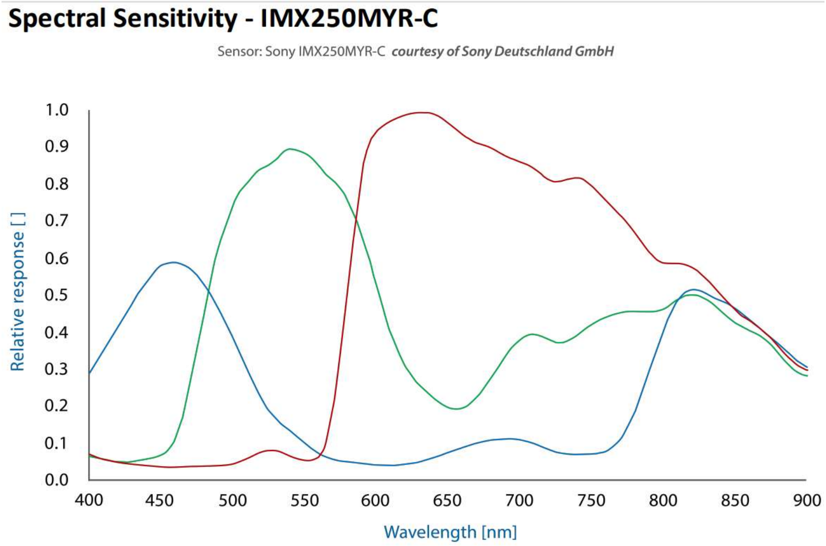

Figure 9.7. Spectral sensitivity of the Camera. Source: the brochure of the https://www.theimagingsource.com/products/industrial-cameras/usb-3.0-polarsens/

Acknowledgment

- Deepest gratitude to my supervisor, Prof. Miklos Fried, whose paramount support and guidance was crucial on this research work.
- Special thanks to Prof. Peter Patrik and all my colleagues who contributed on my research work……

- National Higher Education and Research Institute (NHERI), Asmara, Eritrea.

- Stipendium Hungaricum scholarship, Hungary
- Doctoral School on Materials Sciences and Technologies, Óbuda University , Budapest, Hungary.
- Institute of Technical Physics and Materials Science Centre for Energy Research, Budapest, Hungary.
- VOC-DETECT M-Era-Net project OTKA NNE 131269 project.

- NKFIH OTKA K 143216 and 146181 projects. Project TKP2021-EGA-04 has been implemented with the support provided by the Ministry of Innovation and Technology of Hungary from the National Research, Development, and Innovation Fund, financed under the TKP2021 funding scheme. Within the framework of the 20FUN02 “POLight” project, this work has received funding from the EMPIR program, co-financed by the Participating States, and from the European Union’s Horizon 2020 research and innovation program.